To everyone, everywhere,
who is breaking away from the role
into which society
has attempted to cast them.

ACCRETION FLOW AND RADIATION PRODUCTION IN A NEUTRON STAR'S MAGNETOSPHERE.

A Thesis submitted by

LINDA ANN CORNWALL

for the degree of

Doctor of Philosophy
in the
University of London

Researched and studied at
Imperial College of Science and Technology,
University of London.

December 1987.

Abstract

This thesis describes X-ray sources powered by the loss of gravitational potential energy of matter accreted by a compact object. It describes X-ray pulsars, where the compact object is a magnetised neutron star and the accretion flow is highly influenced by the magnetic field.

For the case when accretion takes place from a stellar wind and the flow towards the neutron star is spherically symmetric; the shape of the magnetosphere is calculated. Accretion flow in the outer regions of the magnetosphere is modelled, the plasma being heated by X-rays produced near the surface of the neutron star.

Limiting cases for radiation production and expected photon energies are described. A method for calculating a soft limit for the spectrum produced when radiation is emitted from the sides of an accretion funnel is presented.

Accretion flow near the bottom of an accretion funnel is modelled, where the flow is slowed down by a radiation pressure gradient. Self-consistency, in the sense that the energy available is equal to the radiative energy output is checked. The model is self-consistent over a wide range of luminosities, 0.06-20 times the Eddington luminosity. The radiation is found to be emitted from the sides of the accretion funnel over a height very much smaller than the radius of the neutron star.

For most of the length of the accretion funnel little radiation is produced. This region is not heated by radiation from the bottom of the funnel due to geometrical effects. The physics of this region and possible radiation output from this region is discussed. The possibility of improving the model by considering radiative transfer in the region of the funnel just above where slowing down takes place is also discussed.

Contents.

List of Figures.

List of tables.

CHAPTER 1.

Introduction.

§1.1 Introduction to X-ray Astronomy.

§1.1.1 Discovery of X-ray Astronomy.

As the earth's atmosphere is opaque to photons in the energy range $0.2 \rightarrow 20keV$, observational X-ray astronomy could not begin until it was possible to launch rockets or satellites. (In the hard X-ray range, $30 \rightarrow 150keV$, observations can be made from balloons above a height of 35km.) X-ray Astronomy began in 1962. The only observed extra-terrestrial X-ray source at that time was the sun, which gave an X-ray flux of $\approx 10^6 photons\, cm^{-2} sec^{-1}$. Since the nearest star is $\sim 10^5$ times further away than the sun, even if it emitted 100 times as much X-radiation as the sun if would have been undetectable with the available X-ray detector sensitivity. This indicates that as X-ray sources were detected at that time from outside the solar system they must come from objects somewhat unlike main sequence stars.

Cosmic ray astrophysics was a well developed subject before the beginning of X-ray astronomy; see for example *Wilson 1976.* Primary cosmic rays have energy up to $\approx 10GeV$. If a small fraction of this energy could be given up to photons by processes such as inverse Compton scattering of cosmic ray electrons by starlight; or synchrotron radiation by cosmic ray electrons in a magnetic field: then X-rays or photons of higher energy may easily be produced. Also, the existence of cosmic rays indicated that processes exist that accelerate particles to high energies, therefore it was not unreasonable to suppose that photons with energies corresponding to the X-ray part of the spectrum may occur in nature.

In 1962 the American Science and Engineering group launched a rocket to detect X-rays from the sun reflected by the moon. No signal from the moon was detected but X-rays were detected from the constellations Scorpio and Sagittarius; *Giacconi et al 1962.* Since then many more X-ray observations have been made, the earlier by rocket and later by satellite. The earlier observations detected a number of strong galactic X-ray sources, concentrated mainly along the galactic equator. Later, extra-galactic sources were added along with many

more galactic sources as the sensitivity of X-ray detectors improved and the duration of observations increased.

When X-ray astronomy got under way it was found that the most powerful of the X-ray sources were thermal X-ray sources. This could not have been predicted from the astrophysics known at that time. Sco X-1 as a thermal source is described by *Felten + Rees 1972.*

§1.1.2 Early identification of X-ray sources with optical sources.

Initially identification of X-ray sources with optical sources was a very slow process. This was because high luminosity X-ray sources are often associated with low luminosity optical sources. Also, the position of the X-ray sources was not known very accurately. Identification was often made as a result of phenomena such as simultaneous flaring of both an optical source and an X-ray source.

The size of the region of X-ray emission was also not known accurately. One of the first experiments to accurately find the size and position of an X-ray source was carried out in 1964, when the moon occulted the Crab nebula. A rocket was launched with an X-ray detector which observed the Crab nebula as the moon passed in front of it. The observed X-ray source diminished gradually, indicating that the source was diffuse.

Scorpio X-1 is a star-like X-ray source and is the brightest X-ray source in the sky. The spectrum of Scorpio X-1 is a good fit to a bremsstrahlung spectrum. Extrapolation of this bremsstrahlung spectrum gives a visual magnitude of ≈ 13. An ultra-violet excess compared to normal stars would also be expected. An appropriate optical object was found.

§1.1.3 Techniques for detecting X-rays.

The first X-ray detectors were proportional counter detectors, which are effective in an energy range of $0.2 \rightarrow 25keV$. A proportional counter detector consists of a sealed electrically conductiong box, one side being a window, filled with 90% inert gas, 10% polyatomic gas. Inside the box is an anode wire at a potential of $\approx 2000V$ insulated from the box. When an X-ray photon enters the box through the window it is photoelectrically absorbed by the inert gas. The photoelectron produced has energy similar to that of the X-ray photon. This electron ionises further atoms and the electrons produced are attracted towards the anode resulting in an electrical signal roughly proportional to the energy of the X-ray photon. Early X-ray detectors had a very low energy resolution $\frac{E}{\Delta E} \approx 1$. This compares to more recent X-ray detectors such as the Objective Grating Spectrometer on the Einstein satellite which has an energy resolution $\frac{E}{\Delta E}$ of up to 50 for soft X-rays. Also on the Einstein, the Focal Plane Crystal Spectrometer has a resolution $\frac{E}{\Delta E} \sim 60 \rightarrow 700$. The spectra of X-ray sources are usually expressed as counts $cm^{-2}sec^{-1}keV^{-1}$ plotted against energy in keV. For a more detailed description of the development of X-ray spectroscopy see *Holt + McCray 1982.*

Scintillation counters are often used for energies greater than $10keV$. These consist of a crystal optically coupled to a photomultiplier tube. An X-ray photon is photoelectrically absorbed by the crystal. The photoelectron produced ionises more atoms and some of the energy is converted into visible light which is detected by the photomultiplier.

In front of the detector is some sort of device which selects the direction from which the photons that enter the detector come. This may be a collimator or focussing optics.

The simplest type of collimator consists of 2 sets of interlocking parallel metal plates which only allow photons to enter the detector that are incident along the axis of the plates. The two sets of plates are usually at right angles to one another although the spacing between one set of plates may be different from the other. The earliest collimators were of this type.

Another common type of collimator is the modulation collimator. This consists of 2 sets of parallel wires, one above the other and parallel to each other. For a star like source the first casts a shadow on either the wires or the gaps between the wires according to the position of the source. The object being

studied is scanned in 2 directions in order to find its position.

X-rays with energies below $\approx 4keV$ can be focussed using grazing incidence optics. The Imaging Proportional Counter (IPC) on the Einstein observatory was an example of a device with grazing incidence optics. The field of view on the IPC was 1° with an angular resolution of $1'$.

§1.1.4 Categories of X-ray sources.

X-ray sources may be divided into three main classes. Those of galactic origin, those of extrgalactic origin, and the X-ray background. The majority of galactic X-ray sources lie in the galactic plane. Galactic sources may be star like: examples of star-like X-ray sources are neutron stars (such as Her X-1, Sco X-1), coronal emitters, and cataclysmic variables (such as AM Her). Galactic X-ray sources may also be diffuse (such as the crab nebula). The majority of galactic X-ray sources are star like. Extra-galactic X-ray sources include Seyfert galaxies and Quasars.

The following section (1.2) describes some of the general arguments used to understand the nature of cosmic X-ray sources. Section 1.3 introduces accreting binary systems. Sections 1.4, 1.5 and 1.6 introduce some of the commonly known X-ray sources. Section 1.7 considers the importance of the study of astrophysical objects containing neutron stars.

§1.2 Some general argumemts concerning X-ray sources.

§1.2.1 Luminosity and flux as a function of distance.

If a source has a luminosity L_x in the X-ray part of the spectrum and the distance to that source is D, the observed energy flux will be given by the well known relationship

$$F = \frac{L_x}{4\pi D^2}$$

Where F is the energy flux at the earth, i.e. the no. of counts per unit area per unit time multiplied by the mean photon energy. If we know the distance to an X-ray source we therefore know its luminosity.

§1.2.2 Maximum size of an X-ray source.

The luminosity of a source cannot vary substantially over a time less than the time taken for light to travel from one side of the source to another. A small variation in output in less time than this is possible as a change may take place over a small portion of the source. The maximum size of an object whose luminosity varies substantially over a time T is therefore cT, where c is the velocity of light.

§1.2.3 Location and luminosity of galactic X-ray sources.

The higher energy galactic X-ray sources, i.e. those emitting X-rays where the photon energies are of the order of a few keV, are dispersed across the plane of the galactic equator with a mean deviation of $\approx 3°$. If these sources are supposed to be dispersed at random about the central plane of the galaxy with a mean deviation of $\approx 300pc$ (the approximate thickness of the galactic plane), then the mean distance to these sources is $4000pc$. This means that the galaxy contains a few bright high energy X-ray sources at large distances rather than a large number of weaker sources.

As an estimate of the magnitude of the distances to the high energy X-ray sources can be made, an estimate of the magnitude of their luminosities can also be made. Typically, high energy galactic X-ray sources have a luminosity in the range $10^{35} \rightarrow 10^{37} erg\, sec^{-1}$. This is large compared to the solar luminosity which is a total of $3.9 \times 10^{33} erg\, sec^{-1}$ over all wavelengths.

As many sources have a high energy X-ray luminosity of $10^{37} erg\, sec^{-1}$ and there are approximately 200 such sources in the galaxy, this gives a rough estimate of the high energy X-ray luminosity of the galaxy of $2 \times 10^{39} ergs\, sec^{-1}$. This is small compared to the optical luminosity of the galaxy $\approx 10^{44} erg\, sec^{-1}$.

Lower energy X-rays come from main sequence stars dispersed throughout the galaxy. These main sequence stars have an X-ray luminosity of $\sim 10^{28} \rightarrow 10^{31} erg\, sec^{-1}$, and have been investigated by the Einstein observatory.

§1.2.4 Mass function.

A large number of galactic and many extragalactic X-ray sources are in binary systems. A useful quantity that allows an estimate of the mass of the X-ray emitting object to be made is the mass function. The mass function can be calculated from observable quantities, and is expressed as follows:-

$$\frac{M^3 \sin^3 i}{(M+m)^2} = \frac{(2\pi)^2 r^3 \sin^3 i}{GT^2}$$

where m is the mass of the X-ray source, M is the mass of the companion r is the radius of the orbit of the X-ray source around the centre of mass of the system, T is the period of the orbit, G the gravitational constant and i is the angle of inclination of the plane of the system.

The quantities $v \sin i$ and the period T can be measured from time delays in the arrival of the X-ray pulses in the case of pulsating sources, hence $r \sin i$ can be measured. The period T may also be measured from the doppler shift. An estimate of the mass of the companion star can often be made from its nature. This allows an estimate of the mass of the X-ray star to be made.

§1.2.5 X-ray production mechanisms and spectra.

The main properties of cosmic X-ray spectra are a low energy cutoff, and a fall off at higher energies either following an exponential or power law. Those spectra which fall off exponentially at higher energies are usually thermal X-ray sources; where the X-rays are produced in a plasma having a temperature of $\sim 10^7 \rightarrow 10^8\,^{\circ}K$. Compact galactic X-ray sources are thermal sources. There are 2 main thermal production mechanisms, Bremsstrahlung and Black body radiation.

Bremmstrahlung results from the acceleration of electrons by the postive ions in an ionised plasma. The electrons are assumed to have a boltzman energy distribution and the resulting emission is proportional to the number density of electrons squared (n_e^2). When expressed in counts per unit energy the shape of the spectrum is given by:–

$$N(E) = K_1 \frac{e^{E/T}}{E\sqrt{T}}$$

Where energy and temperature are expressed in keV.

Black body radiation results when the emitting region is optically thick. The radiation energy spectrum of temperature T when expressed in counts per unit energy is given by:–

$$N(E) = K_2 \frac{E^2}{\left(e^{E/T} - 1\right)}$$

The shapes of black body and Bremsstrahlung spectra are shown in fig 1.1 when the temperature is 10keV. Note that the spectra are plotted in counts per unit energy as a function of energy. It is also worth noting that if the Bremsstrahlung spectrum was plotted as energy recieved per unit energy then it would be flat at low energies.

Power law spectra usually result from inverse Compton or synchrotron emission. The resulting power law is due to the power law energy spectrum of the electrons. Inverse Compton scattering is caused by electrons scattering starlight or the microwave background photons, and processes occuring in accreting plasma near the stellar surface.

Synchrotron radiation results from relativistic electrons being accelerated by a magnetic field. A power law spectrum is of the form:–

$$N(E) = K_3 E^{-\alpha}$$

A power law spectrum is also shown in fig 1.1. The spectra in fig 1.1. are in arbitrary units; they are also not scaled to one another. Fig 1.1 shows the shape of the spectra only.

If a source contains regions at different temperatures then these cases may become confused; therefore interpretation of the nature of observed sources is not always simple. The low energy cut off is usually due to absorption by material in the line of sight between the source and the observer; although it may be caused by reabsorption by the emitting material.

§1.3 Basic description of the X-ray binary system.

§1.3.1 The basic principle of accretion.

For many star like high luminosity X-ray sources the energy is believed to be derived from the gravitational potential energy released as matter is accreted by a compact object. Therefore, it is worthwhile to describe the basic principle of accretion before describing the various types of X-ray source.

Many binary systems consist of a compact object, either a white dwarf, neutron star, or a black hole with a main sequence or giant companion. Under certain circumstances matter may flow from the companion onto the compact object. If matter flows onto a compact object mass M to a radius r the energy available is given by:-

$$E = \frac{GM\dot{m}}{r}$$

where G is the gravitational constant and $\dot{m}$ is the mass flow per unit time. r may be the radius of a neutron star or white dwarf, or the Schwarzschild radius of a black hole. The energy released is $\sim 10\%\dot{m}c^2$ for a neutron star and up to $\sim 30\%\dot{m}c^2$ for a black hole. As the innermost stable orbit of a black hole is at a radius greater than the Schwarzschild radius it is thought that the maximum energy released is $\sim 30\%\dot{m}c^2$; see for example *Eardley and Press 1975.*

There are thought to be three basic mechanisms for the transfer of matter from the companion to the collapsed star, and these are described below. Real cases may however be a combination of more than one of these mechanisms.

§1.3.2 Roche lobe overflow.

In a binary system with circular orbits the gravitational equipotential forms a figure of eight; see fig 1.2. This bounds the region around each star that is dominated by the gravitational field of that star. The figure of eight is is often called the Roche lobe. If the separation between the stars is small the non-compact star may expand to fill its Roche lobe; matter may then flow across the inner lagrangian point towards the compact star. This is known as Roche lobe overflow, and is a likely mechanism for high mass transfer rates onto a compact star. This process is described by *Davidson and Ostriker 1973* and *Willmore 1978.*

The matter accreted will have angular momentum with respect to the compact star. Therefore, the matter cannot fall directly towards the surface of the compact star and will form an accretion disc around it. The matter then slowly looses angular momentum through viscous dissipation processes and passes towards the neutron star. For a review of accretion discs see *Pringle 1981.*

§1.3.3 Accretion from a stellar wind.

The outflow from a hot corona, the stellar wind, is $\sim 10^{-6} M_{\odot}$ per year from O or B stars. This can produce an accretion rate onto the companion star of $\sim 10^{-9} M_{\odot}$ per year which is sufficient to produce a luminosity of $\sim 10^{37} erg\, sec^{-1}$ for a $1 M_{\odot}$ neutron star.

If a stream of matter velocity v_{rel} and density ρ is passing an object of mass M the object will accrete matter within a radius of:–

$$r_{accr} = \frac{2GM}{v_{rel}^2}$$

ignoring the effect of radiation on the infalling matter. Therefore, the accretion rate is given by

$$\dot{m} = \pi \xi r_{accr}^2 v_{rel} \rho$$

where ξ is less than one to account for phenomena such as radiation pressure on the matter. Stellar wind accretion is described in more detail by *Davidson and Ostriker 1973.* Fig 1.3 shows accretion from a stellar wind.

§1.3.4 X-ray induced stellar wind.

In a close binary system mass transfer may be induced by X-ray heating of the outer layers of the companion star. The X-ray luminosity must be quite large to sustain sufficient mass transfer. Such a self-sustaining feedback mechanism is thought to be present in Her X-1.

§1.4 Galactic X-ray sources.

§1.4.1 Cataclysmic variables.

Cataclysmic variables have been well known as optical sources for many years. They exhibit a wide variety of phenomena, including pulsations and optical polarisation. Many of them flare up at regular or irregular intervals. As X-ray sources they vary on a time scale of hours. They are binary systems containing a white dwarf and a low mass main sequence star; where matter is accreted onto the white dwarf from the companion as described in section 1.3.

Cataclysmic variables are often divided into three main categories, those where the white dwarf has a weak magnetic field, those containing a white dwarf that has a magnetic field of sufficient strength to sufficient to disrupt the accretion flow before it reaches the stellar surface, and those where the magnetic field is of sufficient strength to dominate the accretion flow.

In the case where the white dwarf contains a weak field, the matter accreted by Roche lobe overflow is likely to form an accretion disk that extends down to the surface of the white dwarf. In this case high energy X-rays do not dominate energy emission, but ultra-violet and soft X-rays are produced.

The second type of cataclysmic variables are often known as DQ-Her type, or Intermediate Polars. These are sources where the white dwarf has a magnetic field sufficient to channel the accreting plasma towards the magnetic pole. If the magnetic axis is not aligned with the rotation axis pulses may be emitted. These sources are strong emitters in the $2 \rightarrow 10keV$ energy range.

The third type of cataclysmic variables are often known as "phase-locked" stars. In these systems the rotation of the white dwarf is phase-locked to the binary period and material from the companion is directly funnelled onto the polar cap. They are also known as 'Polars' because their optical output is polarised. AM Her is an example of this type of star, and these high field stars are sometimes known as "AM Her" type. The discovery of a magnetic compact

star in AM Her was reported in *Tapia 1977*. The magnetic field of the white dwarf is $\sim 10^8 gauss$. AM Her is described by *Fabian et al 1977*, and cataclysmic variables are described by *Mason 1985*.

§1.4.2 Non-pulsating X-ray binaries and X-ray bursters.

These are variable, non-pulstating, non-eclipsing X-ray sources. They have luminosities greater than $10^{36} erg\, sec^{-1}$. The distribution of these sources is concentrated towards the galactic centre, and follows the distribution pattern of old, population II stars.

Some of these sources emit X-ray bursts, which have a rise time of $\sim 1s$ and decay over $3 \rightarrow 100 sec$. The peak luminosity during these bursts is $\sim 10^{38} erg\, sec^{-1}$, and the total output per burst is typically $\sim 10^{39} erg$. The existence of these X-ray burst sources helps in the understanding of this more general class of X-ray source.

The spectrum at the peak temperature of a typical X-ray burst is well fitted to a black body of temperature $3 \times 10^7\, ^\circ K$. As the burst decays it remains well fitted to a black body spectrum emitted from a body that corresponds to a sphere of radius $\sim 10 km$. The interval between bursts is typically $\sim 10^4 \rightarrow 10^5 sec$. The ratio of the average persistent luminosity to the average burst luminosity, $\alpha \sim 10^2$.

These non-pulstating sources, whether bursters or not, are thought to be powered by accretion onto a non-magnetic neutron star. The commonest theory for the nature of the burst is that there is a thermonuclear flash in the surface layers of the accreting neutron star. 10^2 is the ratio of the energy released by accretion onto a neutron star $\sim 10\% \dot{m}c^2$ to the energy liberated due to Helium burning $\sim 0.1\% \dot{m}c^2$. The thermonuclear flash model is thought to account for the majority of X-ray burst sources.

For one source, the rapid burster MXB 1730-355, the interval between bursts is $10 \rightarrow 100 sec$ and $\alpha \sim 2$. This type of source obviously cannot be explained by the thermonuclear flash model. These types of source have been classed 'type II' burst sources. Another possible cause for bursts is instabilities in the accretion onto the collapsed object.

The surface magnetic field of these neutron stars has probably decayed, which is probable for a neutron star whose age is $> 10^9 yr$. The accretion disk

may extend down to the surface of the neutron star, half the gravitational potential energy being lost as the matter spirals inwards, thus giving a large soft X-ray flux.

The optical counterparts of these sources, where identified, are faint. The companions to the neutron stars in these types of sources are of low mass, and much of the optical output is thought to come from reproccessing of X-rays by matter such as the accretion disk within the binary system. The companion is thought to be a low mass main sequence or dwarf star. Mass transfer will only be sufficient if the companion fills the Roche lobe. This requires an orbital separation of$< 10^{11} cm$ which gives an orbital period of $\sim 0.3 days$. Eclipses of the X-ray sources are not observed.

The reason why eclipses are not observed is likely to be geometrical. If the accretion disk lies within the line of sight between the neutron star and ourselves we would not observe the X-rays as the disk viewed edge on is optically very thick with respect to X-rays. If we are observing from above the plane of the disk, the companion would not pass between us and the neutron star, hence we would not expect to observe eclipses.

For a more detailed description of X-ray burst sources see the review articles by *Joss + Rappaport 1984* and *Borner 1980.*

§1.4.3 X-ray pulsars.

The first binary X-ray pulsars were discovered in 1971 with the Uhuru satellite, *Giacconi et al 1971.* X-ray pulsars consist of a neutron star and a main sequence or giant star in a binary system. As in the case of radio pulsars, the pulse period is the period of rotation of the neutron star. The energy source of X-ray pulsars is the loss of gravitational potential energy of matter accreting onto the polar cap of a rotating neutron star. This is unlike the case of the radio pulsar, which is powered from the rotational kinetic energy of the neutron star. It is also worth noting that many X-ray pulsars speed up rather than slow down, hence the energy source cannot be simple rotational kinetic energy. Also worth mentioning, is if the energy source was rotational, then the life of the X-ray pulsar would be extremely short.

X-ray pulsars have large duty cycles, $> 50\%$, compared to radio pulsars whose duty cycles are $\sim 3\%$. Modulation factors for X-ray pulsars are typically

in the range $20 \rightarrow 90\%$. The pulse periods of X-ray pulsars vary between $\sim 67ms$ and $1000sec$.

The pulse shapes of the X-ray pulses are very varied, some are symmetric while others are highly asymmetric. There is no obvious correspondence between pulse morphology and either pulse period or luminosity.

Most of the X-ray energy is emitted in the range $2 \rightarrow 20keV$, with a rapid fall off in energy flux above 20keV. The spectra of the X-ray pulsars cannot be described simply in terms of a blackbody, thermal bremsstrahlung or power law. Also, many X-ray pulsars have an iron K shell emission feature at 7keV.

It is thought that many of the X-ray pulsars have a strong magnetic field, and there is observational evidence to support this. In the case of two X-ray pulsars, Her X-1 and 4U0115+63, X-ray features have been detected that can be explained in terms of cyclotron emission in a magnetic field. The first to be detected was Her X-1, *Trumper 1978*. In the case of Her X-1 the cyclotron feature corresponds to a magnetic field of 3.8×10^{12} *or* $5.3 \times 10^{12} gauss$ depending whether the spectral feature arises from absorption or emission.

The complex pulse shapes and their dependence on energy are not fully understood. The pulsations arise from non-spherically symmetric X-ray production from a rotating magnetic neutron star where the magnetic axis is misaligned with the rotation axis. The magnetic field channels the accretion flow and the X-ray pattern produced is viewed from different directions as the star rotates, thus producing pulsations. The light curves are different for different energy ranges, in some cases the peak of the light curve in one energy range coincides with a low for another energy range; see figs 1.4 and 1.5.

For a large number of X-ray pulsars, the companion to the neutron star is a giant star. The sizes of some of the companions to the X-ray pulsars are given in *Joss + Rappaport 1984*. This indicates that the dominant mass transfer mechanism is likely to be wind fed accretion. Many X-ray pulsars show eclipses, the fraction of the orbital period where eclipses are displayed gives further information on the nature of the companion and the orbital characterisics.

One of the best known X-ray pulsars, Her X-1, displays a 35 day cycle. This is in addition to the pulse period and orbital period. The emission from the source is low for most of this 35 day period but strong for part of it. Many explanations have been put forward for this 35 day cycle, including precession of

an accretion disk surrounding the neutron star and a possible third star in the system. Recent evidence described by *Trumper et al 1986* suggests that the 35 day cycle is caused by precession of the neutron star. This does not contradict the theory that mass transfer occurs due to an X-ray induced stellar wind.

Be binaries are sometimes described in a class of their own. They are X-ray binary systems containing a Be star in an eccentric orbit around a neutron star. *Apparao 1985.*

For a general review of X-ray binaries see *Borner 1980.* Most of the rest of this thesis is concerned with X-ray pulsars.

§1.4.4 Accreting Black Holes.

The best evidence for the existence of black holes is probably still the X-ray binary Cyg X-1. Cyg X-1 is identified with the supergiant star HDE 226868. Observations of the orbital characteristics and application of the mass function give a mass for the collapsed star much greater than the maximum mass of a neutron star.

Cyg X-1 goes through metastable states of 'high' and 'low' luminosity, the X-ray luminosity varying between 4×10^{37} and $6\times10^{37} erg\, sec^{-1}$; having irregular durations of weeks to years. Cyg X-1 also exhibits chaotic fluctuations on a time scale down to at least $10ms$.

There is no surface of a black hole in the way there is in the case of a neutron star or white dwarf. For this reason it is commonly thought that the X-ray output must come entirely from the accretion disk.

For a detailed description of Cyg X-1 see *Liang + Nolan 1984.*

§1.4.5 Supernova Remnants.

Supernova remnants are diffuse X-ray sources, a description of how they are formed can be found in most astronomy texts. Here a few examples of them as X-ray sources are described.

Cassiopeia A was formed from a supernova explosion in 1670. It has a large radio flux which decreases by 1.1% per year, indicating that it is a young supernova remnant. It is also an X-ray source where the X-rays come from the same region as the radio emission. The best spectral fit is a 2 component bremsstrahlung fit involving regions at $12 \times 10^6\,^\circ K$ and $60 \times 10^6\,^\circ K$. Tycho's supernova remnant is of similar nature.

Puppis A, Vela X, and the Cygnus loop are older SN remnants. The spectrum of Puppis A, when observed in the $0.2 \rightarrow 18keV$ range is best fitted to the spectrum produced by a thermal plasma at a temperature $3.6 \times 10^6\,^\circ K$.

The Crab nebula is a remnant of a supernova that exploded in 1054. The X-ray spectrum resembles a power law. The X-ray luminosity $L_x \sim 10^{37} erg\, sec^{-1}$, and the total luminosity over all wavelengths is $\sim 5 \times 10^{37} erg\, sec^{-1}$. The crab nebula contains a pulsar, NP05322, with a period of 0.331 sec. This pulsar is slowing down and the rotational kinetic energy lost is $\sim 8 \times 10^{38} erg\, sec^{-1}$. It is thought that this pulsar injects energy into the crab nebula which powers the entire source. The pulsar itself is also observed in the X-ray part of the spectrum.

§1.4.6 Some other types of galactic X-ray sources.

X-ray transients are X-ray sources whose luminosity builds up very suddenly and decays on a time scale of several tens or hundereds of days. They are widely thought to consist of binary systems containing a compact object accreting matter from a normal companion. The sudden large luminosity is caused by a large surge in the mass accretion rate onto the compact object. The luminosity typically increases by as much as 1000. One example of an X-ray transient is the reccurrent transient X-ray source 4U 1630-47. In an outburst in 1984 this source decayed from a maximum luminosity of $2 \times 10^{38} erg\, sec^{-1}$ to $4 \times 10^{36} erg\, sec^{-1}$ over a period of 100 days; *Parmar et al 1986.* Intensity variations were also observed over $\sim 20s$.

SS433 is a galactic jet source which emits radiation across the spectrum from radio to γ-ray wavelengths. It is a strong optical emitter, with an output at optical wavelengths of $\sim 2.5 \times 10^{39} erg\, sec^{-1}$, and an X-ray output $L_x \sim 5 \times 10^{35} erg\, sec^{-1}$. In the optical range, doppler shifted emission lines are observed, one set with a large red shift and another set with a large blue shift. The doppler features change in wavelength and drift through the spectrum time scale of days. The maximum redshift corresponds to a velocity of $50\,000 km\, sec^{-1}$. The simultaneous red and blue shifts are widely believed to be due to collimated, oppositely ejected jets. They are similar in nature to extragalactic jet sources, hence an understanding of SS433 may lead to an understanding of a wider class of jet sources.

The energy output of SS433 at X-ray wavelengths is small compared to both the optical output and the kinetic energy deposited in the material in the jets. The X-ray output varies on many time scales, but no variations are detected on a time scale $< 300s$ see, for example, *Grindlay et al 1984.* Imaging observations on the Einstein observatory show that 90% of the soft X-ray flux is coincident with the optical object. The remaining 10% is closely aligned with the major axis of W50, a diffuse nebula with which SS433 is closely linked. SS433 is likely to have an infuence on this nebula due to the large amount of energy contained in the jets. For a detailed description of SS433 see the review article by *Margon 1984* and references therein.

X-rays from non-compact stellar objects began to be detected during the late 1970's. Typically, stellar sources have an X-ray luminosity of $10^{26} \rightarrow$

$10^{28} erg\, sec^{-1}$. Much of the X-ray output from stellar sources is at an energy $E \leq 1keV$; and is thought likely to come from a hot stellar wind *Schreier 1982.* For a review of X-rays from stellar sources see *Rosner et al 1985.*

§1.5 Extragalactic X-ray sources.

Other normal galaxies probably contain X-ray sources similar to those in our galaxy. Individual X-ray sources are easily observable in the nearby Magellanic clouds. The nearby galaxy, M31, has an X-ray luminosity of $2 \times 10^{39} erg\, sec^{-1}$, which indicates that it is populated by X-ray sources similar to the X-ray sources in our own galaxy.

Radio galaxies such as Centaurus A are often detected as X-ray sources. The X-ray output is associated with the region observed at optical wavelengths rather than the radio lobes. X-rays are also detected from Seyfert galaxies. These are spiral galaxies with bright nuclei. Quasars are objects with very large red shifts. Their X-ray output is typically power law. The luminosity is very large, for example 3C 273 has an X-ray luminosity $L_x \sim 7 \times 10^{45} erg\, sec^{-1}$.

The commonest theory for the power source of active galactic nuclei is accretion onto a massive black hole at the centre of the galaxy. Some other theories exist, such as accretion onto a cluster of black holes, *Pacholczyk + Stoeger 1986.* It is likely that the power source is accretion onto a collapsed object of some sort due to the huge luminosities observed.

§1.6 The X-ray background.

There is an X-ray background radiation of $\sim 10^{-2} counts\, cm^{-2}\, sec^{-1}$.

At energies above $\sim 2keV$ the background is isotropic, suggesting that the background is extragalactic in origin. It is not known whether it is due to a diffuse source or a large number of distant sources.

At energies $< 2keV$ the flux is stronger at the galactic poles than in the plane of the milky way. One early possible explanation for the annisotropy was shadowing of an extragalactic background by the plane of the galaxy. No such shadowing occurs from the Large Magellanic clouds, so the soft X-ray background is believed to be of galactic origin.

§1.7 Importance of the study of systems containing neutron stars.

Observations of systems containing neutron stars can lead to a greater understanding of neutron stars themselves. *Wasserman + Shapiro 1983* consider binary systems containing an accreting neutron star. They derive a mass-radius relationship for an neutron star from observed physical processes ocurring exterior to the neutron star. Such calculations may constrain the equation of state of the neutron star. Possible equations of state of a neutron star are also constrained by the exsistence of millisecond pulsars, *Lindblom 1986.*

Sufficient data is available such that the orbital characteristics and masses of the components of the binary radio pulsar 1913+16 are known. This data can be used to calculate the period decay due to gravitational radiation of this system. This forms a test of general relativity, as described by *Taylor + Weisberg 1982.*

Accreting neutron stars are also relatively small scale objects where gravitational potential energy is converted into radiation. A large proportion of the rest mass of accreted material can be converted into radiation due to loss of gravitational potential energy. It is therefore likely that loss of gravitational potential energy is a very important radiation energy source in the universe. The study of small scale objects provides much insight into the conversion of gravitational potential energy into radiation, thus leading to a greater understanding of larger objects such as active galactic nuclei that are also gravitationally powered. One particular class of objects that are likely to be gravitationally powered are astrophysical jets. The galactic X-ray source SS433 being a smaller scale jet source has some properties similar to those of astrophysical jets, as described by *Davidson + McCray 1980.* An understanding of SS433, thought by many to be an accreting neutron star, may lead to an understanding of the large scale astrophysical jets.

Fig 1.1. X-ray emission spectra.

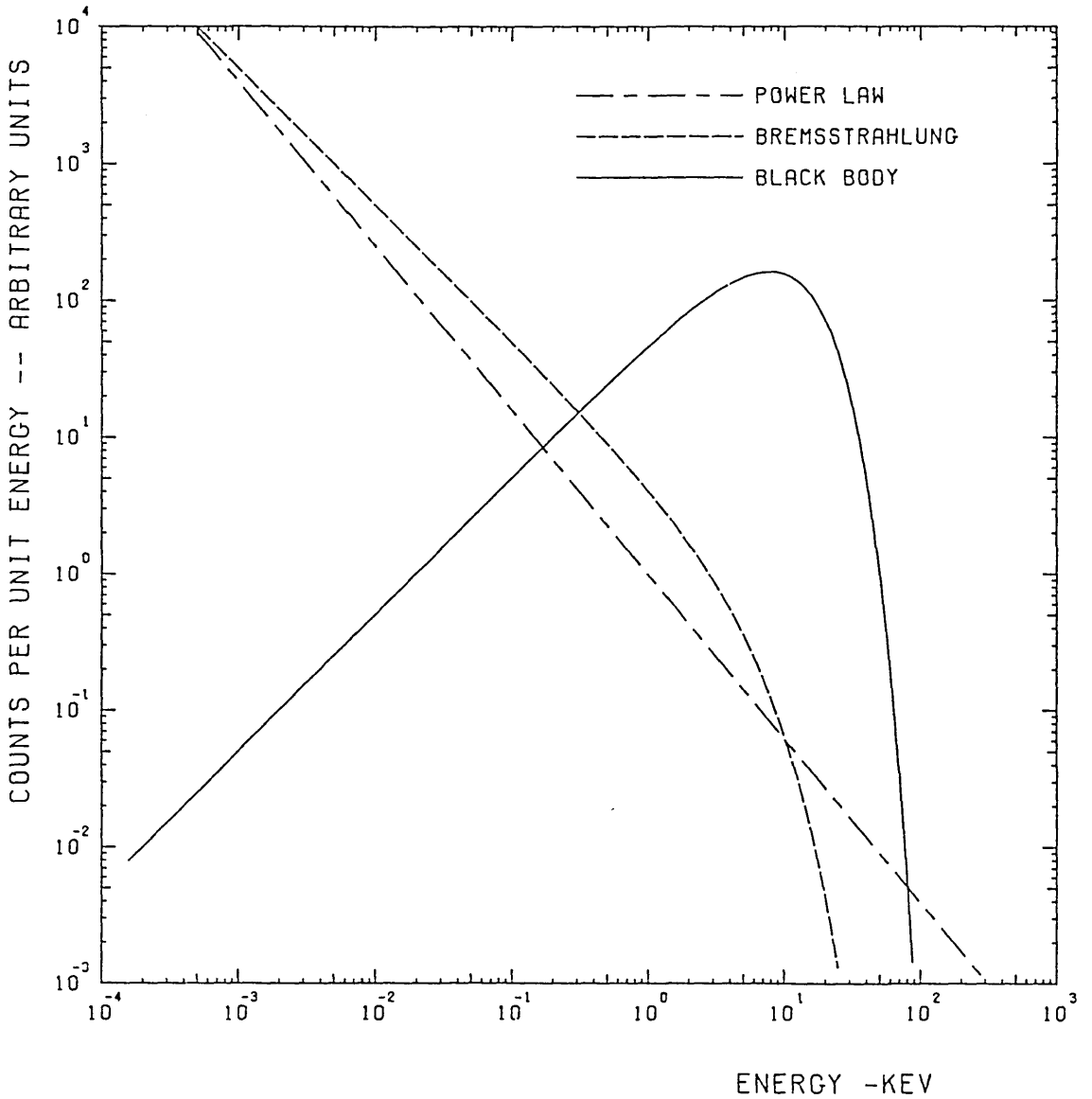

Figure 1.2. Roche lobe overflow.

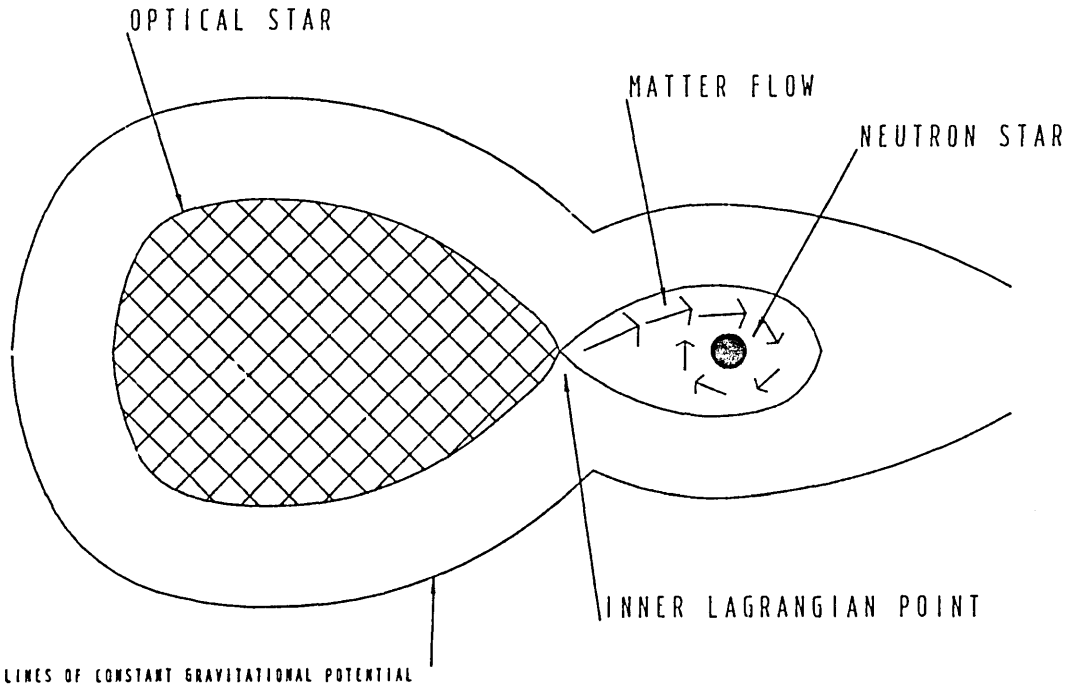

Figure 1.3. Accretion from a stellar wind.

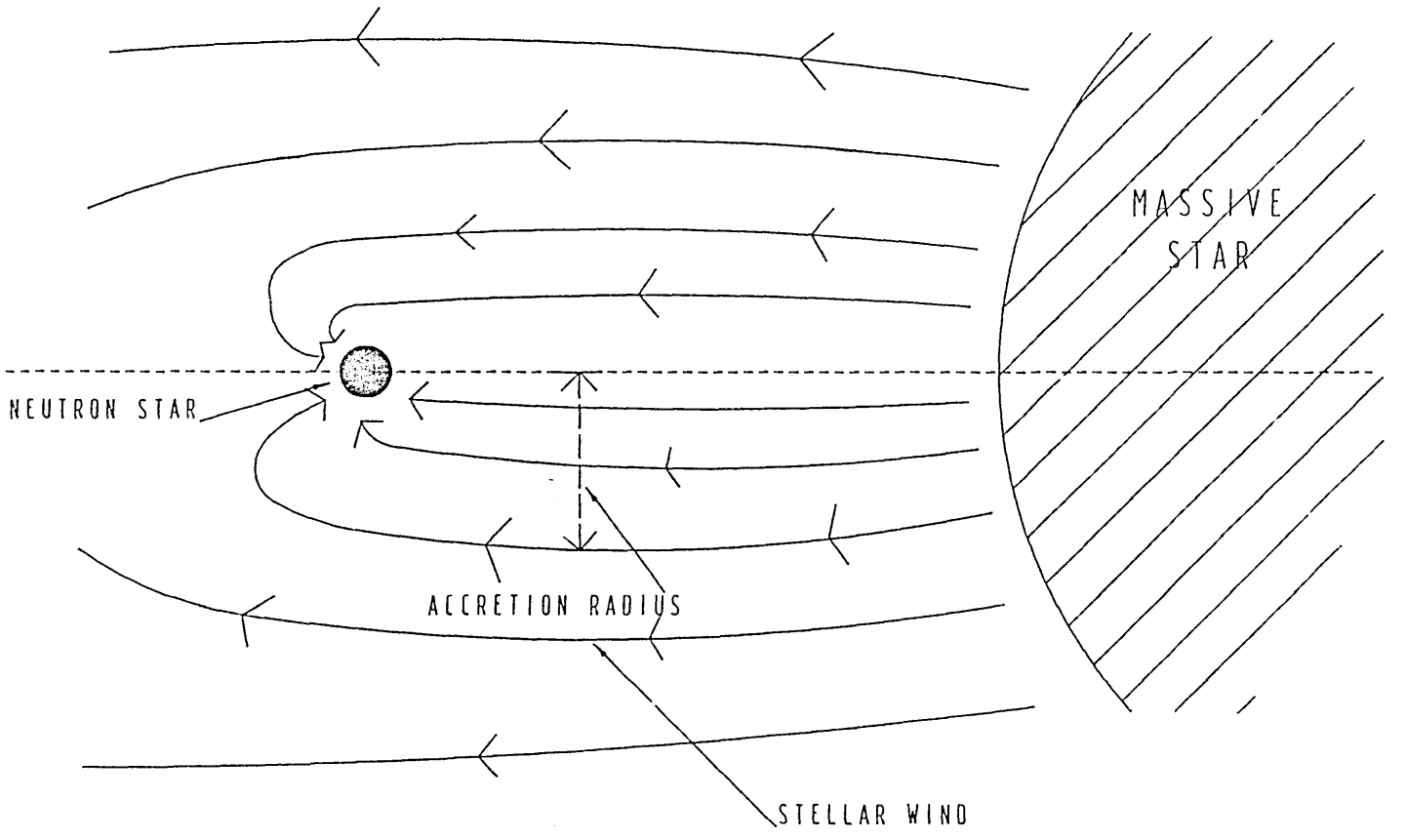

Figure 1.4. Light curves of the X-ray pulsar 4U 1626-6 for three X-ray energy ranges. Obtained from HEAO A2 observations, *Pravdo et al 1979.*

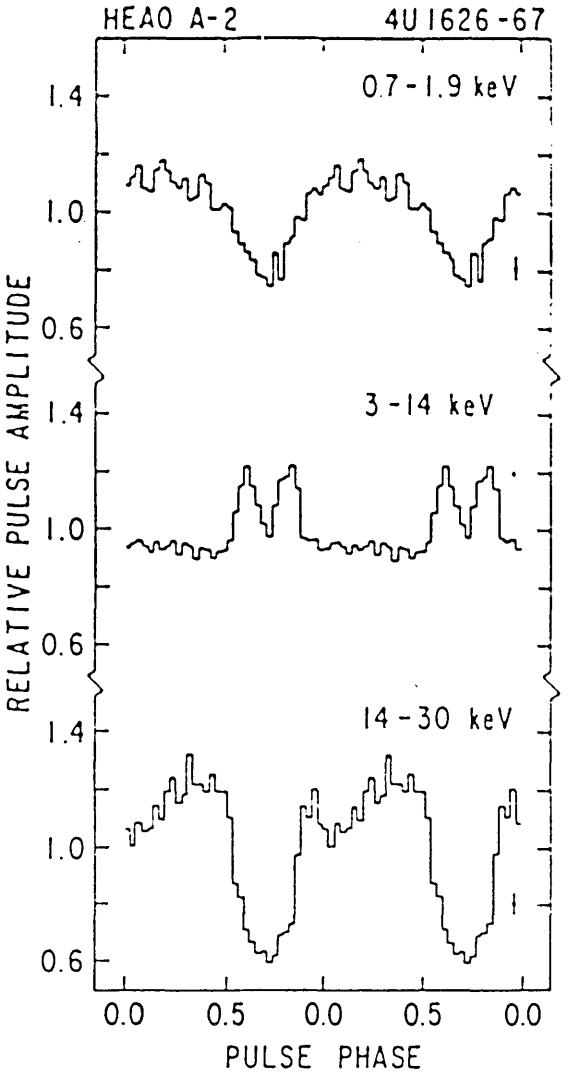

Figure 1.5. Light curves of the X-ray puslar Her X-1 for two energy ranges at different points in the 35 day period. Obtained from EXOSAT observations, *Trumper et al 1986.*

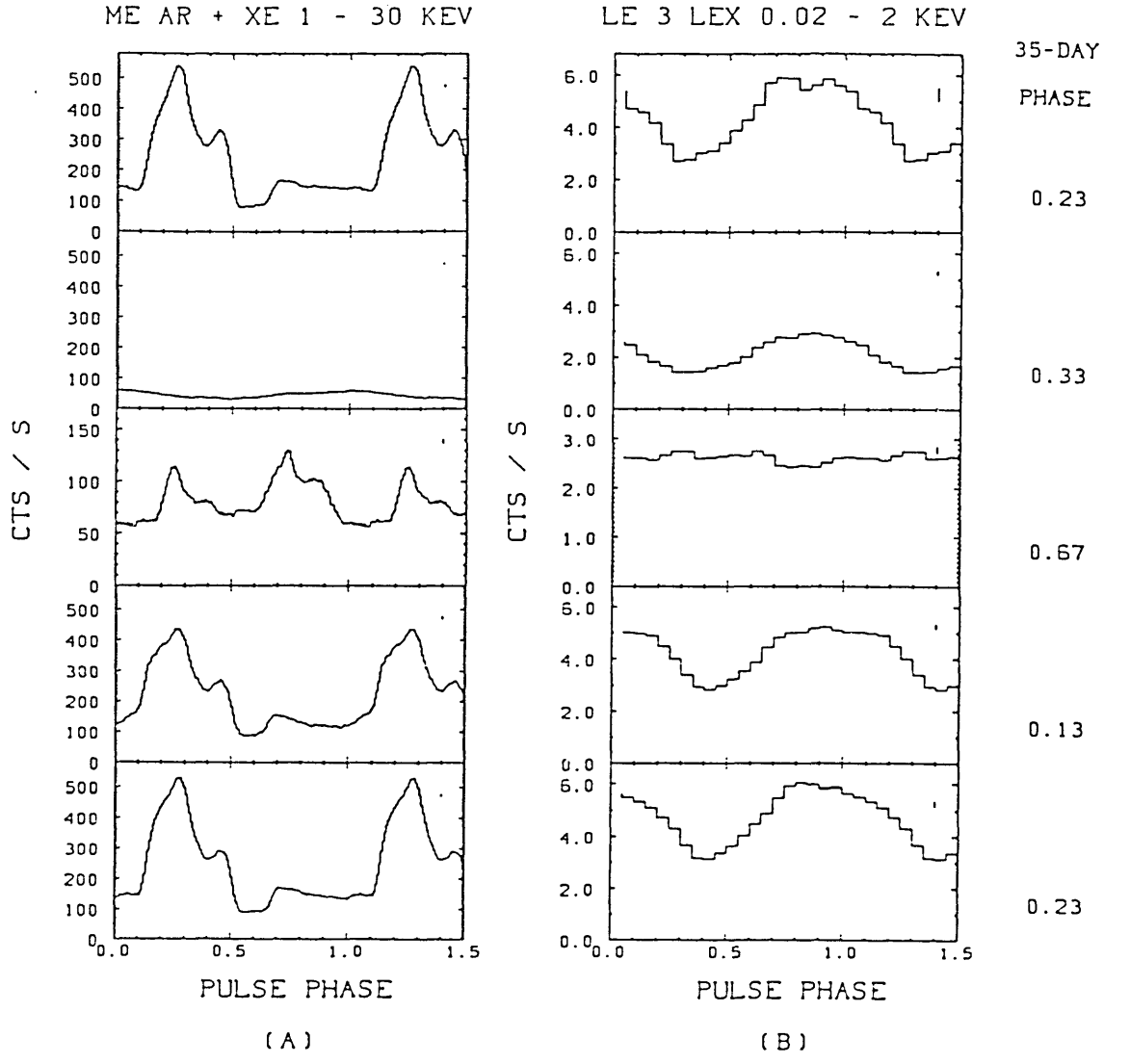

CHAPTER 2

The magnetosphere and plasma entry into the magnetosphere of an accreting neutron star.

§2.1 General properties and the importance of the magnetosphere

The magnetosphere is commonly defined as the region around a celestial object in which the magnetic field has dominant control over the motions of gas and charged particles. The magnetosphere of a planet or star results from the interaction between the magnetic field of the celestial object and any matter that may be present. The magnetopause is the boundary between where the flow is dominated by the magnetic field and where it is not. The most well studied magnetosphere is that of the earth, as for many years it has been observed directly by numerous space crafts. For a review of the properties of the earth's magnetosphere see *Akasofu 1978.*

As described in chapter 1, we are able to observe the magnetic field at the surface of 2 accreting neutron stars due to cylotron line emission. The large magnetic field present in sources such as Her X-1, which has a magnetic field of $\approx 5 \times 10^{12}$ gauss, will have a dominant effect on the channeling of accreted matter towards the surface of the neutron star. As the magnetosphere is defined as the region in which the magnetic field has dominant control over motion of gas and charged particles, it is obviously necessary to consider the shape and nature of the magnetosphere in order to understand accretion flow around a neutron star.

It is not known for certain whether the magnetosphere of an accreting neutron star is open or closed. The magnetosphere of the earth is known to be open. In the case of the earth, the magnetic field lines do not all close within the magnetosphere, but the magnetic field lines that originate from the polar cap of the are linked with the magnetic field lines of the solar wind. Again see *Akasofu 1978.* A schematic diagram of a neutron star with an open magnetosphere is given in Fig 2.1.

The shape of the magnetosphere will be different depending whether accretion takes place from a wind or an accretion disk. In the case of an accretion disk

the disk will interact with the magnetic field, and at a certain point the magnetic pressure will be greater than the pressure of the accretion disk and disrupt the shape of the magnetic field. The accreting matter will become linked to the magnetic field and channeled along it towards the surface of the neutron star. This scenario is described in *Basko + Sunyaev 1976* and a schematic diagram is given in Fig 2.2.

As noted in chapter 1, many of the neutron stars are known to have a giant star as a companion; therefore accretion from a stellar wind is the likely mass transfer mechanism for many of the X-ray pulsars. In the next section the shape of a magnetosphere resulting from the interaction of the magnetic field with a spherically symmetric inflow of matter is considered.

§2.2. Calculation of the shape of a closed magnetosphere.

As some authors consider it likely that the magnetosphere of an accreting neutron star is closed, a calculation of a possible shape of a closed magnetosphere is presented here. Here it is assumed that the captured matter free falls towards the neutron star, and where it interacts with the star's magnetic field it is falling in a spherically symmetric pattern. For a closed magnetosphere to occur the magnetic field outside the magnetosphere must be cancelled by currents set up in the ionised plasma at the magnetopause. It is assumed that as these currents cause the magnetic field to be cancelled outside the magnetophere they must locally double the magnetic field just inside the magnetosphere. The principle of this calculation is similar to that carried out by *Evans 1981*, using principles first used by *Beard 1960* for the calculation of the shape of the earth's magnetosphere.

For simplicity, it is assumed that the shape is defined by the ram pressure of the infalling matter equaling the magnetic pressure of the magnetic field of the neutron star. The geometry is that shown in Fig 2.3. $\hat{\mathbf{s}}$ is the unit vector along the magnetopause and $\hat{\mathbf{n}}$ is the unit vector perpendicular to the magnetopause, and $\hat{\mathbf{r}}$ is the unit vector in the radial direction.

First define $g_\theta = dr/d\theta$ along the magnetic boundary in the direction of $\hat{\mathbf{s}}$. Then, from looking at Fig 2.3.

$$\tan\chi = r\frac{d\theta}{dr} = \frac{r}{g_\theta}$$

Again, from looking at Fig 2.3. it is clear that:–

$$\hat{\mathbf{s}} = -\left(\cos\chi\hat{\mathbf{r}} + \sin\chi\hat{\theta}\right)$$

and the normal to the surface

$$\hat{\mathbf{n}} = \left(\sin\chi\hat{\mathbf{r}} - \cos\chi\hat{\theta}\right)$$

The magnetic field is assumed to be a dipole field, therefore:–

$$\mathbf{B} = \frac{\mu}{r^3}\left(2\cos\theta\hat{\mathbf{r}} + \sin\theta\hat{\theta}\right)$$

The component of the magnetic field along the magnetopause is:–

$$B_T = \mathbf{B}.\hat{\mathbf{s}} = -\frac{\mu}{r^3}\left(2\cos\theta\cos\chi + \sin\theta\sin\chi\right)$$

or

$$B_T = -\frac{\mu}{r^3}\sin\chi\left(2\cos\theta\frac{g_\theta}{r} + \sin\theta\right)$$

The next step is to equate the ram pressure $(\hat{\mathbf{r}}.\hat{\mathbf{n}})^2\, 2nmv^2$ to the magnetic pressure due to the component of the magnetic field parallel to the boundary B_T, i.e.

$$\frac{(2B_T)^2}{8\pi} = (-\hat{\mathbf{r}}.\hat{\mathbf{n}})^2\, 2nmv^2$$

This gives:–

$$\left(2\cos\theta\frac{g_\theta}{r} + \sin\theta\right)^2 = \frac{4\pi nmv^2r^6}{\mu^2}$$

Then from conservation of mass

$$4\pi r^2 nmv = \dot{m}$$

This gives:–

$$\left(2\cos\theta\frac{g_\theta}{r} + \sin\theta\right)^2 = \frac{\dot{m}}{\mu^2}\sqrt{\frac{2GM}{r}}r^4$$

From this we can find the radius of the magnetosphere at the magnetic equator, r_m. At the magnetic equator $\theta = 90°$ therefore:-

$$\frac{\dot{m}}{\mu^2}\sqrt{\frac{2GM}{r_m}}r_m^4 = 1$$

The observed magnetic field is assumed to be at the magnetic pole of the neutron star near the stellar surface, therefore from the equation for the dipole field

$$B_\star = 2\frac{\mu}{r_\star^3}$$

substituting this into the equation for r_m gives:-

$$\frac{r_m}{r_\star} = \frac{B_\star^{4/7} r_\star^{3/7} (GM)^{1/7}}{2^{5/7} L_x^{2/7}}$$

The radius of the magnetosphere at the magnetic equator is:-

$$r_m = 7.73 \times 10^8 \left(\frac{B_\star}{5 \times 10^{12} gauss}\right)^{4/7} \left(\frac{r_\star}{1.5 \times 10^6 cm}\right)^{10/7} \times \left(\frac{M_\star}{M_\odot}\right)^{1/7} \left(\frac{3 \times 10^{37}}{L_x}\right)^{2/7} cm$$

By substituting the expression for r_m into the expression for the shape of the boundary an expression for g_θ can be derived.

$$g_\theta \ (= \frac{dr}{d\theta}) = \frac{r}{2\cos\theta}\left(\left(\frac{r}{r_m}\right)^{7/4} - \sin\theta\right)$$

This gives an expression for r as a function of θ in the form of a first order ordinary differential equation. By starting at the magnetic equator, where $r = r_m$, the value of r for various values of theta can be found by integrating numerically. The shape of the magnetosphere calculated by the above method is shown in Fig 2.4.

This calulation is a very simple approximation to the real case. It ignores the effect of gravity on any matter accumulated at the magnetopause that has not yet entered the magnetosphere. It also ignores the effect of radiation on the infalling matter, as this may slow down the flow such that the infall velocity is much less than the free fall velocity. It does not consider what happens at the polar cusps, as the approximation for the geometry at this point by the

pressure balance may not be a good approximation to the real case. See for example *Arons + Lea 1976.* The calculation above does give a reasonable shape for the neutron star magnetosphere for this first order approximation. Much of what follows, including the model for accretion flow in the outer regions of the magnetosphere given in chapter 3, is not especially dependent on the exact geometry; therefore the shape and size of the magnetosphere calculated above is a reasonable one to work with.

§2.3 Plasma entry into the magnetosphere.

The accreted plasma is most commonly thought to enter the magnetosphere via the Rayleigh-Taylor (or Kruskal-Schwartzchild) instability. At a basic level, this can be considered as a dense layer of plasma outside the magnetosphere and a less dense one inside. Any small disruption is likely to result in the more dense plasma entering the magnetic field. A basic description of this instability is given in most plasma physics texts such as *Boyd + Sanderson 1969.* This is discussed in detail in *Arons + Lea 1976*, who suggest that as the plasma enters the magnetosphere the plasma is in the form of large 'bubbles', which need to be broken down and the plasma 'threaded' onto the magnetic field lines. They suggest that there are other intabilities that will break these 'blobs' down. They also calculate the size of the 'bubbles' to be $\sim 410km$ in their case when the radius of the magnetosphere is $\sim 2400km$. Thus in their case the plasma penetrates the magnetosphere down to $\sim 20\%$ of the radius of the magnetosphere. They also suggest that the cusps are unstable to the Rayleigh-Taylor instability, thus if plasma is to enter here another mechanism is required. A schematic diagram of the Rayleigh-Taylor instability is given in Fig 2.5.

A mechanism for plasma entry near the cusps was considered by *Michel 1977.* If plasma accumulates at the polar cusp, it will inevitably cool as it is out of view of the radiation coming from the bottom of the funnel. The density of this accumulated matter may become large enough such that it is able to push its way down through the magnetosphere towards the polar cap thus forming an accretion funnel. A schematic diagram of plasma entry through the cusp is given in Fig 2.6.

As spherically symmetric accretion is assumed, matter must accumulate at all points along the magnetosphere if it does not immediately enter the mag-

netosphere. This accreted matter must go somewhere, therefore there must be plasma entry at the cusps as well as at the equator where the Rayleigh-Taylor instability is most effective. In the case of non-spherically symmetric accretion all the plasma may enter at the magnetic equator and only penetrate the magnetic field to a depth of a small fraction of the radius of the magnetosphere, as the matter followed the field lines it would form an annulus at the polar cap. This is unlikely to occur for spherically symmetric accretion for the reasons given above, whether the magnotosphere is open or closed.

Some plasma must enter at the equator, whether accretion takes place from a disk or a wind. This plasma will follow the magnetic field lines towards the magnetic equator. In doing so it will be in sight of and therefore heated by the radiation coming from the bottom of the accretion funnel. This radiation will also effect a radiative pressure on the accreted matter. In chapter 3 the flow of the matter around the magnetic boundary within the magnetosphere is followed by a hydrodynamic approach.

§2.4 Mass transfer rates onto neutron stars.

As previously mentioned, in the case of X-ray pulsars, the most common mechanism for mass transfer is accretion from a wind. Mass transfer from a wind is substantially impaired by the pressure exerted on it by radiation. *Arons + Lea 1976* calculate a typical rate of mass transfer from a wind to be that which corresponds to a luminosity of $3 \times 10^{36} erg\, sec^{-1}$. Their calculations suggest that highly super-Eddington accretion is unlikely to occur when accretion takes place from a stellar wind. It is by definition of the Eddington limit in §4.3.1 that super-Eddington accretion cannot occur in straightforward spherically symmetric accretion.

Davidson + Ostriker 1973 consider the case of Cen X-3. They calculate the accretion rate from the stellar wind in this system, when it is modified by the outward radiation pressure. They conclude that the mass transfer rate will be large enough to power this X-ray source. *Willmore 1978* also considers this source, and calculates a mass transfer rate of at least $10^{17} g\, sec^{-1}$; clearly sufficient to power the observed luminosity.

In the case of Her X-1, it is thought by some authors that accretion takes place from a stellar wind induced by X-rays. This is not contradicted by the

recent observations by *Trumper 1986* that indicate that the 35 day period of Her X-1 is due to precession of the neutron star and not precession of an accretion disk. If an X-ray induced wind can provide a mass transfer rate onto the neutron star sufficient to power this X-ray source of luminosity $3 \times 10^{37} erg\, sec^{-1}$ then it is clearly possible that higher rates of accretion may be induced in systems containing a more massive companion. Again, this accretion is likely to be impaired by the force exerted on it by the outfow of radiation from the compact star.

If a system could be set up where the wind does not 'see' the radiation coming from the compact star then higher rates of accretion may be possible. If the X-rays come from the bottom of the sides of the funnel, as in the case of the fan beam model described in §4.4, then accretion may occur at higher latitudes and matter may fall towards the polar cusps of the neutron star. This case is shown schematically in Fig 2.7.

In the case of the other important mechanism for mass transfer, Roche lobe overflow, high accretion rates are considered possible. Many authors, for example *Basko + Sunyaev 1976* consider this the more likely mechanism for super-Eddington accretion.

Figure 2.1. Open magnetosphere with accretion from a stellar wind.

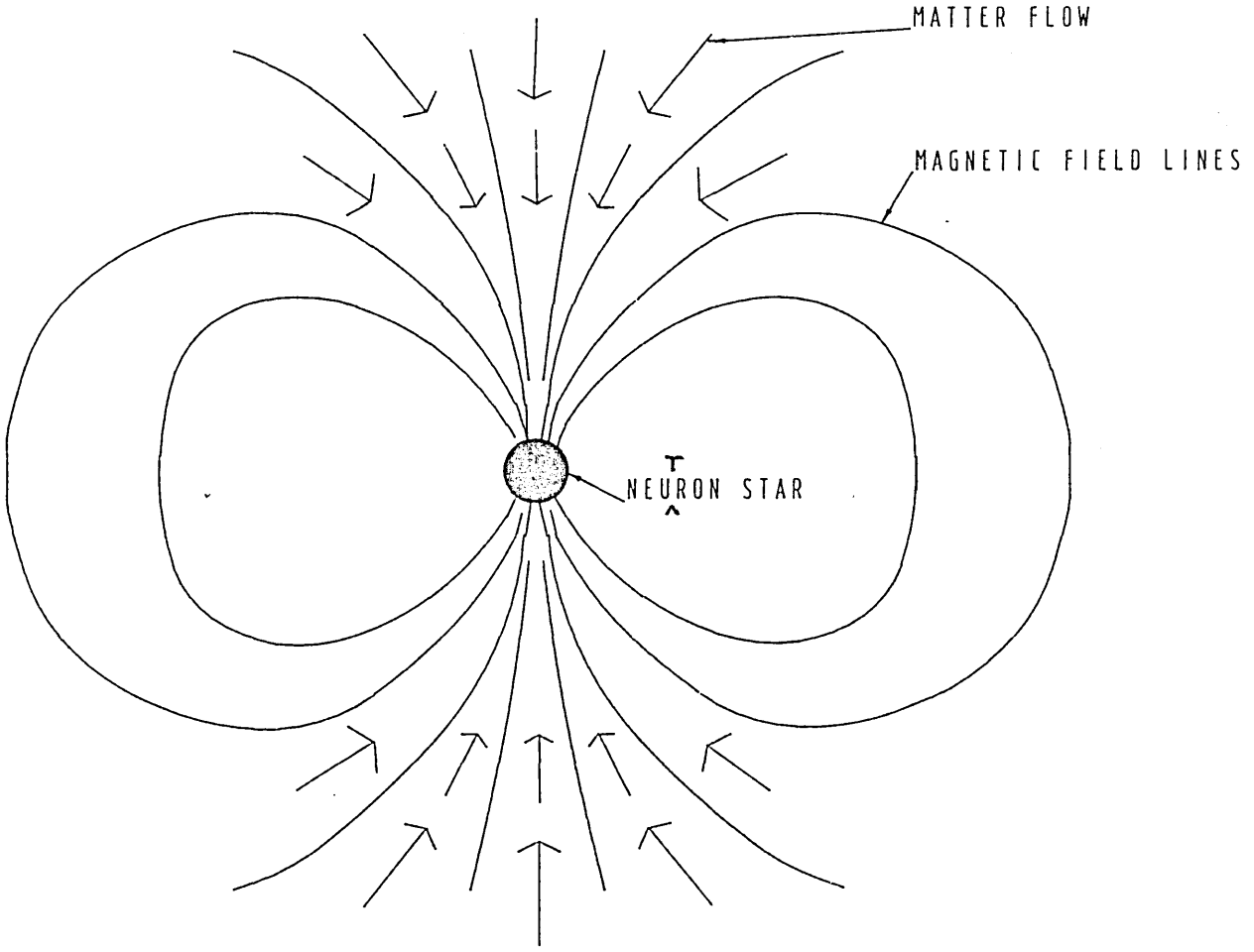

Figure 2.2. Disk Fed accretion and matter flow.

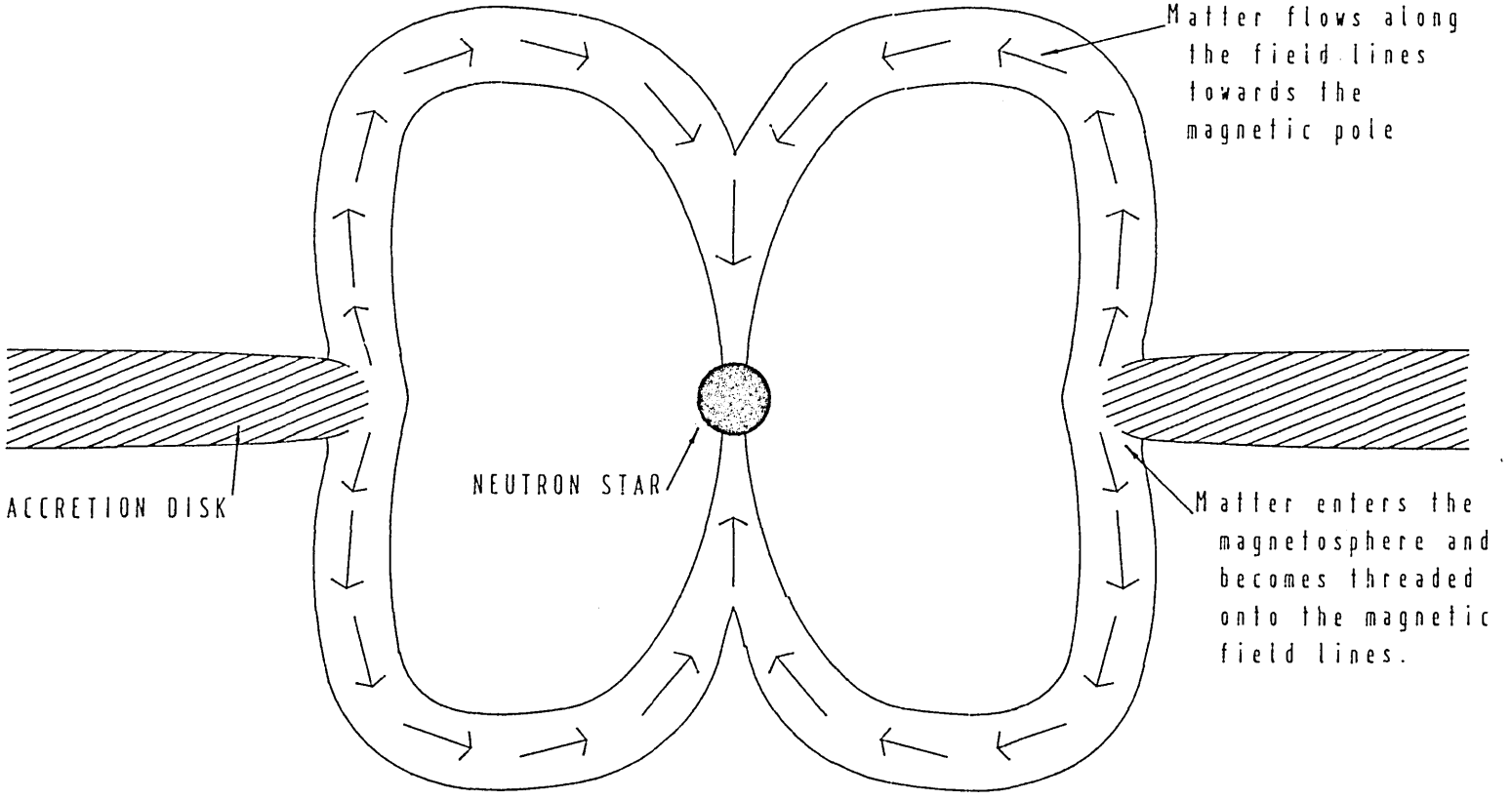

Figure 2.3. Geometry for the calculation of the shape of a closed magnetosphere.

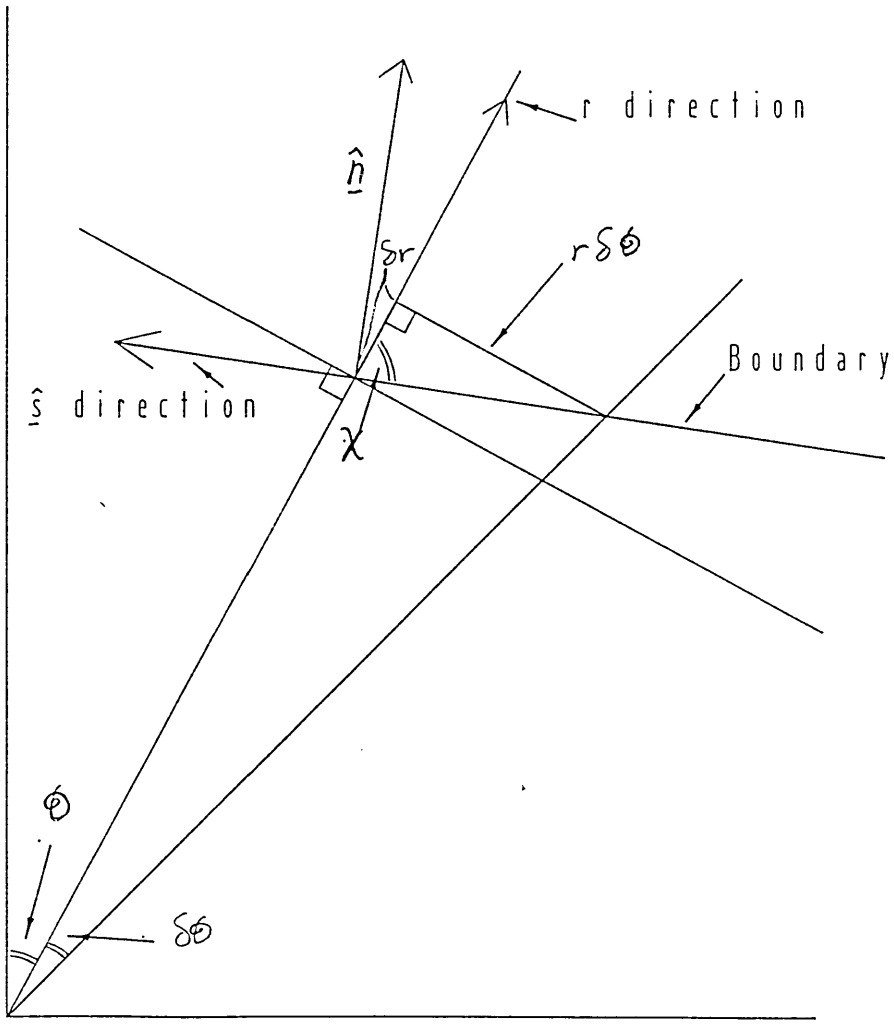

Fig 2.4. Closed magnetosphere--shape as calculated in § *2.2*.

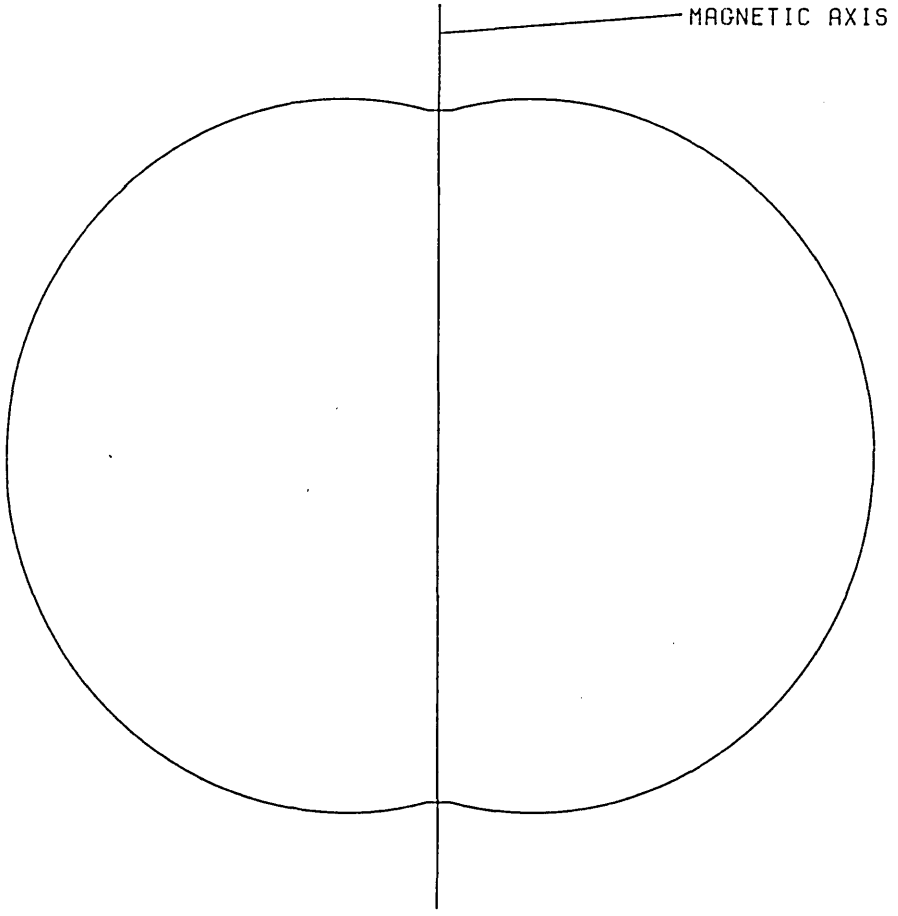

Figure 2.5. The Rayleigh-Taylor Instability.

This occurs when there is a dense liquid or plasma above a less dense liquid or plasma, kept apart by surface tension in the case of a liquid or a magnetic field in the case of a plasma. Any disturbance is likely to be amplified and result in 'blobs' of the denser material falling into the less dense material.

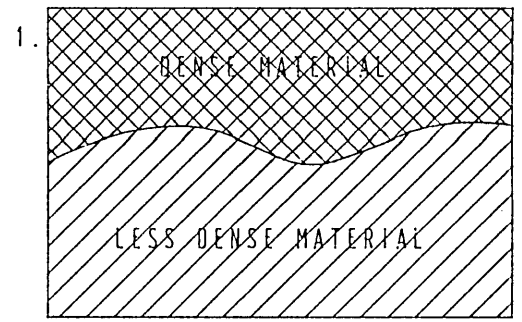

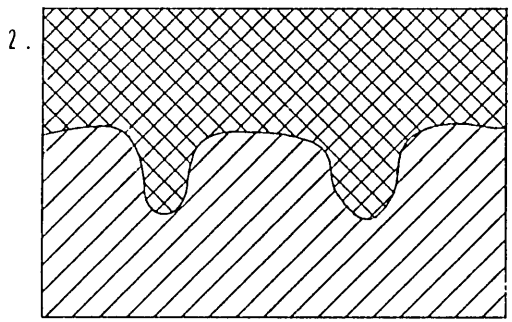

Disturbance becomes magnified.

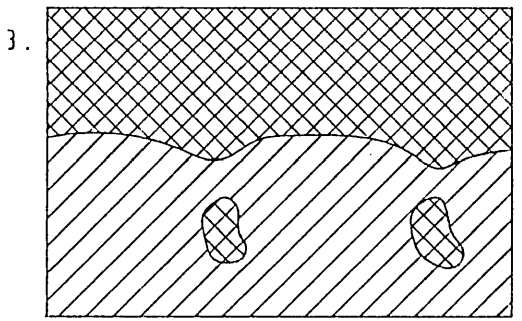

Blobs of dense material fall into less dense material.

Figure 2.6. Plasma Entry through a cusp.

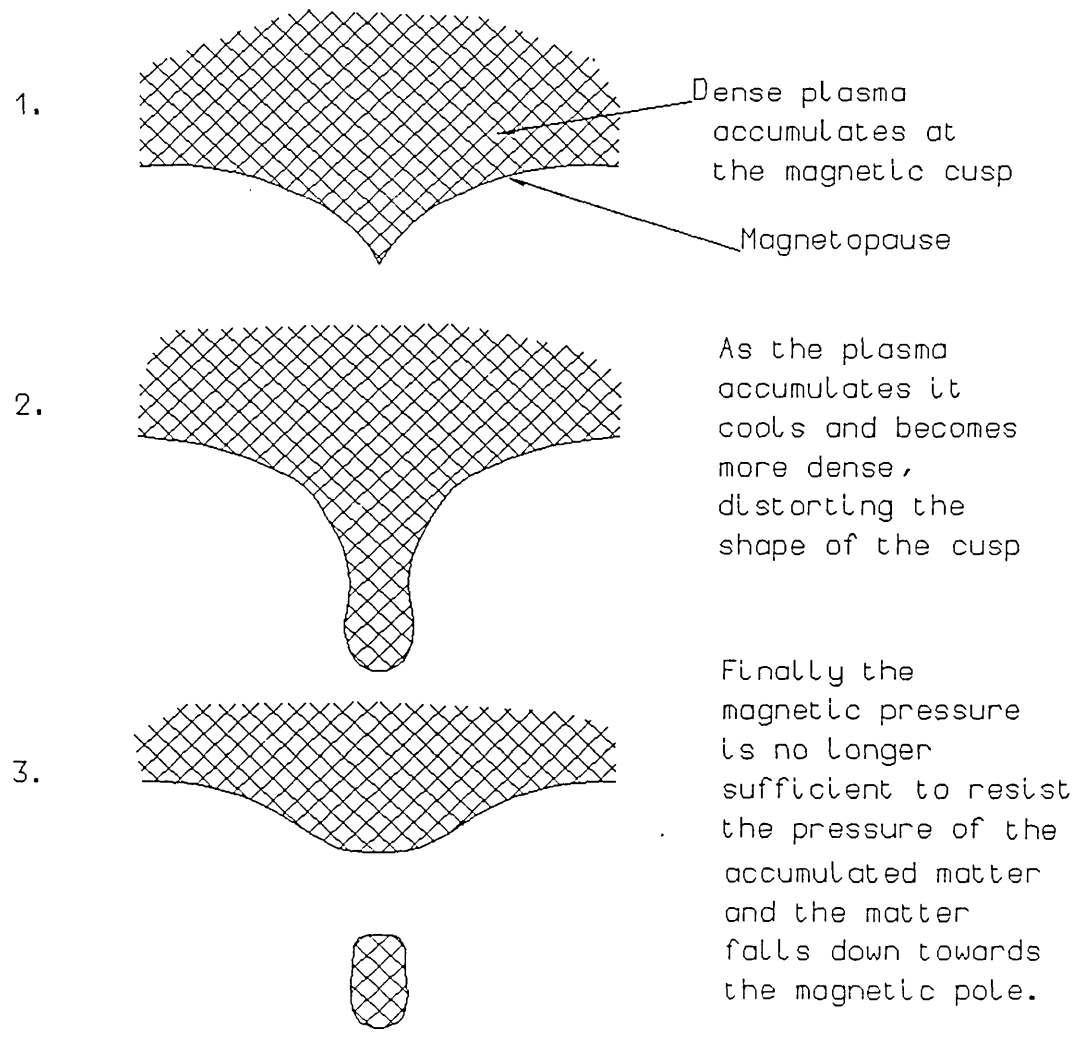

Figure 2.7. Fan beam and wind fed accretion.

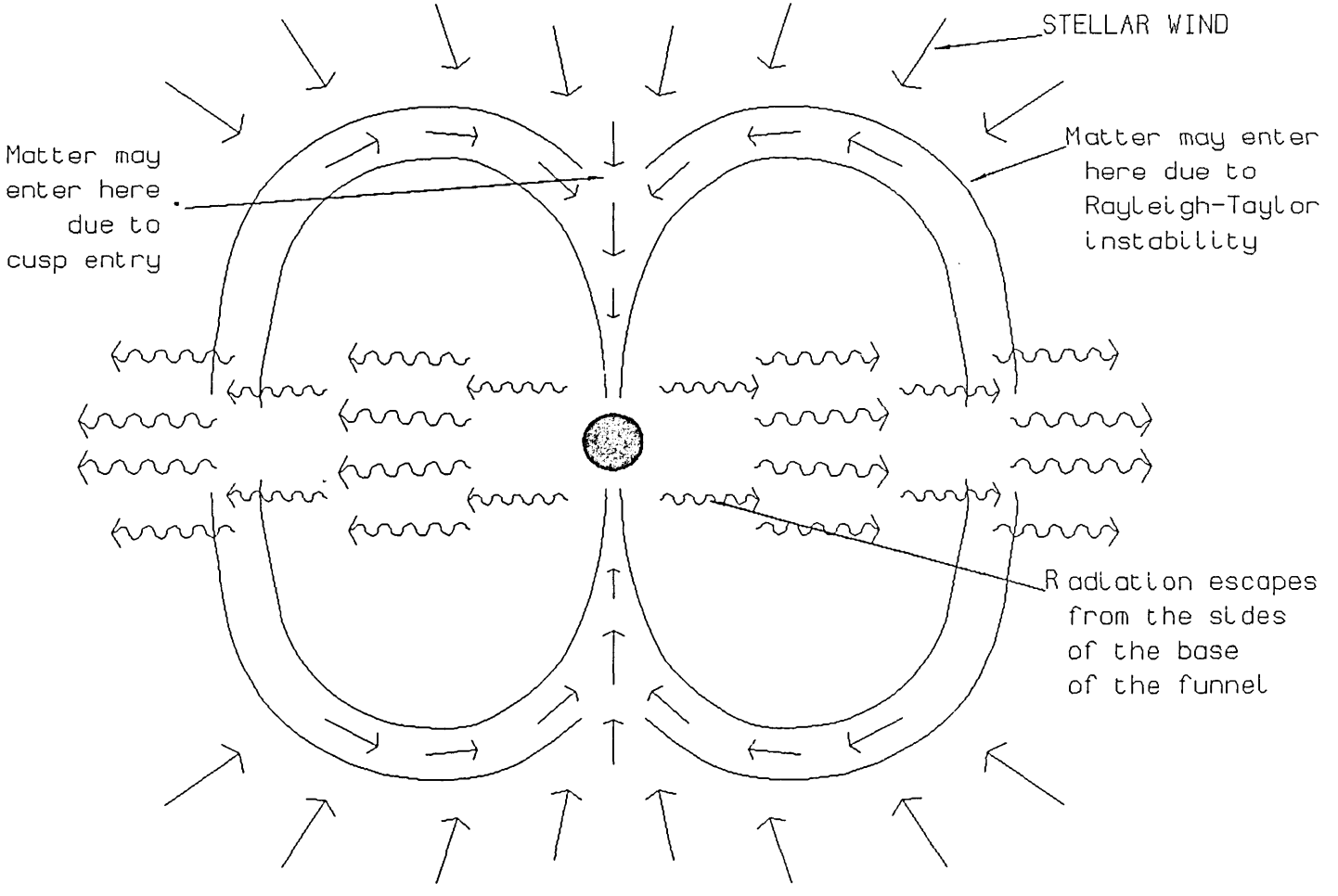

CHAPTER 3.

A model for accretion flow in the outer regions of a neutron star's magnetosphere.

§3.1 Description of the case considered in this chapter.

This chapter models accretion flow along the magnetospheric boundary. Accretion flow is followed along the magnetic field lines from the magnetic equator towards the magnetic pole. Plasma is assumed to enter the magnetosphere by the Rayleigh-Taylor instability in the region near the magnetic equator and become linked to the magnetic field lines. As described in chapter 2, at least some of the plasma is likely to enter the magnetosphere near the magnetic equator when accretion takes place from a wind. It is easier for plasma to enter the magnetosphere by the Rayleigh-Taylor instability in the region near the magnetic equator as the magnetic field lines are less curved. Even if the plasma enters nearer the magnetic pole as indicated in Fig 2.7, unless it enters near the cusp, it must still flow some of the way along the magnetic field lines towards the pole. Also, if accretion takes place from a disk arround the magnetic equator matter must enter the magnetosphere near the magnetic equator. Therefore, for many cases of accretion flow onto a magnetised neutron star flow along the magnetic field lines towards the magnetic pole is worth investigating.

The plasma on entering the magnetosphere penetrates to a certain depth. As mentioned in chapter 2, *Arons + Lea 1976* calculated this depth to be 410km when their magnetospheric radius was 2400km. This represents 17% of the magnetopheric radius. Therefore, it is reasonable to consider the plasma flowing towards the pole as confined to a flux tube with a thickness of between 410km and 20% of the magnetospheric radius at the magnetic equator. At the equator the flux tube is assumed to have a cross-sectional area equal to the penetration depth squared. As the plasma is assumed to be linked to the magnetic field lines, the area of these flux tubes is taken to be inversely proportional to the strength of the magnetic field. The simplest way of describing this is in terms of a series of square flux tubes at the magnetospheric boundary surrounding the neutron star. The radius of the magnetosphere is calculated for the case when $B_* = 5 \times 10^{12}$ gauss and $L_x = 3 \times 10^{37} erg\, sec^{-1}$. The radius of the

magnetosphere is not changed for different accretion rates as this allows us to see how the properties of the model vary with for different accretion rates and radiation output temperatures without it being further complicated by differing magnetospheric radii. Also, the magnetospheric radius varies slowly with the accretion rate, i.e. as $(1/\dot{m})^{2/7}$.

Accretion flow along the flux tubes is assumed to have a velocity equal to ξv_{ff} at the magnetic equator, i.e. it is assumed that when the matter enters the magnetosphere it has a fraction ξ of the free fall velocity in the direction travelling towards the magnetic pole.

The matter is assumed to be a plasma consisting of fully ionised hydrogen. The flow of plasma is treated hydrodynamically. A separate equation for the electron energy is given below in order to allow for the possibility that the electron and proton temperatures are not equal. As shown below it is unnecessary to calculate the electron temperature separately, as the coulomb scattering process is fast enough in order for the electron and proton temperatures to be approximately equal throughout. Also, viscosity and thermal conductivity are neglected.

The plasma is also assumed to be heated by radiation coming from the sides of the bottom of an accretion funnel. Energy exchange between the plasma and the radiation is by Bremsstrahlung and Compton scattering.

The geometry used is the same as that shown in Fig 2.3 and the shape of the magnetospheric boundary is that calculated in §2.2 and shown in Fig 2.4. The magnetic equator is assumed to be surrounded by flux tubes of width d (equal to the penetration depth of the plasma). The plasma flows along these flux tubes towards the magnetic pole. The fraction of the equator surrounded by flux tubes is taken as equal to α, alpha is usually taken as being equal to 1, but the flow for $\alpha \ll 1$ is also calculated. The mass flow down 1 tube ($\dot{m}$) is calculated as follows. The number of tubes N_t is given by:–

$$N_t = \frac{2\pi r_m}{d} \times 2\alpha$$

the luminosity L_x is given by

$$L_x = N_t \frac{GM\dot{m}}{r_\star}$$

Therefore,

$$\dot{m} = \frac{r_\star L_x d}{4\pi r_m GM\alpha}$$

At the equator the matter is assumed to be flowing along the flux tube with a velocity equal to $\xi\sqrt{\frac{2GM}{r_m}}$.

The general picture of the model described in this chapter is shown in Fig 3.1.

§3.2 Equations describing the flow.

The variables used in the equations below are as follows:–

G	=	gravitational constant
M	=	mass of star
$\dot{m}$	=	mass flow down 1 flux tube
A	=	cross-sectional area of 1 flux tube
v	=	flow velocity along the flux tube
ρ	=	density ($g\,cm^{-3}$)
s	=	distance coordinate
r	=	distance from centre of star
χ	=	angle between radius vector and normal to s
P_g	=	gas pressure
P_e	=	electron pressure
P_p	=	proton pressure
T_e	=	electron temperature
T_p	=	proton temperature
L_x	=	luminosity
Λ_C	=	energy flow from protons to electrons
Λ_R	=	energy flow from electrons to radiation
Λ_B	=	Bremsstrahlung
Λ_{Co}	=	Compton scattering
κ_T	=	Opacity due to Thomson scattering
m_e	=	electron mass
m_p	=	proton mass
β	=	$m_e/(m_e+m_p)$
r_m	=	radius of the magnetosphere
$r_\star$	=	neutron star radius
r	=	radius (from centre of neutron star)
λ	=	latitude

d = penetration depth of the plasma (at r_m)

Mass conservation.

$$\rho v A = \dot{m}$$

where $\dot{m}$ is constant, and refers to the mass flow down one tube of cross sectional area A, which at the magnetic equator is equal to d^2.

Momentum equation.

$$\rho v \frac{dv}{ds} = \rho \frac{GM}{r^2} \cos\chi - \frac{dP_g}{ds} - \kappa \rho U_x \cos\chi$$

Gas energy equation.

It is worth noting that the gas consists of protons and electrons.

$$\nabla . \left(\rho \mathbf{v} \frac{v^2}{2} + \frac{5}{2} \mathbf{v} P_g \right) = \mathbf{v} . \mathbf{F}_{gas} - \Lambda_R$$

where $\mathbf{F}_{gas}$ is the force on the gas exerted by the radiation and the gravitational force. If the radiation is assumed to be flowing outwards in the $\hat{\mathbf{r}}$ direction the force $\mathbf{F}_{gas}$ is given by:-

$$\mathbf{F}_{gas} = -\rho \frac{GM}{r^2} \hat{\mathbf{r}} + \kappa \rho U_x \hat{\mathbf{r}}$$

Electron energy equation.

$$\nabla . \left(\rho_e \mathbf{v} \frac{v^2}{2} + \frac{5}{2} \mathbf{v} P_e \right) = \mathbf{v} . \mathbf{F}_e - \Lambda_R + \Lambda_C$$

$\mathbf{F}_e$ is the force exerted on the electron component of the gas and is given by:-

$$\mathbf{F}_e = -\beta \rho \frac{GM}{r^2} \hat{\mathbf{r}} + \kappa \rho U_x \hat{\mathbf{r}}$$

It is worth noting that the radiative force acts on the electrons as it is due to Compton scattering of the electrons.

Λ_R is the rate of energy flow from electrons to photons, i.e. it is the rate at which thermal energy of the electrons is converted into radiative energy. Λ_R is expressed as energy exchange per unit volume. Energy exchange between electrons and photons takes place due to inverse Compton scattering and Bremsstrahlung.

The component of Λ_R due to Compton scattering (Λ_{Co}) is given by:–

$$\Lambda_{Co} = 20.22\kappa\rho U_x(T_e - T_r)$$

where κ is the Thomson cross-section σ_T divided by the proton mass. This expression for the energy exchange due to Compton scattering is given in *Weyman 1965.*

The component of Λ_R due to Bremsstrahlung (Λ_B) is

$$\Lambda_B = 5.1 \times 10^{20}\rho^2 T_e^{1/2}\left(1 - \frac{U_x}{aT_r^4}\frac{T_r}{T_e}\right)$$

$$\Lambda_R = \Lambda_B + \Lambda_{Co}$$

The energy exchange between protons and electrons Λ_C is given by the Coulomb exchange term:–

$$\Lambda_C = 4.9 \times 10^5 \frac{\rho^2}{T_{eff}^{3/2} m_p} \ln\Lambda\,(T_p - T_e)$$

where $\ln\Lambda$ is the Coulomb logarithm:–

$$\ln\Lambda = \ln\left(\frac{1.6 \times 10^{-8} T_e^{3/2}}{\rho^{1/2}}\right)$$

This is given in *Spitzer 1956.*

§3.3. Radiation input to the flux tube.

This section calculates the radiation energy density U_x due to radiation from the bottom of an accretion funnel at the magnetic pole. Also, other properties connected with radiative input to the flux tube are considered including opacity.

The radiation energy density in the flux tube is assumed to be due to the radiation emitted from the sides of a shallow cylinder at the bottom of the accretion funnel, see Fig 3.2. The radius of the neutron star and the radius of the cylinder emitting radiation are small compared to the radius of the magnetosphere; therefore the radius of the star and cylinder are taken to be infinitely small. The radiation density at the flux tubes is dependent on r and λ where λ is the latitude as shown in Fig 3.2.

The radiation density is proportional to the effective area seen at the flux tube at latitude λ, therefore from looking at Fig 3.2 it is clear that the radiation energy density or flux is proportional to $\cos\lambda$. The radiation density follows an inverse square law after this initial anisotropy, thus the radiative flux at given r and λ is given by:–

$$F(r,\lambda) = \frac{K}{r^2}\cos\lambda \; erg\, cm^{-2} sec^{-1}$$

In order to find K, it is necessary to integrate this flux over 1 hemisphere and set it equal to $L_x/2$. The geometry for doing this is given in Fig 3.3.

The total radiative flux through a ring at latitude λ that subtends an an angle $\delta\lambda$ is calculated. This is equal to $F_{ring}(r,\lambda)$ and is equal to the area of the ring multiplied by the radiation flux per unit area of the ring

$$\begin{aligned} F_{ring}(r,\lambda) &= 2\pi r \sin(90-\lambda) r\delta\lambda \frac{K}{r^2}\cos\lambda \\ &= 2\pi K \cos^2\lambda\, \delta\lambda \end{aligned}$$

The total radiation flux through this hemisphere of radius r is calculated by integrating over all rings for λ between 0 and $\pi/2$. This is set equal to $L_x/2$:–

$$\frac{L_x}{2} = 2\pi K \int_0^{\pi/2} \cos^2\lambda \, d\lambda$$

This gives a radiation flux $F_x(r,\lambda)$ at the flux tube:–

$$F_x(r,\lambda) = \frac{L_x}{\pi^2 r^2}\cos\lambda$$

Therefore the radiaton energy density is given by:–

$$U_x(r,\lambda) = \frac{L_x}{\pi^2 r^2 c}\cos\lambda$$

This expression for U_x is used in the equations in §3.2 to allow for radiative heating of the plasma flowing along the flux tubes.

The optical depth of a plasma is $\kappa\rho L$ where L is the length of the region considered. The optical depth of the flux tube seen by the radiation τ is given by:–

$$\tau \sim \kappa\rho\sqrt{A}/\sin\chi$$

which is clear from looking at Fig 3.4. If the optical length becomes greater than 1 significant scattering has occurred. If it is not much greater than 1 then the radiation density calculated above $U_x(r,\lambda)$ remains a reasonable approximation to the radiation density in the flux tube, as although the radiation has scattered a large proportion of the radiation energy has not been converted into thermal energy of the gas.

§3.4. Exclusion of the electron energy equation.

In this section it is shown that energy exchange between protons and electrons due to Coulomb scattering is fast enough such that it may be assumed that $T_e = T_p$. If the temperatures can be assumed to be equal then only the gas energy equation is necessary. The expression for the density ρ at the equator is derived from mass conservation and the expression given in §3.1 for $\dot{m}$, i.e.

$$\rho_{r_m} = \frac{r_* L_x}{2\pi r_m^{1/2}(2GM)^{1/2}\xi\alpha}$$

The Coulomb exchange term, Λ_C, is the energy flow from protons to electrons per unit volume per unit time. For order of magnitude purposes, the thermal energy density per unit volume of the electrons is $\frac{3}{2}\frac{\rho}{m_p}k_B T_e$; therefore, for a given ρ

$$\frac{3}{2}\frac{\rho}{m_p}k_B\frac{dT_e}{dt} = 4.9\times10^5\frac{\rho^2}{T_e^{3/2}m_p}\ln\lambda(T_p - T_e)$$

This gives an equation of the form:–

$$\frac{dT_e}{dr} = C_C\frac{(T_p - T_e)}{T_e^{3/2}}$$

as the intention is to calculate the order of magnitude of the time scale this is simplified to solving

$$\frac{3}{2}\frac{dT_e}{dt} = C_C T_e^{-1/2}$$

which gives

$$\Delta t_C \sim \frac{T_e^{3/2}}{C_C} = \frac{T_e^{3/2} k_B}{4.9 \times 10^5 \rho \ln \Lambda}$$

The maximum value for Δt_C is given for minumum ρ and maximum T_e. The minimum ρ is where $\xi = 1$ and maximum T_e where $T_e = T_r\,(= 10keV)$. This gives a value for $\Delta t_{C\,max} = 9 \times 10^{-3} sec$. It is also worth noting that Δt_C decreases with both decreasing T_e and increasing ρ. Therefore if at this point this value for Δt is less than the time scale of other processes it is a reasonable approximation to assume that $T_e = T_p$.

A similar calculation of the time scale for Bremsstrahlung gives

$$\Delta t_B = 8.1 \times 10^{-14} \frac{T_e^{1/2}}{\rho}$$

which in the region near the magnetic equator gives a value of $\Delta T_B = 0.5 sec$, again proportinal to ρ; and Compton heating gives a value of 0.1 sec, independent of ρ. Also the distance over which plasma travels at its maximum velocity in the maximum time scale for Coulomb heating is $\sqrt{\frac{2GM}{r_m}} \Delta t_{max} = 5.2 \times 10^6 cm \sim 6.8 \times 10^{-3} r_m$. Therefore it is a reasonable approximation to assume that $T_e = T_p$.

Cyclotron emission is also ignored. The formula for the time scale of orbit decay due to cylotron emission given in *Katz 1986* was applied to the magnetic field strengths in the region considered. This gave a time scale for orbit decay in the outer regions of the magnetosphere of $\sim 0.8 sec$; which is independent of plasma density and temperature and is much longer than the time scales of the other radiation processes.

§3.5. Rearrangement of the equations for solution.

The term $\nabla.(\,)$ in the energy equation is expressed as follows:-

$$\nabla.(\,) = \frac{1}{A}\frac{d}{ds}A(\,)$$

as we are consdering the divergence of the flow as it is flowing along a flux tube of cross-sectional area A. Also, $\mathbf{v}.\hat{\mathbf{r}}$ is required. This is given by noting that $\mathbf{v}$ is in the $\hat{\mathbf{s}}$ direction, therefore $\mathbf{v}.\hat{\mathbf{r}} = -v\cos\chi$. If the gas energy is rewritten in its component parts, using $\rho v A = \dot{m}$, and substituting for dv/ds from the momentum equation the expression for dP_g/ds given below is obtained.

$$\frac{dP_g}{ds} = \frac{1}{\left(\frac{3}{2\rho} - \frac{5P_gA^2}{2\dot{m}^2}\right)} \times \left[\frac{-5P_gA}{2\dot{m}v}\left(\frac{GM}{r^2} - \kappa U_x\right)\cos\chi - \frac{5P_g}{2\rho A}\frac{dA}{ds} - \frac{A}{\dot{m}}\Lambda_R\right]$$

Similar rearrangement, but this time eliminating the pressure gradient gives the following expression for dv/ds.

$$\frac{dv}{ds} = \frac{1}{\left(\frac{3}{2}v - \frac{5AP_g}{2\dot{m}}\right)} \times \left[-\frac{3}{2}\left(\frac{GM}{r^2} - \kappa U_x\right)\cos\chi + \frac{5vP_g}{2\dot{m}}\frac{dA}{ds} + \Lambda_R\frac{A}{\dot{m}}\right]$$

Therefore we have a system of 2 first order ordinary differential equations

$$\frac{dv}{ds} = F_1(s, v, P_g)$$
$$\frac{dP_g}{ds} = F_2(s, v, P_g)$$

This is because at any given s all other terms are known or can be calculated.

§3.6. Method of solution.

The equations in §3.5 are in the form of a system of 2 first order ordinary differential equations, and can therefore be solved using a standard method. The problem is defined to be an initial value problem, the equations being followed from the equator towards the pole. The equations were solved numerically using the 1 step second order implicit scheme, see for example *Potter 1973.* An implicit scheme involves a predictor-corrector pair. This was simply carried out by taking the value at the nth step for the predictor (effectively the predictor was the Euler method) and correcting to convergence. This scheme was chosen as it is simple to program, only the resulting variables from the previous step forward are needed for the calculation of the next step forward. This one step method was also chosen in preference to a library routine as the step length could be set by the program, rather than the step length being chosen and varied by the library routine. This is important as the values for r, λ and χ are also calculated at each step before the calculation of the next value of v and P_g.

Calculation of $\int \Lambda_B A \, ds$ from the equator (where s=0), to the end of the computation was carried out. This was multiplied by the number of flux tubes to give a value for the total radiation emitted from the outer region.

The ratio of the gas pressure to the magnetic pressure was also calculated as the computation proceeded. This is important as the plasma is assumed to be confined by the magnetic pressure. The magnetic pressure is $B^2/8\pi$. This and various other variables and parameters were printed out at each run of the program. Some variables were written to a file in order to be later used in a program to plot graphs of the results. A description of the implicit 1 step method is given in Appendix 1.

§3.7. Results of the Computations.

The program was run for a wide variety of input conditions, a sample of the results being shown in Figs 3.5 to 3.10. Fig 3.5 shows the result for a lower luminosity ($L_x = 1 \times 10^{37} erg\, sec^{-1}$) computation in which the plasma density is so low that cooling due to Bremsstrahlung is suppressed. The plasma in this case heats up to beyond the temperature of the radiation as heating due to adiabatic compression is also occuring, and is faster than the emission processes. Fig 3.6 to 3.8 show the results for computations when $L_x = 3 \times 10^{37} erg\, sec^{-1}$. Comparing Figs 3.6 and 3.7 shows how changing the proportion of the equator surrounded by flux tubes effects the flow. Fig 3.7 shows that when the density is higher cooling due to thermal Bremsstrahlung becomes more effective and the electron temperature profile follows the radiation density profile. Comparing Fig 3.8 to Fig 3.6 shows how changing the input velocity effects the flow. Fig 3.9 is for the case where the X-ray luminosity is $3 \times 10^{38} erg\, sec^{-1}$ which is just super-Eddington. The input velocity along the flux tubes is taken as equal to the free fall velocity and the plasma flows along the flux tube to the magnetic pole. In this case the gas temperature profile closely follows the radiation density profile. For the case shown in Fig 3.10. where the input velocity was taken equal to half the free fall velocity the plasma slowed down and did not reach the magnetic pole.

The ratio of the radiation emitted in the outer regions to the total luminosity was found to be $1 \times 10^{-4} \rightarrow 3 \times 10^{-3}$, for a wide variety of parameters of the model.

The ratio $P_{ratio} = P_g/P_B$ where the magnetic pressure $P_B = B^2/8\pi$ was noted as the runs of the model proceeded. In the cases where $L_x = 1 \times 10^{37}$ and 3×10^{37} and ξ and α were equal to 1 then this ratio was less than 1. For $L_x \sim 3 \times 10^{37}$ and no more than one of ξ and α being $\ll 1$; then this ratio remained less than one except for over a fairly short distance. If both ξ and α were $\ll 1$ then $P_{ratio} \geq 1$. Also, when $L_x \geq 10^{38} erg\, sec^{-1}$, $P_{ratio} \gg 1$: in the case shown in Fig 3.9. where the luminosity is just super-Eddington this ratio was ~ 8. To see if this ratio could be reduced for luminosities that just exceed the Eddington luminosity the program was run for the case when $L_x = 3 \times 10^{38} erg\, \mathrm{sec}^{-1}$, with $\alpha = \xi = 1$, and the width of the flux tube =20% of the magnetospheric radius; which is over 3 times the depth used in the other

computations. For this case $P_{ratio} \sim 2$ throughout.

For all computations, the optical length across the flux tube $\tau \leq 0.5$.

§3.8. Conclusions.

This very simple initial value approach to the hydrodynamic flow in the outer region of the magnetosphere allows us some insight into the flow in this region. It shows how for low density plasma flow cooling processes are not very effective, which means that the gas temperature profile can be greatly influenced by the starting temperature of the plasma with adiabatic heating playing a major role. For higher plasma densities cooling due to thermal Bremsstrahlung plays a major role and therefore the plasma temperature is lower and follows the radiation density profile. This is not dissimilar from the conditions assumed by *Wandel et al 1984* in their spherically symmetric case.

The amount of radiation emitted by these outer regions was $1 \times 10^{-4} \rightarrow 3 \times 10^{-3}$ times the total luminosity of the source. This small fraction shows that emission from flow in the outer regions is small and therefore cannot be a major contribution to the emission spectrum. The fact that the plasma temperature is in the *keV* energy range shows that this outer region does not form a source of radiation at other frequencies. Also, this fraction remains low for all the input parameters used, and does not change substantially when for example the input velocity is reduced. This indicates that these conclusions may be valid for a wider range of conditions than described by this model. The small fraction of the total luminosity emitted by this flowing plasma also indicates that in sources where substantial reprocessing takes place it must occur in plasma that has not yet entered the magnetosphere, or possibly in plasma that is flowing much more slowly than that in our case. The fact that in all our calculations the optical depth across the tube remained less than 1 is further support of these conclusions.

In the cases of higher luminosity and when the input values of ξ and α are set less than 1 then the ratio of the gas pressure to the magnetic pressure becomes greater than 1. When this occurs the plasma cannot be fully confined by the magnetic field to the flux tubes defined by the model in this chapter. The magnetic field may be increased by the flow of the plasma, the value taken in this chapter is simply that of a dipole. The magnetic field may be doubled in places

as described in chapter 2; if this is the case the plasma may be confined to the flux tubes. If the plasma is not confined to narrow flux tubes a larger number of magnetic field lines may have matter flowing along them, thus creating funnel geometry rather than annulus geometry (see §4.2).

As shown in Fig 3.9, it is possible for the plasma to flow from the equator towards the magnetic pole in the case of accretion rates slightly above the Eddington limit. Whether or not this situation may not occur in nature depends on whether the matter can be directed along the flux tube with a high enough velocity.

The main limitation of these computations is that the method is only appropriate when the plasma is flowing supersonically towards the magnetic pole: the equations as they are set up are invalid for low velocity flows, and any run of the program for low velocity flows appears to be unstable. It has been assumed that as the inflowing plasma is turned around (from spherically symmetric inflow or from a disk) it retains a large proportion of its kinetic energy. This turning around may be achieved by scattering of the charged particles by the magnetic field; the magnetic field may scatter the charged particles by $\pi/2$ without substantially reducing the velocity.

The model described in this chapter allows us some understanding of the processes occuring in the outer regions of the magnetosphere. A full understanding of the problem of accretion flow in the outer regions would require a very complicated model. In order to model the flow for low starting velocities where the matter is pulled along the flux tubes towards the surface by the gravitational force, and decelerated by the gas pressure gradient would require a complictated boundary value problem to be set up, see for example *Potter 1973*. In order to properly treat the plasma flow such that the plasma is not confined to the flux tubes would be an even more complicated problem, including the modification of the magnetic field by the plasma. A full treatment of the plasma flow in the outer regions may require a time dependent treatment of the hydrodynamic flow problem.

Figure 3.1. Plasma flow in the outer regions of the magnetosphere.

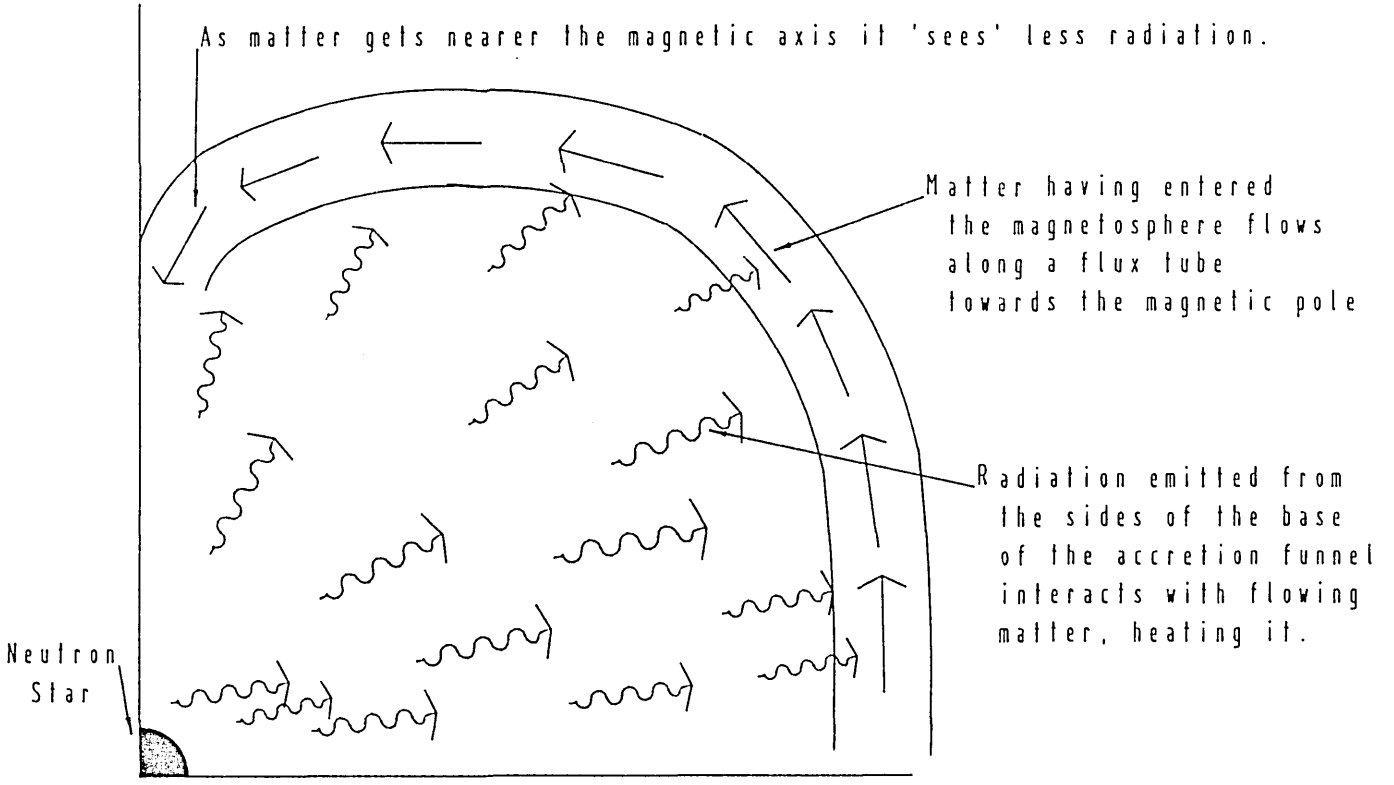

Figure 3.2. Variation of radiation input to flux tube with λ

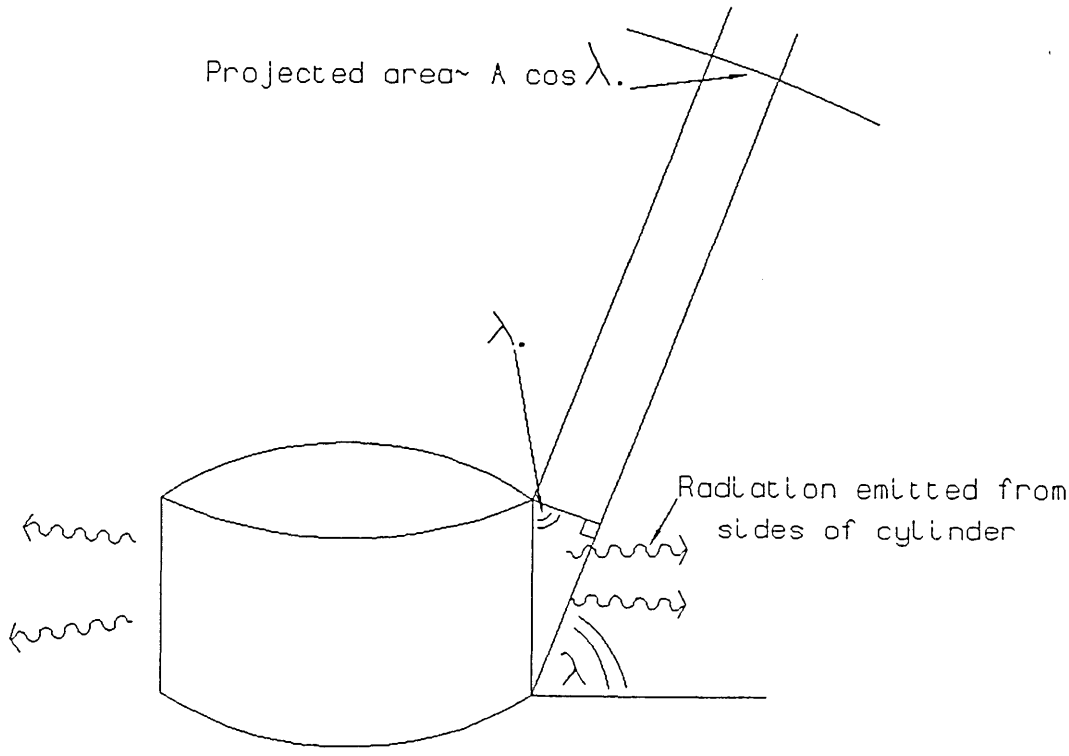

Figure 3.3. Geometry for calculating radiation density at flux tube.

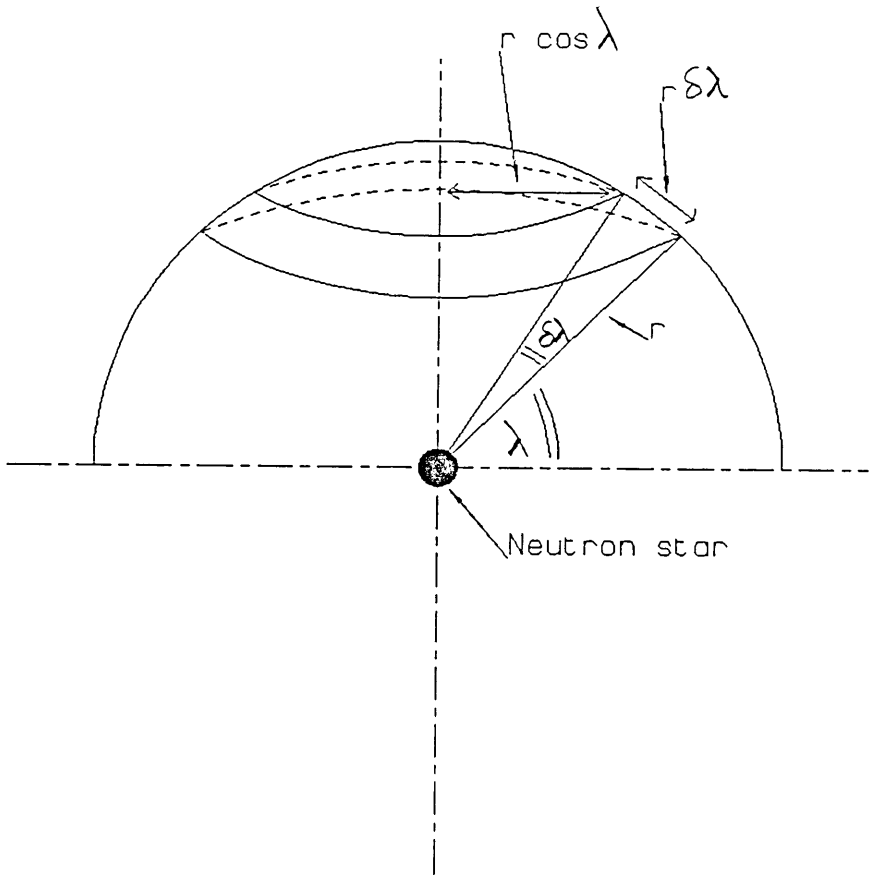

Figure 3.4. Length of matter travelled through by radiation.

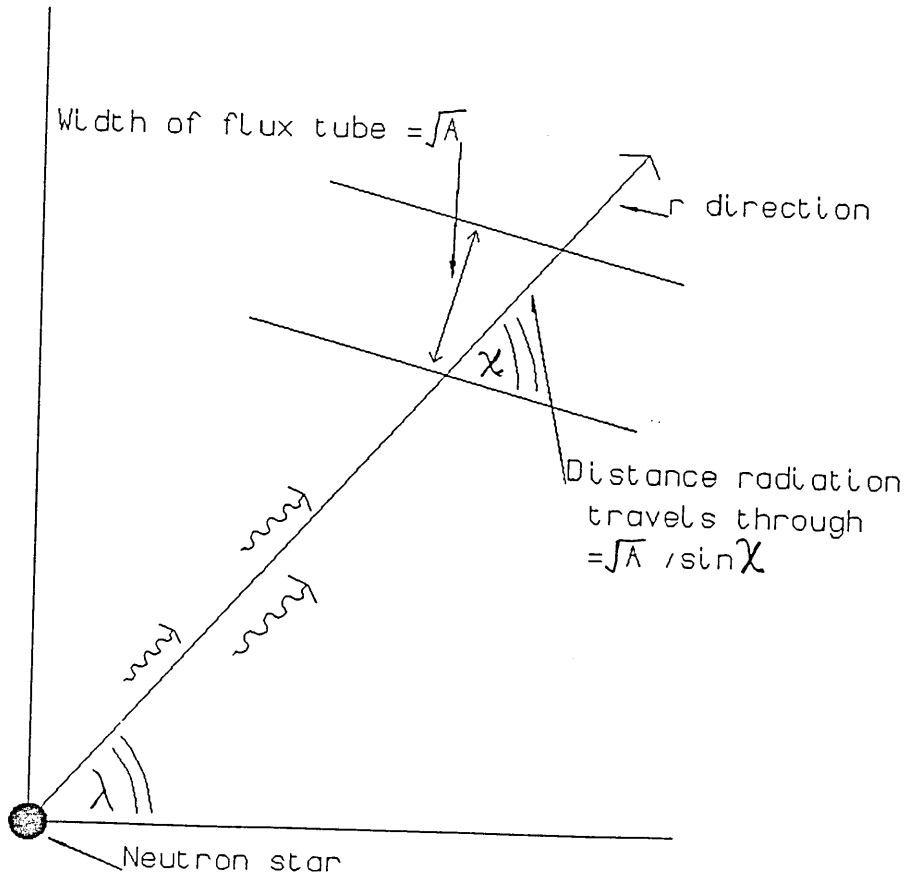

Fig 3.5. Plasma flow in the outer regions of the magnetosphere.

Parameters of this run are:-- $R_m=7.43\times10^8 cm$ $Depth=4.10\times10^7 cm$ $\alpha=1.0$
$L_x=1\times10^{37} erg\ s^{-1}$ ξ(at R_m)=1.0 T_e(at R_m)=3.0keV. T_R=10.0keV

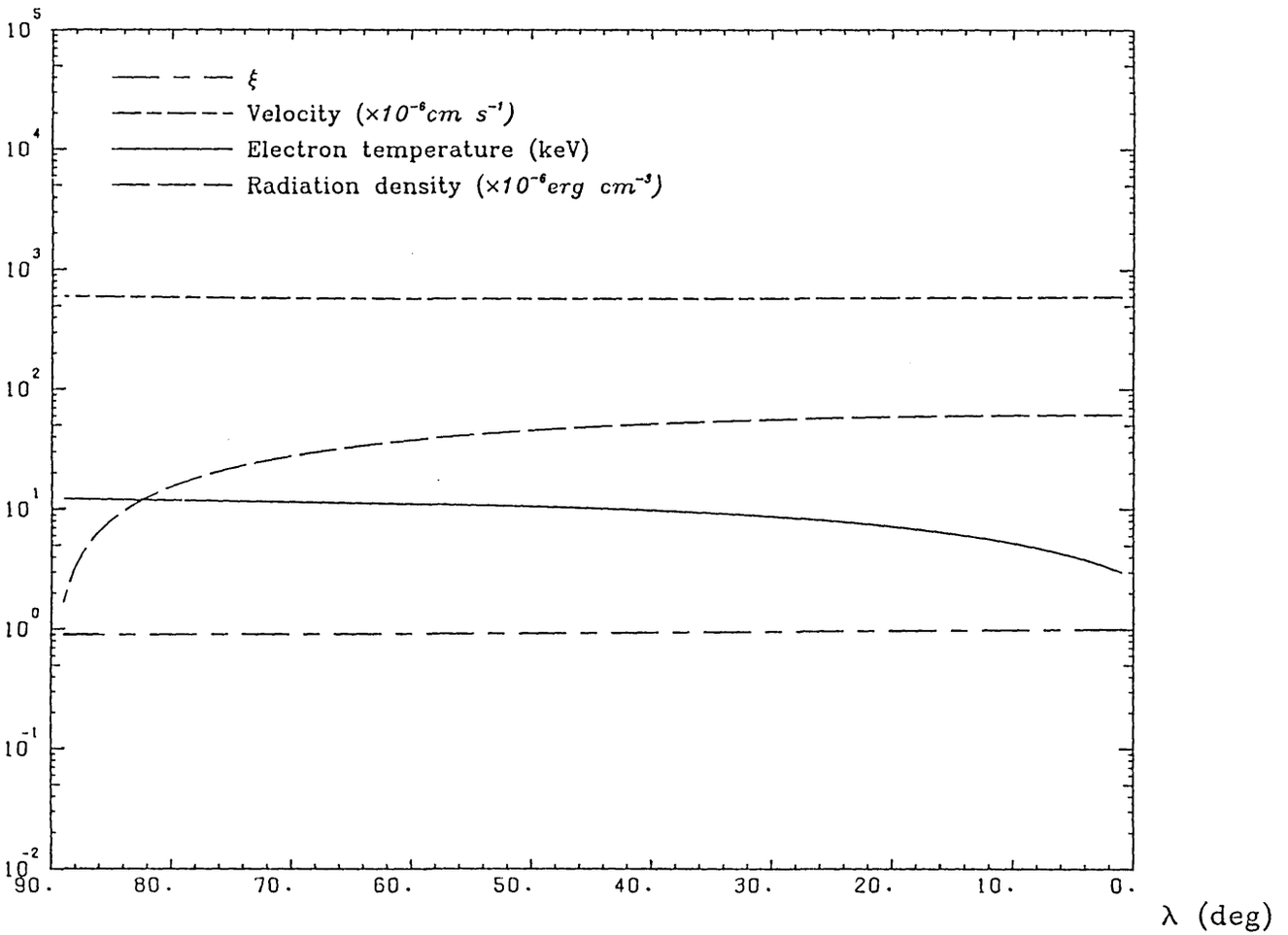

Fig 3.6. Plasma flow in the outer regions of the magnetosphere.

Parameters of this run are:-- $R_m=7.43\times10^8 cm$ $Depth=4.10\times10^7 cm$ $\alpha=1.0$
$L_x=3\times10^{37} erg\ s^{-1}$ ξ(at R_m)=1.0 T_e(at R_m)=3.0keV. T_R=10.0keV.

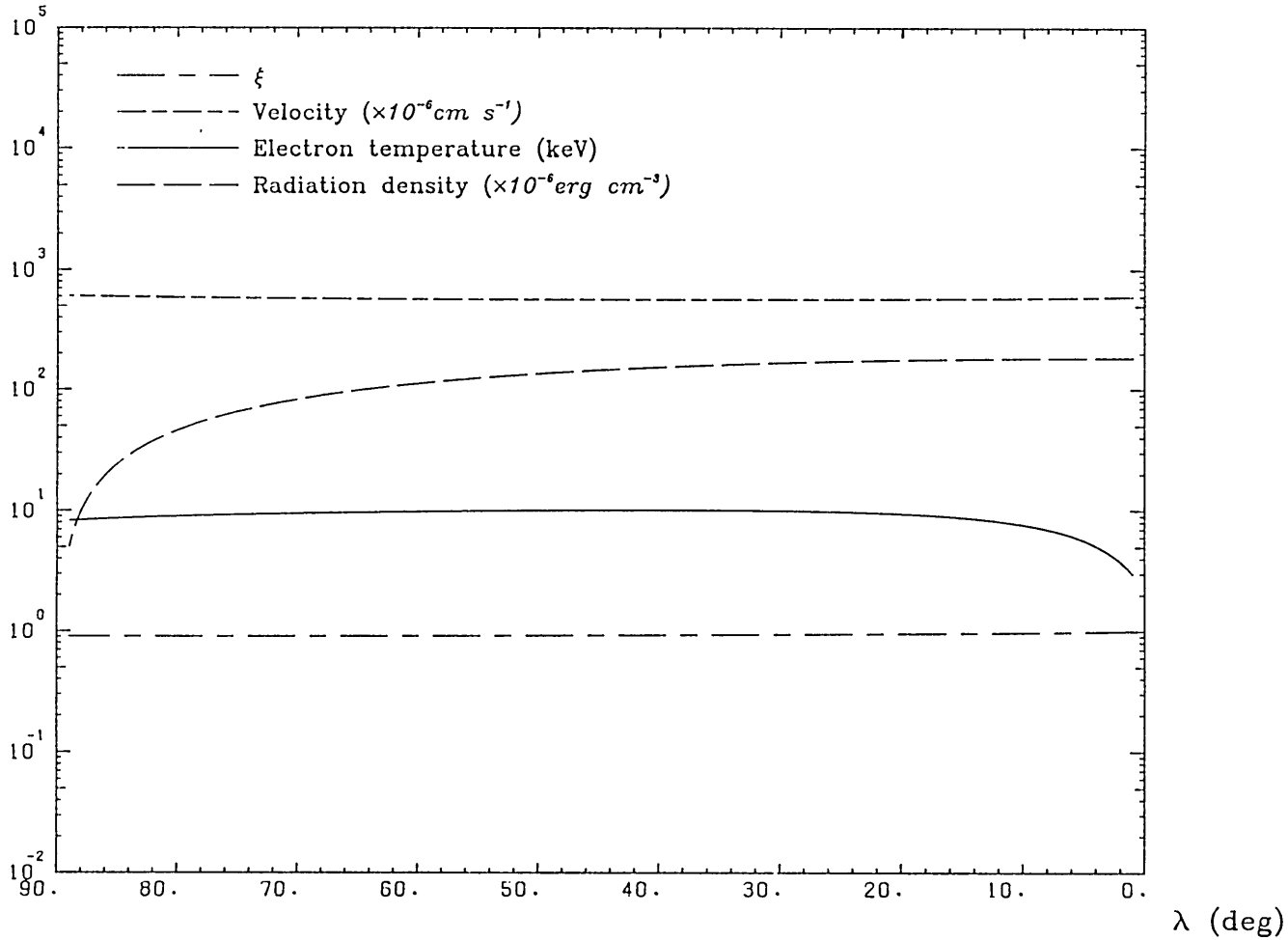

Fig 3.7. Plasma flow in the outer regions of the magnetosphere.

Parameters of this run are:-- $R_m=7.43\times10^8 cm$ $Depth=4.10\times10^7 cm$ $\alpha=0.5$
$L_x=3\times10^{37} erg\ s^{-1}$ ξ(at R_m)=1.0 T_e(at R_m)=6.0keV. T_R=10.0keV.

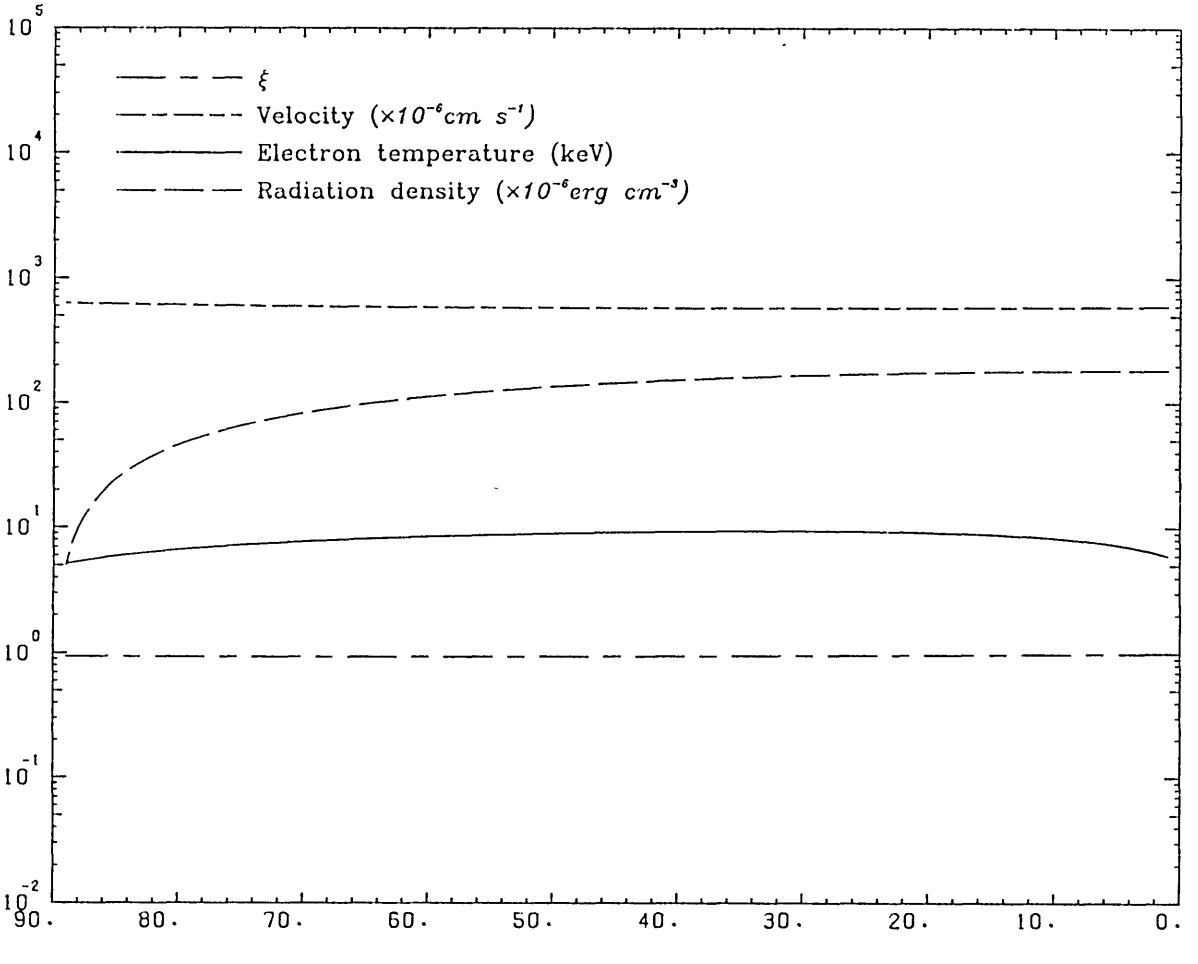

Fig 3.8. Plasma flow in the outer regions of the magnetosphere.

Parameters of this run are:-- $R_m=7.43\times10^8 cm$ $Depth=4.10\times10^7 cm$ $\alpha=1.0$
$L_x=3\times10^{37} erg\ s^{-1}$ ξ(at R_m)=0.5 T_e(at R_m)=6.0keV. T_R=10.0keV.

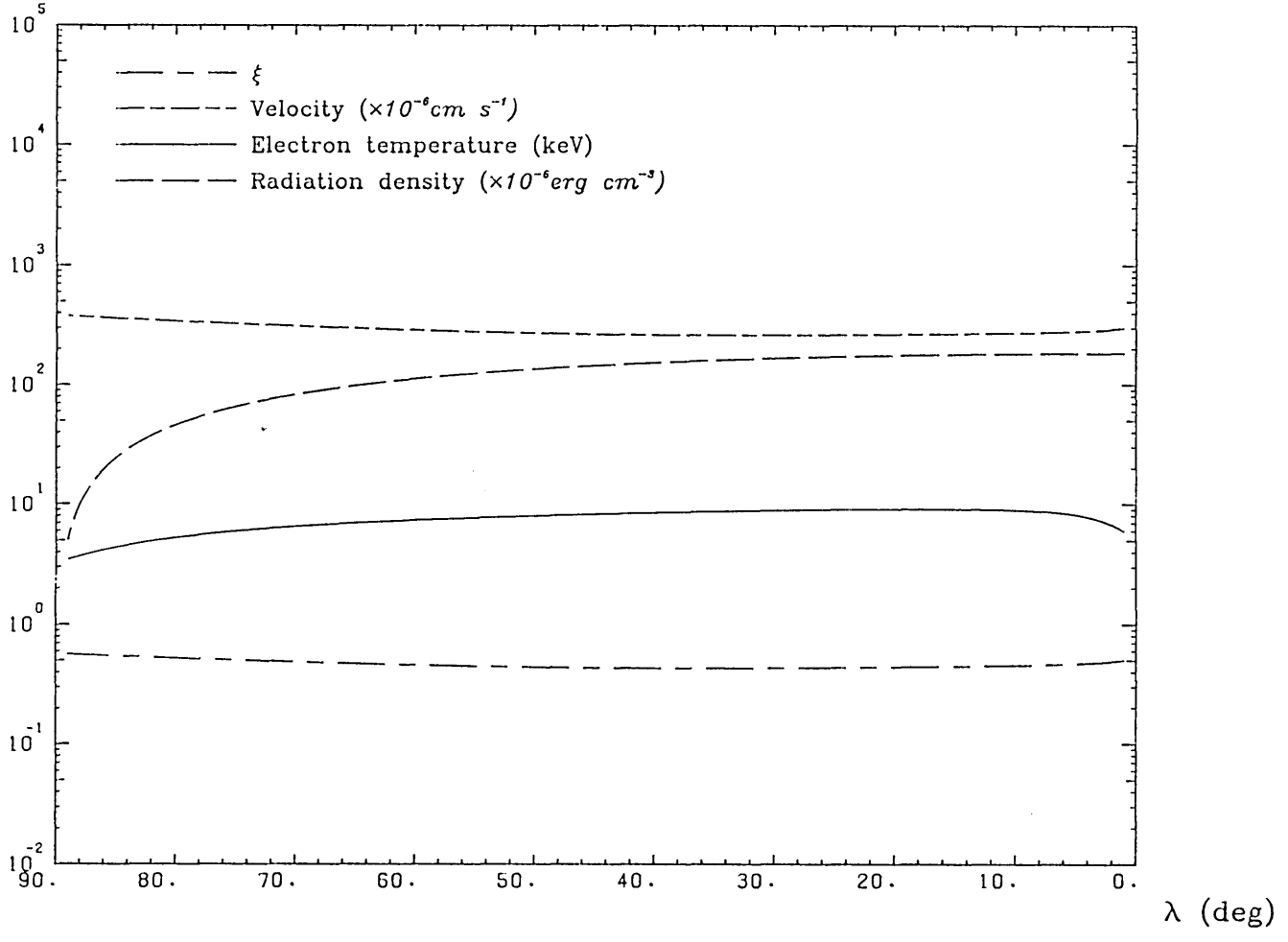

Fig 3.9. Plasma flow in the outer regions of the magnetosphere.

Parameters of this run are:-- $R_m=7.43\times10^8 cm$ $Depth=4.10\times10^7 cm$ $\alpha=1.0$
$L_x=3\times10^{38} erg\ s^{-1}$ ξ(at R_m)=1.0 T_e(at R_m)=6.0keV. T_R=10.0keV

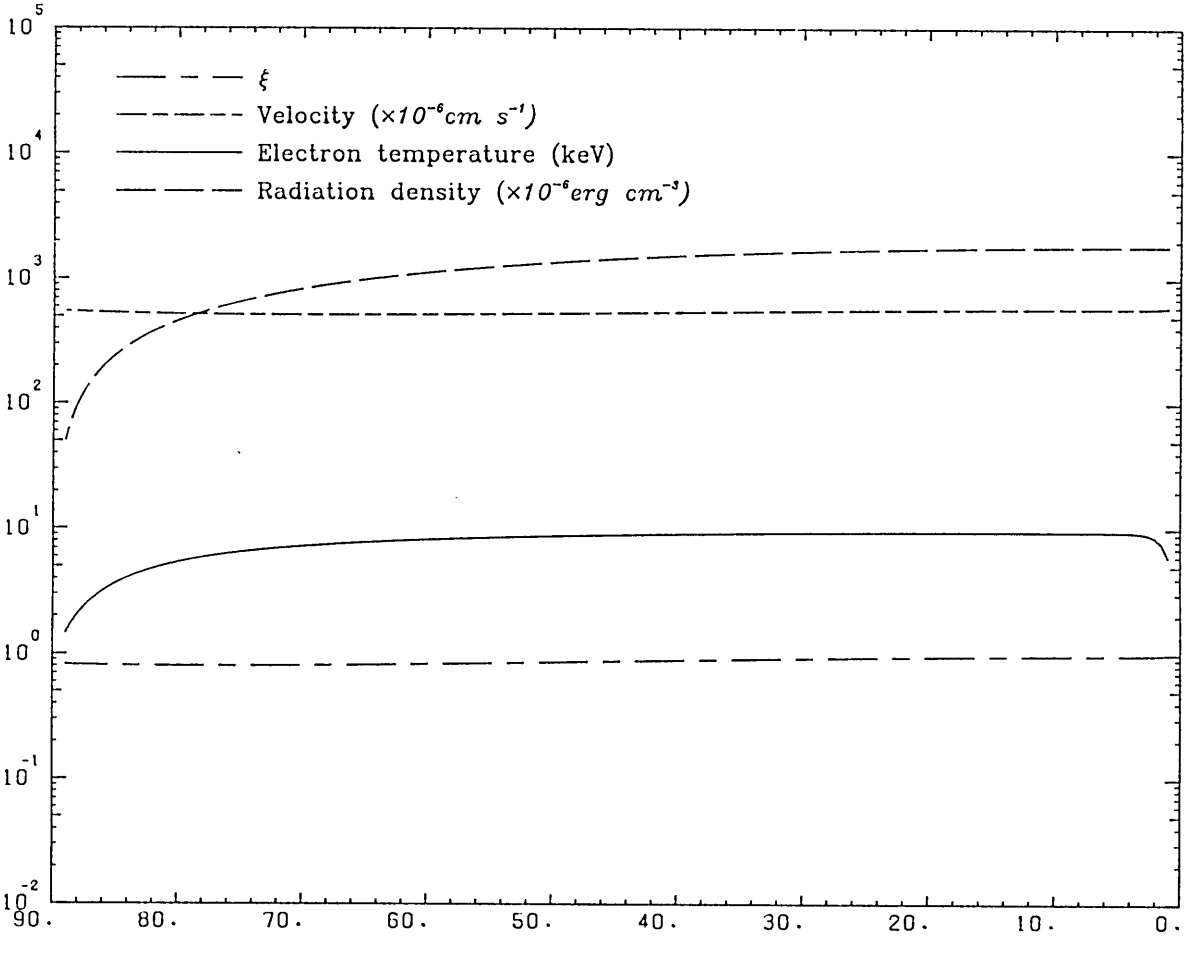

Fig 3.10. Plasma flow in the outer regions of the magnetosphere.

Parameters of this run are:-- $R_m=7.43\times10^8 cm$ $Depth=4.10\times10^7 cm$ $\alpha=1.0$
$L_x=3\times10^{38} erg\ s^{-1}$ ξ(at R_m)=0.5 T_e(at R_m)=6.0keV. T_R=10.0keV

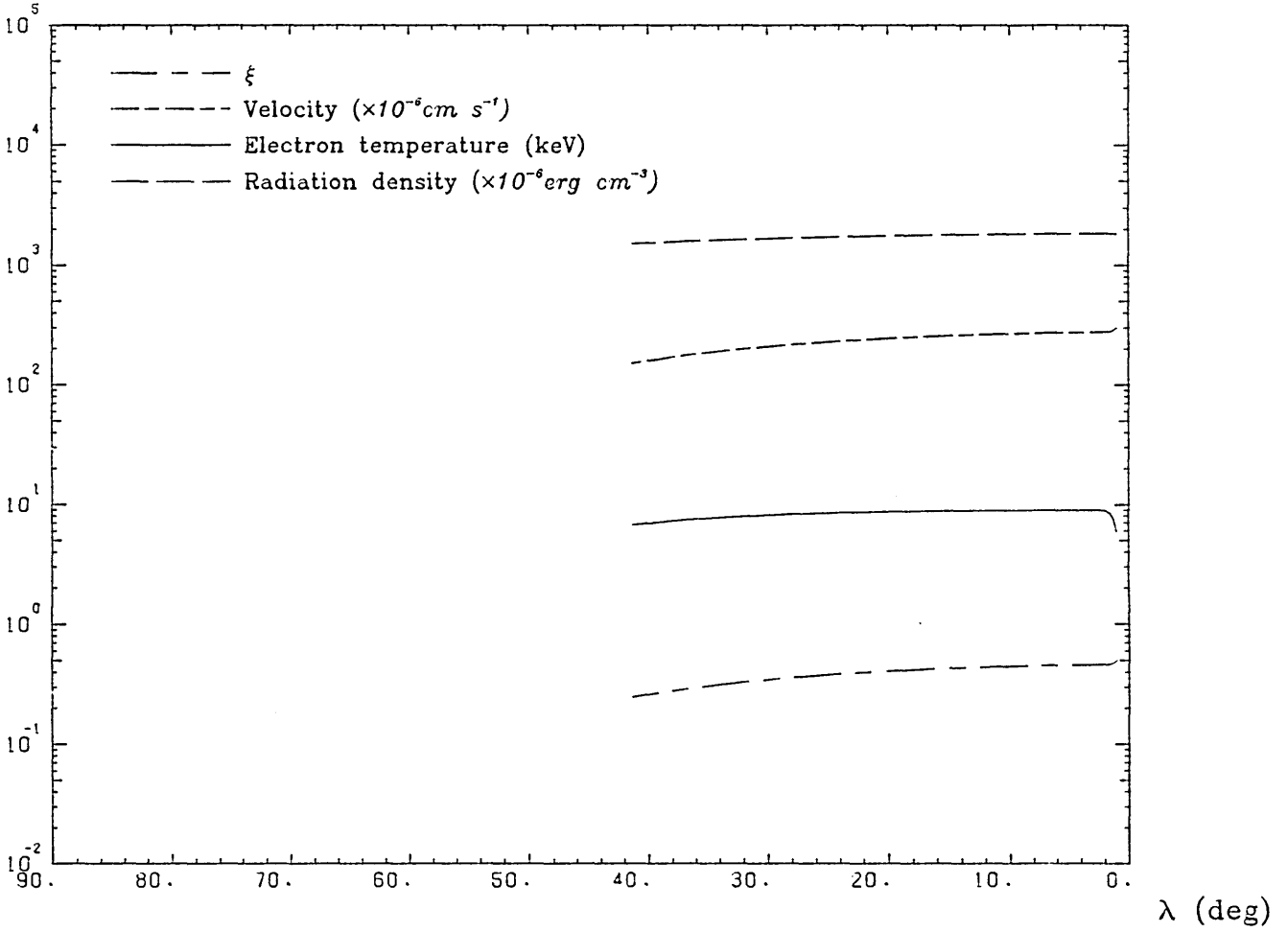

CHAPTER 4.

Radiation production and the slowing down of accretion flow in X-ray binaries.

§4.1 Characteristics of X-ray pulsars.

§4.1.1 Situation considered.

This chapter considers slowing down mechanisms and radiation production for binary X-ray pulsars with parameters similar to those observed. It also considers the possibility of super-Eddington luminosity (see §4.3). Typically, X-ray binaries have large duty cycles, X-ray luminosities in the range $L_x \sim 5 \times 10^{35} \rightarrow 10^{38} erg\, sec^{-1}$, with much of the X-ray output at energies $\sim 10keV$.

We will take as a typical case for the sake of argument a $1M_\odot$ neutron star having a luminosity of $L_x \sim 3 \times 10^{37} erg\, sec^{-1}$, producing X-rays of energy $\sim 10keV$. This is typical of higher luminosity X-ray pulsars such as Her X-1. For simplicity, general relativistic effects are ignored as they are in most papers that consider the mechanisms of X-ray binaries. The uncertainties in the various other parameters and X-ray production mechanisms are large, therefore, ignoring general relativistic effects does not have a great effect on the overall picture.

The exact radius of a $1M_\odot$ neutron star is unknown. *Arnet + Bowers 1977* consider the radii of neutron stars for various masses and equations of state. Their estimate of the radius of a $1M_\odot$ neutron star $r_\star$ varies between $0.86 \times 10^6 cm$ and $1.65 \times 10^6 cm$. In the model in the next chapter a radius of $1.5 \times 10^6 cm$ is assumed.

§4.1.2 Kinetic temperature.

If it is assumed that the accreted matter free falls to the surface of the neutron star each proton will have a kinetic energy $GMm_p/r_\star$. If this is assumed to be immediately given up to 1 photon the kinetic temperature is given by:-

$$T_K = \frac{GMm_p}{kr_\star} = 1.6 \times 10^{12} \left(\frac{M}{M_\odot}\right) \left(\frac{R}{10km}\right)^{-1} {}^\circ K$$

This gives a temperature where $kT \sim 100meV$ *Manchanda 1977.* It is therefore obvious that the kinetic energy of the protons must be released gradually. The kinetic energy of one proton cannot be transfered to a single photon.

§4.1.3 Black body temperature

If all the gravitational potential energy released is emitted as a black body covering the entire surface of the neutron star the temperature will be given by:-

$$T_{BB} = \left(\frac{L_x}{4\pi r_\star^2 \sigma}\right)^{1/4} = 1.23 \left(\frac{r_\star}{10km}\right)^{-1/2} keV$$

where $L_x = 3 \times 10^{37} erg\, sec^{-1}$, and σ is the Stefan-Boltzman constant. This is much smaller than the observed photon energies. If the black body radiation is assumed to be radiated from a fraction f of the neutron star surface the black body temperature would then be:-

$$T_{BB} = 1.23 \left(\frac{r_\star}{10km}\right)^{-1/2} f^{-1/4} keV$$

if $f = 0.01$ then $T_{BB} = 3.89keV$ which is still much less than the peak energy observed. This and the above section show that a more sophisticated approach to understanding the radiation production is needed.

§4.2 Geometry of the slowing down region.

§4.2.1 Discussion.

For a magnetic accreting neutron star matter is channeled to the surface of the neutron star by the magnetic field. The exact geometry of the slowing down region is unknown. Two cases are described below, an annulus and a funnel. The real case probably lies somewhere between these two, or is a far more complicated geometry. In most of the calculations presented in this thesis a funnel is assumed.

§4.2.2 Annulus.

The case of accretion down an annulus is argued for by *Basko + Sunyaev 1976.* If accretion takes place from an accretion disk matter may be frozen into the magnetic field of the neutron star at the magnetic equator. The depth to which the plasma penetrates into the dipole field is small compared to the Alvén radius. This plasma follows the magnetic field lines and when it reaches the neutron star surface it is in the shape of a thin annulus around the magnetic pole. The annulus may not be complete, the shape may be an arc of a circle rather than a circle. This is because the contours of constant magnetic pressure in the disk are not circles, and matter freezes into the magnetic field where the contour of constant magnetic pressure is remotest from the neutron star.

In the case of accretion from a stellar wind plasma may enter the magnetosphere predominantly near the magnetic equator. Again the depth to which the plasma penetrates is small compared to the Alvén radius and the above arguments may apply. See *Arons + Lea 1976* and chapters 2 and 3. Fig 4.1. is a schematic diagram of annulus geometry.

§4.2.3 Funnel.

This geometry is more likely to be formed in the case where accretion is from a stellar wind. When plasma entry into the magnetosphere is not confined to a small region about the magnetic equator, plasma may reach the surface down magnetic funnels at the poles of the neutron star. This is again argued by *Basko + Sunyaev 1976.* Even if the plasma enters predominantly near the equator of the magnetosphere, a funnel may still be formed depending on the manner in which the magnetosphere is formed. The magnetosphere is discussed in more detail in chapter 2. Fig 4.2. shows funnel geometry.

§4.3 Interaction of radiation with infalling plasma.

§4.3.1 The Eddington Luminosity.

This well known limiting luminosity arises from the pressure exerted on infalling matter by radiation. Here we assume that the accreting matter is in the form of fully ionized hydrogen. It is also assumed that electromagnetic forces keep the number density of protons equal to the number density of electrons.

As the luminosity increases the outward radiation flux increases. The outward radiation force per electron is proportional to the Thomson cross section multiplied by the radiative flux. Hence as the radiative flux increases the outward radiaton force per electron increases whereas the inward gravitational force per electron remains constant. Hence for spherically symmetric accretion the maximum luminosity L_{EDD} is given by:-

$$L_{EDD} = 4\pi \frac{c}{\kappa} GM \approx 1.25 \times 10^{38} \left(\frac{\kappa_T}{\kappa}\right) \left(\frac{M}{M_\odot}\right) erg\, sec^{-1}$$

where κ is the opacity, $\kappa_T = \sigma_T / m_p$ is the Thomson opacity.

The Eddington luminosity may be exceeded if $\kappa < \kappa_T$ which can occur in strong magnetic field; see §4.3.4. The Eddington luminosity may also be exceeded if the geometry is not spherically symmetric and the radiation does not need to pass through the infalling matter, as in the case described in chapter 5.

§4.3.2 Radiation outflow from "hot spot".

Assume matter is accreted down two magnetic funnels whose radii at the stellar surface are $a_f r_\star$. Here we also assume that the radiation is produced from the two polar caps each of area $\pi a_f^2 r_\star^2$. If all the radiation produced passes through the infalling matter the maximum luminosity per cap which we can expect is:-

$$L_x = L_{EDD} \frac{a_f^2}{4} \left(\frac{\kappa_T}{\kappa} \right)$$

This may easily be exceeded as all the radiation produced does not need to pass through the accreting plasma, and is an indication that for real luminosities the radiation cannot all pass through the accreting plasma. This may also be considered as a minimum luminosity for which we can expect the radiation to play a significant role in the slowing down of the accretion flow. This is because the maximum effect the radiation can have on the infalling plasma occurs if all the radiation passes through the infalling plasma. Therefore, if in this case the effects of radiation are insufficient to slow the plasma then in the real case where not all the radiation passes through the infalling plasma then the radiation is unlikely to dominate the slowing down process.

§4.3.3 Radiation pressure gradient.

Again assume accretion takes place down a funnel. If the funnel is optically very thick the radiation produced will be scattered a number of times before escaping from the funnel. Much of the radiation is likely to escape from the sides of the funnel, but some may diffuse upwards through the infalling matter. A distribution of photons travelling in all directions is therefore set up, which can be considered to be a photon gas. The pressure gradient of this photon gas exerts a slowing down force on the infalling material. This may form the principle slowing down mechanism in many higher luminosity X-ray pulsars.

§4.3.4 Radiation processes in a high magnetic field.

The dominant mechanism by which radiation is scattered in a plasma having densities similar to those in an accretion funnel is by the inverse Compton process. The relevant scattering cross section is the Thomson cross section. From observations of cylcotron lines in some X-ray pulsars we know that some of the neutron stars have high magnetic fields. In strong magnetic fields the scattering cross section is modified for the following reasons.

An electron in a magnetic field orbits the magnetic field with an angular frequency $\omega_B = \frac{eB}{m_e c}$. Due to quantum effects the electron may only have a value of energy perpendicular to the magnetic field of $n\hbar\omega_B$, where n is an integer. In a strong magnetic field $\hbar\omega_B$ may be greater than the thermal energy kT of the electrons, therefore most of the electrons are in the ground state where $n = 1$, hence quantum effects prevent the electron from taking up momentum perpendicular to the magnetic field.

Compton and Bremsstrahlung cross-sections in a high magnetic field have been studied by several authors. *Canuto et al 1971* calculated the Thomson cross sections in a high magnetic field. Their result for the Thomson cross section for an electron travelling at an angle $\theta \ll 1$ to a magnetic field when $\omega \ll \omega_B$ was:-

$$\sigma \sim \sigma_T \left(\frac{\omega^2}{\omega_B^2} + \sin^2 \theta \right)$$

where θ is the angle between the magnetic field and the direction considered. It was also found that the Compton cross-section shows a resonance at $\omega = \omega_B$.

Lieu 1983 calculated the value of the Bremsstrahlung cross-section in a high magnetic field. *Daugherty + Ventura 1978* made a detailed study of emission processes in a high magnetic field and produced a graph of σ/σ_T as a function of ω/ω_B.

The reduction in the value of the Compton cross-section in a high magnetic field when $\omega \ll \omega_B$ is important to the problem of super-Eddington accretion.

§4.3.5 Optical depth along and across an accretion funnel.

As the importance of the interaction of radiation with infalling matter depends on optical depth, here the optical depth along and across an accretion funnel are calculated. Assume $\dot{m}$ is the mass flow per unit time down one accretion funnel whose radius at the base is $a_f r_*$. The cross sectional area of the funnel at the base is $A_* = \pi a_f^2 r_*^2$, and at radius r is $A_*(r/r_*)^\alpha$. If the funnel is shaped by a dipole magnetic field $\alpha = 3$. Simple mass conservation gives $\rho v A = \dot{m}$ where ρ is the density and v the velocity. Let $v = \xi_1 v_{ff}$ where v_{ff} is the free fall velocity.

$$\rho(r) = \frac{\dot{m}}{\xi_1 v_{ff} A} = \frac{\dot{m}}{\xi_1 \sqrt{2GM}\pi a_f^2} \frac{r_*^{\alpha-2}}{r^{\alpha-1/2}}$$

$$r_f = a_f r_* (r/r_*)^{\alpha/2} \qquad \dot{m} = \frac{r_* L_x}{2GM}$$

$$\tau_\perp = 2 r_f \kappa \rho = \frac{2\kappa L_x}{\xi_1 (2GM)^{3/2}\pi a_f} \frac{r_*^{\alpha/2}}{r^{(\alpha-1)/2}}$$

At base of funnel where $r = r_*$

$$\tau_\perp = \frac{5.4\kappa}{\xi_1 a_f} \left(\frac{M}{M_\odot}\right)^{-3/2} \left(\frac{r_*}{15km}\right)^{1/2} \left(\frac{L_x}{3 \times 10^{37} erg\, sec^{-1}}\right)$$

For $\kappa = 0.38$, $a_f = 0.05$

$$\tau_\perp \sim \frac{41}{\xi_1}$$

Next calculate the optical length along the funnel.

$$\begin{aligned} \tau_\parallel &= \int_{r_*}^{\infty} \kappa \rho dr \\ &= \frac{\dot{m} r_*^{\alpha-2}}{\sqrt{2GM}\pi a_f^2} \int_{r_*}^{\infty} \frac{\kappa}{\xi_1} r^{(1/2-\alpha)} \end{aligned}$$

For simplicity, the variation in κ is ignored. Also take $\xi_1 = 1$. Assume $\alpha \neq 3/2$.

$$\tau_\parallel = \frac{\dot{m} r_*^{(\alpha-2)}}{\sqrt{2GM}\pi a_f^2} \left[\frac{r^{3/2-\alpha}}{3/2-\alpha}\right]_{r_*}^{\infty}$$

If $\alpha < 3/2$, $\tau_\parallel$ from this calculation is infinite. Again take $\alpha = 3$.

$$\tau_{||} = \frac{1.8\kappa}{a_f^2}\left(\frac{L_x}{3\times 10^{37} erg\, sec^{-1}}\right)\left(\frac{r_*}{1.5km}\right)^{1/2}\left(\frac{M}{M_\odot}\right)^{-3/2}$$

For $a_f = 0.05$, $\kappa \sim \kappa_T \sim 0.38$

$$\tau_{||} \approx 275$$

For the funnel to be optically thin along its length, the opacity would need to be reduced by ≈ 300 along the entire length of the funnel. This means that in the case of the higher luminosity sources the radiation cannot escape along the funnel. Hence the "pencil beam model" described in the next section is only appropriate for low luminosity sources.

§4.4 Some models of slowing down of accretion flow and radiation emission

Several authors have studied the processes by which accretion flow is stopped and the radiation emitted. The mechanism by which the flow is stopped depends on factors such as the luminosity, the geometry of the flow and the physics of the various slowing down mechanisms proposed.

One of the earliest studies of the processes was carried out by *Zel'dovich and Shakura 1969*. They assume a spherically symmetric geometry. They considered emission from a layer of plasma at the surface of the neutron star due to Bremsstrahlung and Compton emission. They also study slowing down due to coulomb collisions.

It is worth noting that in the spherically symmetric case, unless the luminosity is at least equal to the Eddington luminosity, the flow cannot be stopped by the interaction of radiation with the infalling matter alone. *Klein et al 1980* study super-Eddington spherically symmetric accretion, and solve the radiation hydrodynamic equations in this case.

For lower luminosity spherically symmetric cases and low luminosity non-spherically symmetric cases the radiation pressure may not be sufficient to stop the inflow. The plasma must therefore be stopped by other mechanisms. For cases where the magnetic field is low, the slowing down may take place via coulomb collisions. In a high magnetic field electrons cannot take up momentum perpendicular to the magnetic field due to quantum effects, hence the effects of coulomb collisions are drastically reduced. Proton-proton collisions are one

possible mechanism for slowing down of accretion flow. *Basko + Sunyaev 1975* consider the stopping of the infalling matter by nucleon-nucleon collisions. They calculate the stopping length from simple consideration of the cross-section for nucleon-nucleon scattering; and obtain a mean free path of $\sim 50 g\,cm^{-2}$. However, *Kirk + Galloway 1981* consider the Fokker-Planck equation for a proton gas and calculate the friction and diffusion coefficients for a gas of protons. They find that protons with an infall speed of c/4 can be stopped by $\sim 1 g\,cm^{-2}$. This is important for low luminosity sources and also shows that any kinetic energy remaining in higher luminosity sources as matter reaches the surface can quickly be dissipated.

Some authors consider the "pencil beam" model, which is one possible scenario for low luminosity sources where the neutron star has a high magnetic field, e.g. *Basko + Sunyaev 1975*. This is based on the modification of the Thomson opacity in a strong magnetic field. It assumes that as the opacity is greatly reduced along the magnetic field photons produced escape predominantly along the magnetic field in the form of a "pencil beam", see fig 4.3. This is probably reasonable for low luminosity cases, where the slowing down has occured by proton-proton collisions. As indicated by the calculation in §4.3.5 this situation is unlikely to occur for higher luminosity sources.

Another possibility is the "Fan Beam" model. This is likely to occur in higher luminosity sources. When the optical depth along the funnel is $\gg 1$ radiation cannot escape along the funnel. It therefore must escape from the sides of the funnel. If the radiation escapes from the sides close to the stellar surface it may form a "Fan Beam" of radiation, see fig 4.4. The model in chapter 5 indicates that the fan beam is a likely geometry for the radiation outflow.

Langer and Rappaport 1982 construct a model of accretion down a magnetic funnel applicable to sources of low enough luminosity such that the interaction of the radiation produced with the infalling matter can be ignored. They assume a collisionless shock forms in the accretion funnel above the surface of the neutron star and matter falls to the surface with $v \ll v_{ff}$. Hydrodynamic equations are solved taking an imposed shock as a boundary condition. Emission processes in a high magnetic field are taken into account.

An early investigation of acretion down a magnetic funnel where the flow is stopped by a radiation pressure gradient was carried out by *Davidson 1973.*

- See page 156

Two dimensional radiative transfer in the lower part of the accretion funnel is considered by *Wang + Frank 1981.* They consider accretion down a funnel. They define the problem as a two dimensional boundary value problem considering the equations on an 11×11 grid. They solved the resulting 121 simultaneous equations by a matrix inversion technique. They take into account the change in opacity in a magnetic field using an approximation for both $\sigma_{||}$ and $\sigma_{\perp}$ in a high magnetic field. The main slowing down mechanism in their model is radiation pressure gradient. They find the flow slows down abruptly above the surface.

Basko + Sunyaev 1976 investigate the radiation hydrodynamic equations with a view to finding the maximum luminosity of an accreting neutron star. They take the diffusion approximation for radiation transport. The geometry assumed is an annulus. They also consider radiation output from the sides of the annulus, i.e. they assume the radiation does not have to diffuse upwards through the infalling matter. They represent the diffusion from the sides as U/d where U is the average radiation density in the annulus and d is the thickness of the annulus.

§4.5 Optically thick limiting cases.

§4.5.1 Radiation output from the sides of an optically thick funnel.

If the opacity across a funnel is $\gg 1$, then it is a reasonable approximation to suppose that radiation output is approximated by a black body. Let the radiation pressure at radius r be $P(r)$, and assume it is approximately constant across the accretion funnel.

The energy emitted from the sides of the cylinder per unit area $= \sigma T^4$ where T is radiation temperature and σ is the Stefan-Boltzman constant. The energy emitted per unit height $= 2\pi r_f \sigma T^4$. The energy emitted per unit volume, D_{perp}

$$D_{perp} = \sigma T^4 \frac{2\pi r_f}{\pi r_f^2} = \frac{3c}{2}\sqrt{\frac{\pi}{A}} P_r$$

The radiation output from the sides of the accretion funnel D_{perp} may be expressed as KP_r where

$$K = \frac{3c}{2}\sqrt{\frac{\pi}{A}}$$

in the case of black body output.

§4.5.2 A soft limit for radiation output from an accretion funnel.

This is the case where gravitational potential energy released is converted locally into black body radiation. This is instead of the potential energy initially being converted into kinetic energy of the infalling matter and released as radiation at the bottom of the funnel. Basically, this case assumes that a rapid slowing down mechanism exists, so that as the potential energy is converted into kinetic energy it is immediately converted into radiation. This case is unlikely to occur, as shown in §4.5.3; but a soft limit for the radiation output is a worthwhile calculation.

If there is a mass flow $\dot{m}$ down one accretion funnel the gravitational potential energy released per unit height is $\dot{m}GM/r^2$. This is assumed to be converted into black body radiation emerging from the sides of the funnel whose radius at r is r_f. The black body output per unit length from a cylinder radius r_f is $2\pi r_f \sigma T^4$, where T is the radiation temperature. As $r_f = a_f r_\star \left(\frac{r}{r_\star}\right)^{\alpha/2}$, equating $\dot{m}GM/r^2$ to $2\pi r_f \sigma T^4$ gives:-

$$T(r) = \left(\frac{L_x r_\star^{\alpha/2}}{4\pi\sigma a_f r^{(4+\alpha)/2}}\right)^{1/4}$$

Therefore the radiation temperature at the surface of the star is:

$$T_{\star\, soft} = \left(\frac{L_x}{4\pi\sigma a_f r_\star^2}\right)^{1/4}$$

and where $\alpha = 3$, $T(r) = T_\star r^{-7/8}$. Also the radiation pressure at the surface is given by:-

$$P_{\star\, soft} = \frac{L_x}{3\pi c a_f r_\star^2}$$

For example, for a luminosity $L_x = 3 \times 10^{37} erg\, sec^{-1}$, where $a_f = 0.05$ then $T_{\star\, soft} = 1.17 \times 10^7\ ^\odot K \sim 1keV$; or if $a_f = 0.01$, $T_{\star\, soft} \sim 1.5keV$. This shows that even for the smallest likely value of a_f the radiation temperature in

this limit is very much less than that required to produce the observed X-ray spectra.

§4.5.3 Minimum pressure at the surface of the star. - Also see page 157.

This is a calculation of the minimum pressure required at the bottom of the accretion funnel if the accreting matter is to be brought to rest by a pressure gradient. To estimate the minimum pressure required equate:–

$$\int_{r_\star}^{\infty} \frac{dP}{dr}.dr = \int_{r_\star}^{\infty} \rho \frac{GM}{r^2} dr$$

let $\xi_1 = \frac{v(r)}{v_{ff}(r)}$, and as calculated in §4.3.5

$$\rho(r) = \frac{\dot{m} r_\star^{(\alpha-2)}}{\xi_1 \sqrt{2GM}\pi a_f^2 r^{(\alpha-1/2)}}$$

Therefore:-

$$P^\infty - P_{\star\, min} = \frac{\dot{m} r_\star^{(\alpha-2)} GM}{\sqrt{2GM}\pi a_f^2} \int_{r_\star}^{\infty} \frac{1}{\xi_1 r^{(\alpha-3/2)}}.dr$$

Take $\xi_1 = 1$ and let the pressure at infinity be zero. Taking the efficiency to be 100% this gives:-

$$\begin{aligned} P_{\star\, min} &= \frac{\dot{m}}{\pi a_f^2 r_\star^2} \sqrt{\frac{2GM}{r_\star}} \frac{1}{(2\alpha+1)} \\ &= \frac{L_x}{(2\alpha+1)\pi v_{ff\,\star} a_f^2 r_\star^2} \end{aligned}$$

Where $v_{ff\,\star} = \sqrt{\frac{2GM}{r_\star}}$ is the free fall velocity at the surface of the star.

If assume our typical case, $L_x = 3 \times 10^{37} erg\, sec^{-1}$, $\alpha = 3$ and $r_\star = 1.5 \times 10^6 cm$ then:-

$$P_{\star\, min} = \frac{4.57 \times 10^{13}}{a_f^2}$$

Next consider the radiation pressures and temperatures that this corresponds to for various values of a_f. If a spectrum corresponding to a black body at a single temperature is plotted in terms of counts per unit energy as a function of energy then the peak is at $E_{peak} = 1.5936 T_r$. This is due to Wein's law, see §4.5.3.

Table 4.1. Minimum pressure required to slow down accretion flow by a pressure gradient and corresponding radiation temperatures.

a_f	$P_{\star min}$	$T_r = \left(\frac{3P_r}{a_f}\right)^{1/4} keV$	$E_{peak} = 1.5936 T_r\, keV$
0.1	4.57×10^{15}	3.17	5.05
0.05	1.38×10^{16}	4.4	7.01
0.02	1.14×10^{17}	7.08	11.28
0.01	4.57×10^{17}	10.02	15.97

The peak energy output is of the correct order of magnitude, especially for $a_f < 0.05$. The pressure at the surface of the star is likely to be greater than $P_{\star min}$ because slowing down is not instantaneous, the velocity must be less than the free fall velocity for at least a short region. It is reasonable to expect that $P_\star \sim 1 \rightarrow$ a few $P_{\star min}$. Also, if the slowing down takes place close to the stellar surface, the change in cross-sectional area of the funnel can be ignored. In this case one would expect the minimum pressure to be approximately that corresponding to the calculation if $\alpha = 0$; in the case where $\alpha = 3$ this would be equal to seven times the minimum pressure calculated above.

Much of the radiation may be emitted in a region further up the accretion funnel where the radiation pressure is less than that near the stellar surface. If the radiation in this region is also in thermal equilibrium, i.e. it is black body radiation, the radiation temperature will be less than that near the stellar surface. Addition of radiation from this region may therefore shift the peak to a temperature softer than that corresponding to the surface temperature. Therefore the above calculation and arguments are not in conflict with observations, and appear to fit well with the types of source being considered.

If we compare the radiation pressure at the surface of the star calculated in §4.5.1 $P_{\star soft}$ to this minimum pressure calculated in this section we get the following ratio:-

$$\frac{P_{\star soft}}{P_{\star min}} = a_f \frac{(2\alpha + 1)}{3} \frac{v_{ff\star}}{c}$$

As $v_{ff\star}/c \sim 1/3$ and $a_f < 1$ this means this shows that the soft limit from §4.5.2 is unlikely to actually exist as the radiation pressure is not sufficient to stop the flow. The variable calculated $P_{\star min}$ is a useful parameter and in the

model in chapter 5 the radiation pressure is expressed in terms of $P_{\star min}$.

§4.6 Spectrum calculation from a series of black bodies.

4.6.1. The principle of the calculation.

Here the case of an accretion funnel emitting radiation from the sides in the form of a series of black bodies at temperature $T_r(r)$ at a given r is considered. A spectrum may be calculated by integrating this series of black body spectra to give a total output spectrum. This is the same principle as that used by *Lynden-Bell 1969* to calculate the characteristic spectrum of an accretion disk. This will also form a soft limit for the spectrum for a model of given radiation pressure as a function of r.

In order to compare the theoretical spectrum produced by this integration with observations of X-ray pulsars, it is necessary to express the calculated spectrum in a similar way to observed spectra. The commonest way of expressing these spectra is photons $cm^{-2}sec^{-1}keV^{-1}$ plotted against energy in keV. Both are usually plotted logarithmically. Photons cm^{-2} refers to photons received by the detector. The most logical way to express the calculated spectrum is therefore log(photons emitted $sec^{-1}keV^{-1}$) plotted against log(energy) in keV. It is not necessary to plot the number of photons emitted, a variable proportional to the number of photons emitted is sufficient.

The specific intensity of radiation emitted by a black body of temperature T is given by:-

$$I(\nu) = \frac{2h\nu^3}{c^2} \frac{1}{\left(e^{\frac{h\nu}{kT}} - 1\right)}$$

Where $I(\nu)$ is the amount of radiant energy per unit frequency, per solid angle crossing unit area in unit time; see standard texts on radiative transfer such as *Pomraning 1973*. The energy density per unit frequency is given by:-

$$\begin{aligned} E(\nu) &= \frac{1}{c} \int I d\Omega \\ &= \frac{2h\nu^3}{c^3} \frac{1}{\left(e^{\frac{h\nu}{kT}} - 1\right)} \times 4\pi \end{aligned}$$

Therefore the energy emitted from a radiating black body per unit frequency, per unit area, per unit time is:-

$$\frac{E(\nu)}{4c} = \frac{2\pi h\nu^3}{c^2}\frac{1}{\left(e^{\frac{h\nu}{kT}}-1\right)}$$

The number of photons emitted per unit frequency per unit area per unit time, $F(\nu)$ is given by:-

$$F(\nu) = \frac{2\pi\nu^2}{c^2}\frac{1}{\left(e^{\frac{h\nu}{kT}}-1\right)}$$

To convert this from number of photons per unit frequency to number of photons per unit energy simply divide the above by h. The number of photons emitted per unit area per unit energy per unit time of energy E is given by:-

$$F(E) = \frac{2\pi E^2}{h^3c^2}\frac{1}{\left(e^{\frac{E}{kT}}-1\right)}$$

Therefore, the total number of photons emitted per unit time per unit energy at energy E is:-

$$L(E) = \int_{r_\star}^{\infty} \frac{2\pi E^2}{h^3c^2}\frac{1}{\left(e^{\frac{E}{kT(r)}}-1\right)} 2\pi a_f r_\star \left(\frac{r}{r_\star}\right)^{\frac{\alpha}{2}} dr$$

As arbitrary units are acceptable, the number of photons emitted per unit energy per unit time at energy E is:-

$$N(E) = CE^2 \int_1^{\infty} \frac{{r_u}^{\alpha/2}}{\left(e^{\frac{E}{T(r_u)}}-1\right)} dr_u$$

Where $r_u = r/r_\star$ is the non-dimensional radius, and C is a constant. Therefore, if T is known for various values of r, this expression can be integrated numerically to produce a spectrum. Infinity may be taken as an appropriate value, for example a few stellar radii where the radiation pressure is very much less than that near the stellar surface.

§4.6.2 Method of calculation of the spectrum.

The values of $T(r)$ that are the result of a model to slow the accretion flow may not be evenly spaced. An integration scheme is therefore required that can integrate over unevenly spaced points. A suitable routine is the NAG routine D01GAF, which is third order accurate. This is used to integrate the formula given in the above section for a given set of values of $T(r)$ and r for various values of E thus producing a spectrum.

The values of E are chosen such that the log of the various values of E are evenly spaced as the spectrum is plotted logarithmically. Where E/T_r is large, e^{E/T_r} is extremely large and cannot be calculated. Therefore, any point where E/T_r is greater than 300 is not used in the integration for that given E. Such points cannot make a significant contribution to the level of radiation at that energy as $1/(e^x - 1)$ becomes extremely small as x becomes large.

It is sometimes worthwhile to plot a black body spectrum for a single temperature on the same graph as the calculated spectrum. The peak of the black body spectrum when expressed in photons per unit energy is calculated as follows. Output in photons per unit energy per unit time is proportional to $\frac{E^2}{(e^{E/T}-1)}$ The peak is given where $\frac{d}{dE}F(E) = 0$ If put $x = E/T$ then this is equivalent to finding the root of $(x-2)e^x + 2 = 0$. Using Newton's method the root of this equation is at $x = 1.593624$. Therefore the peak of the output in photons per unit energy per unit time for a black body at a single temperature T is at $E = 1.593624T$. This is the equivalent for a spectrum expressed in counts per unit energy to the usual black body peak at $E = 2.82T$ when the spectrum is expressed in terms of energy emitted per unit energy. The program used to calculate the spectrum from a series of black bodies is given in Appendix 2; this version uses the results of chapter 5 as the data.

As an example the spectrum for the soft limit case of §4.5.2 was calculated. In this case, as the temperature decreases very slowly with r, infinity was taken as $\sim 100r_\star$. The spectrum was calculated for several values of L_x and a_f. The spectra for $L_x = 3 \times 10^{37} erg\, sec^{-1}$ with various values of a_f is given in fig 4.5. The spectra for various values of L_x with $a_f = 0.02$ is given in fig 4.6. These again show that the this soft limit does not correspond with observed sources.

Figure 4.1. Annulus Geometry.

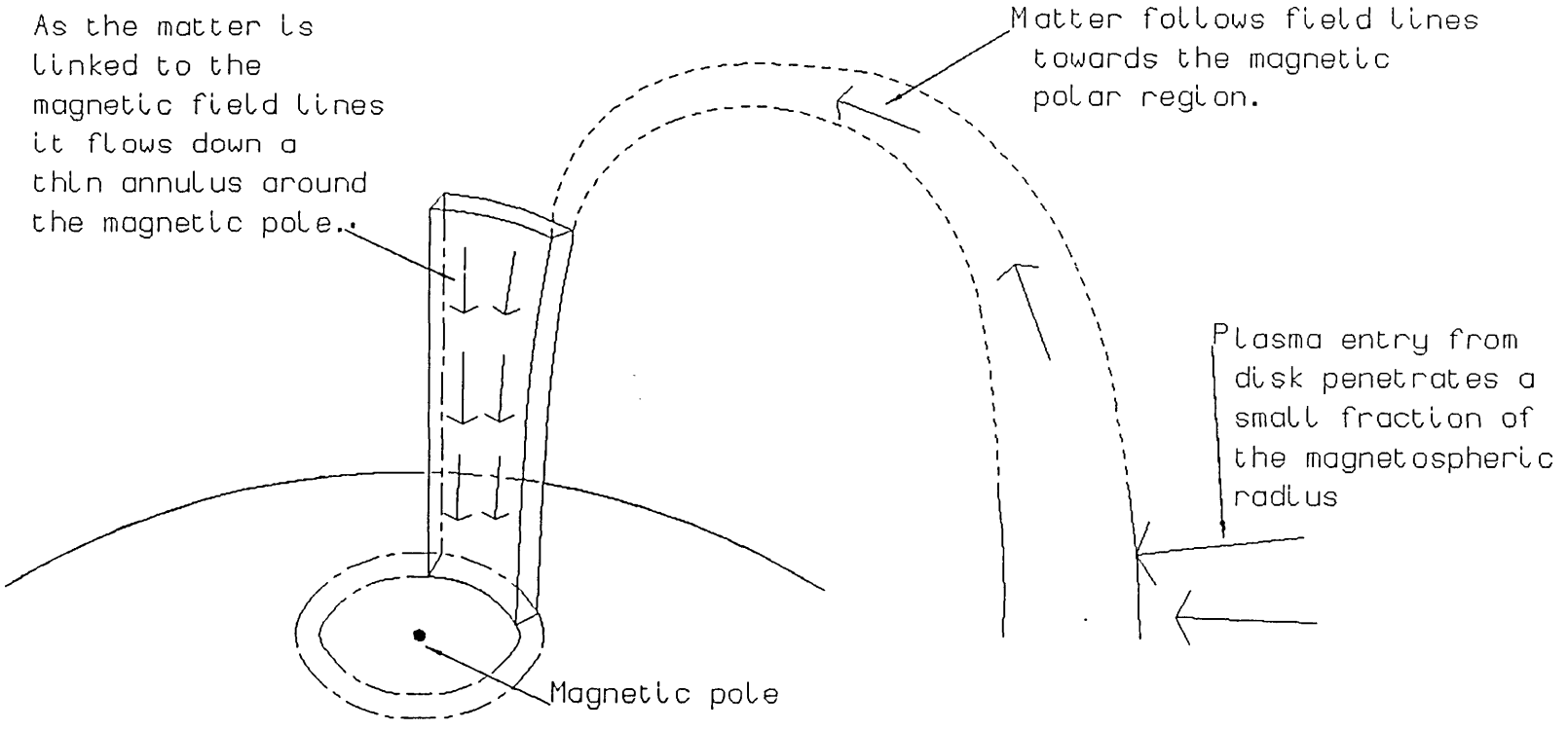

Figure 4.2. Funnel Geometry.

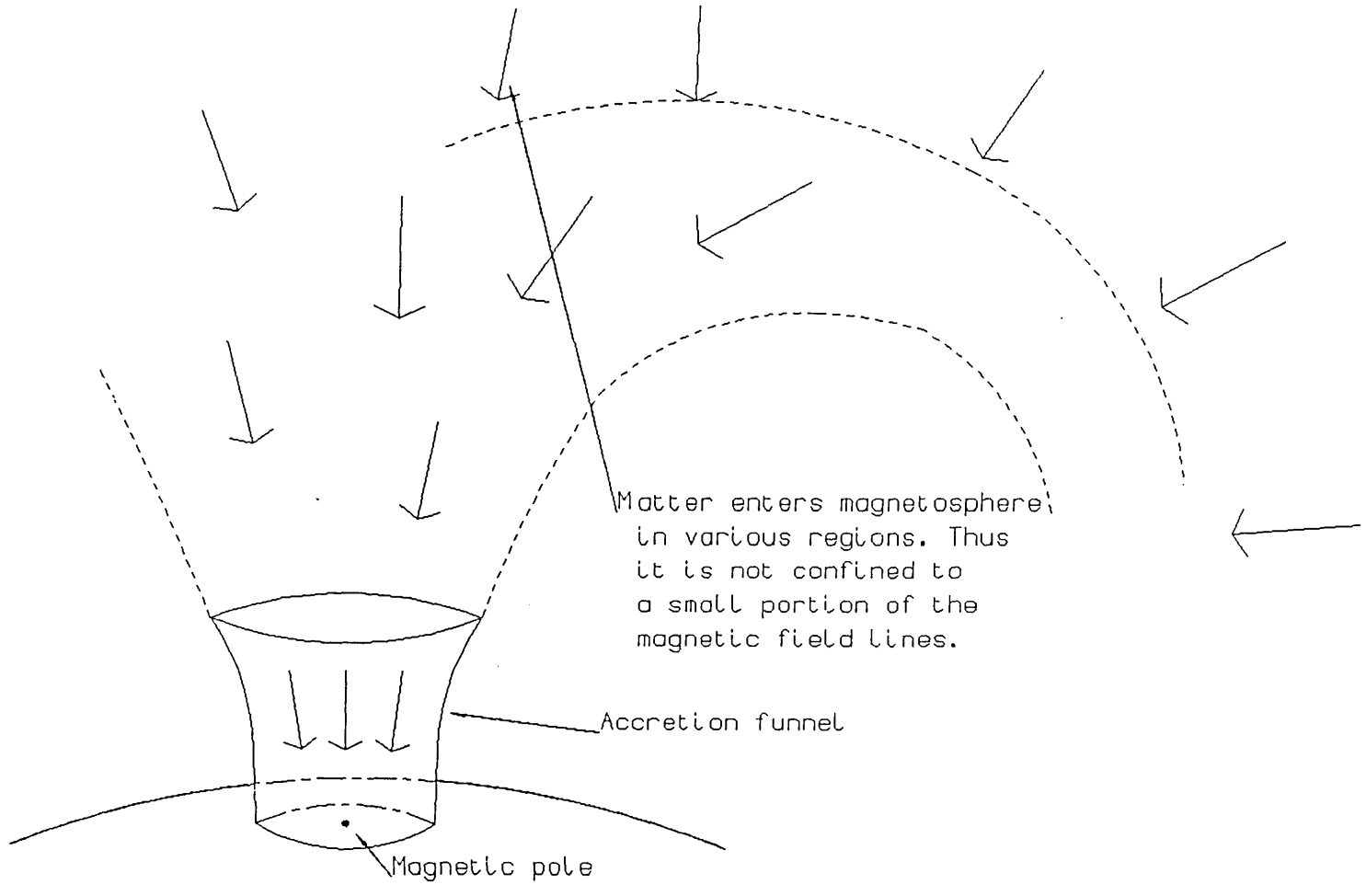

Figure 4.3. Pencil beam model.

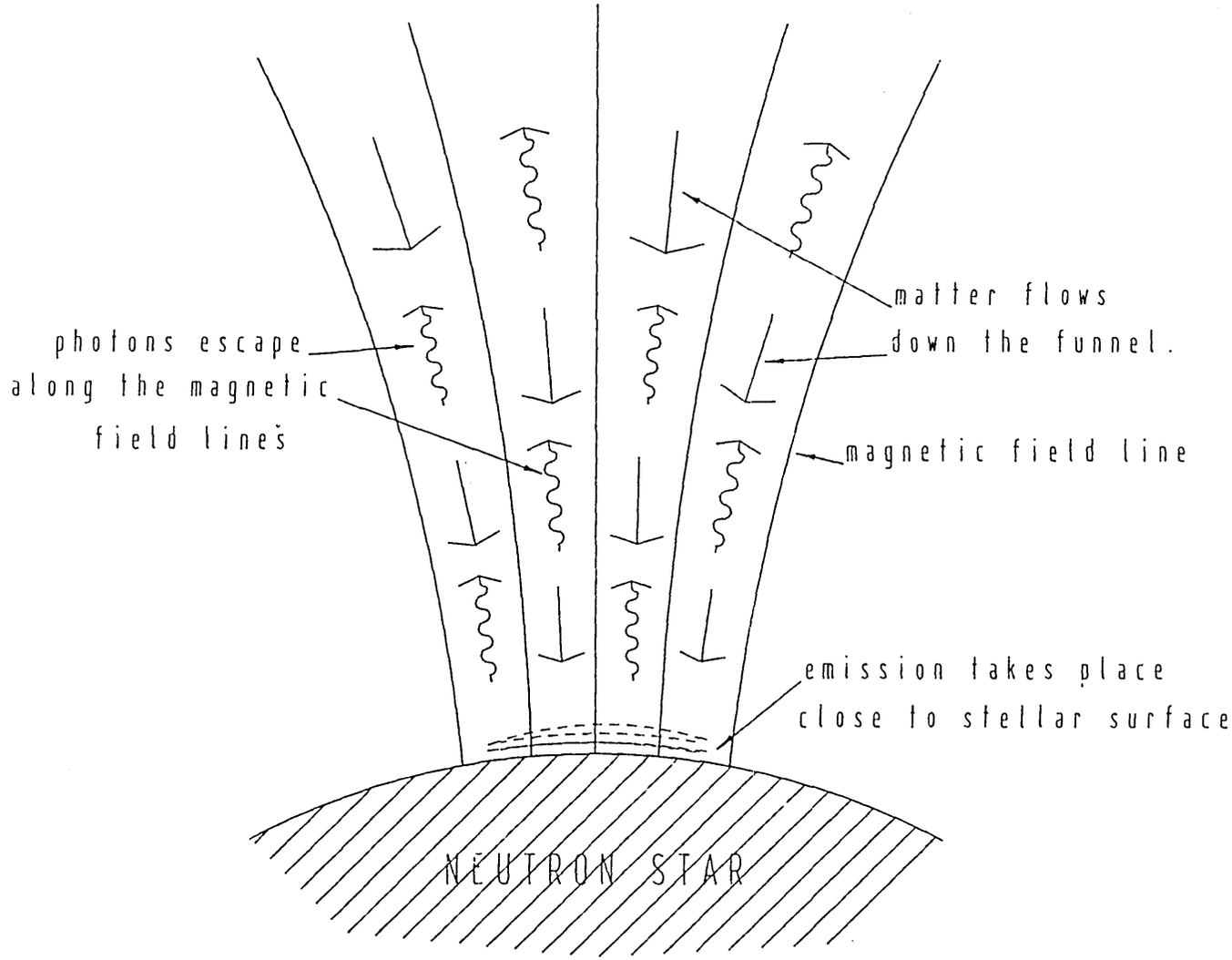

Figure 4.4. Fan beam model.

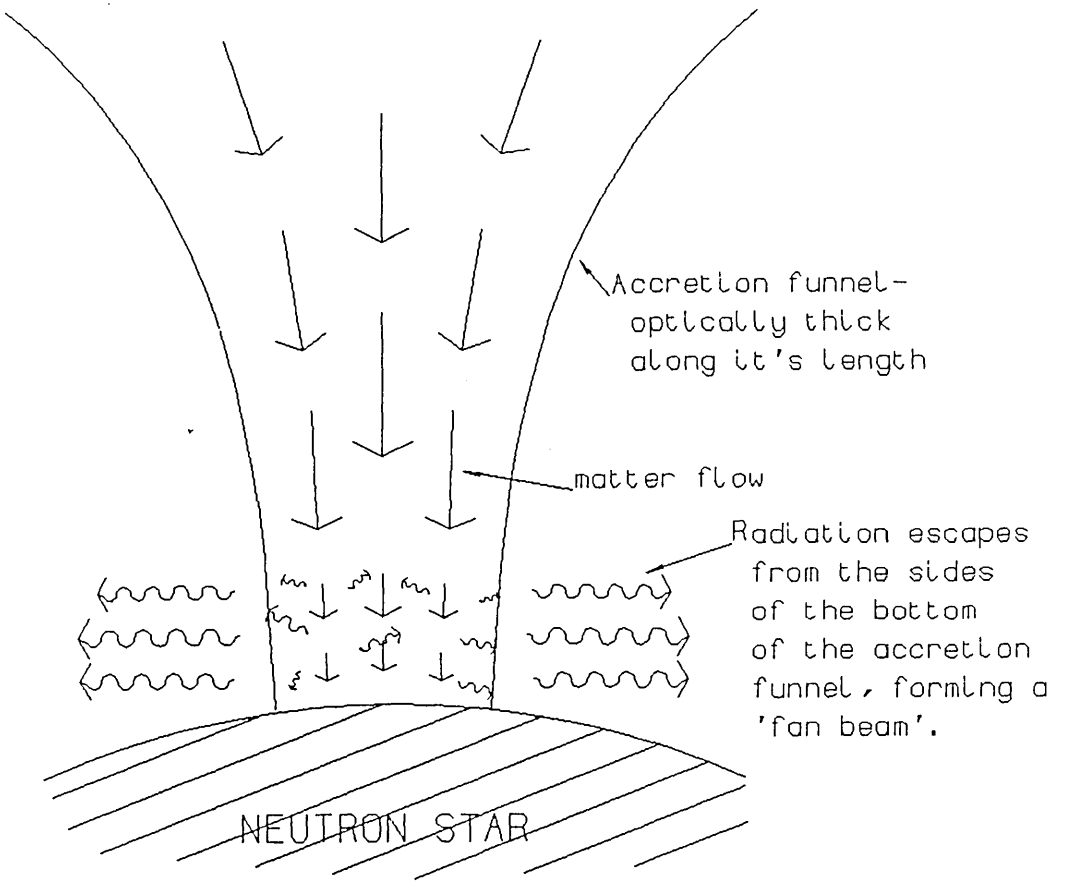

Fig 4.5. Soft limit spectra for various a_f with L_x constant

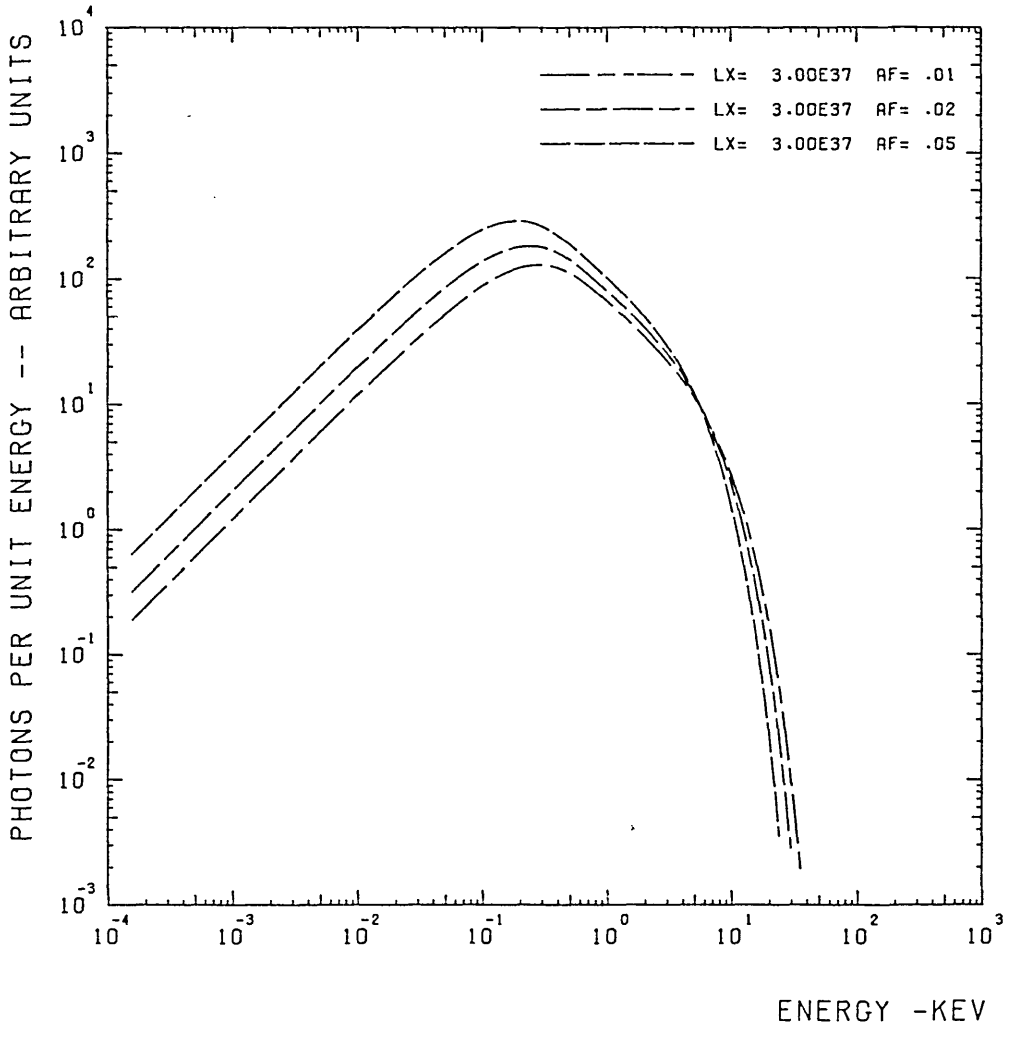

Fig 4.6. Soft limit spectra for various L_x with a_f constant

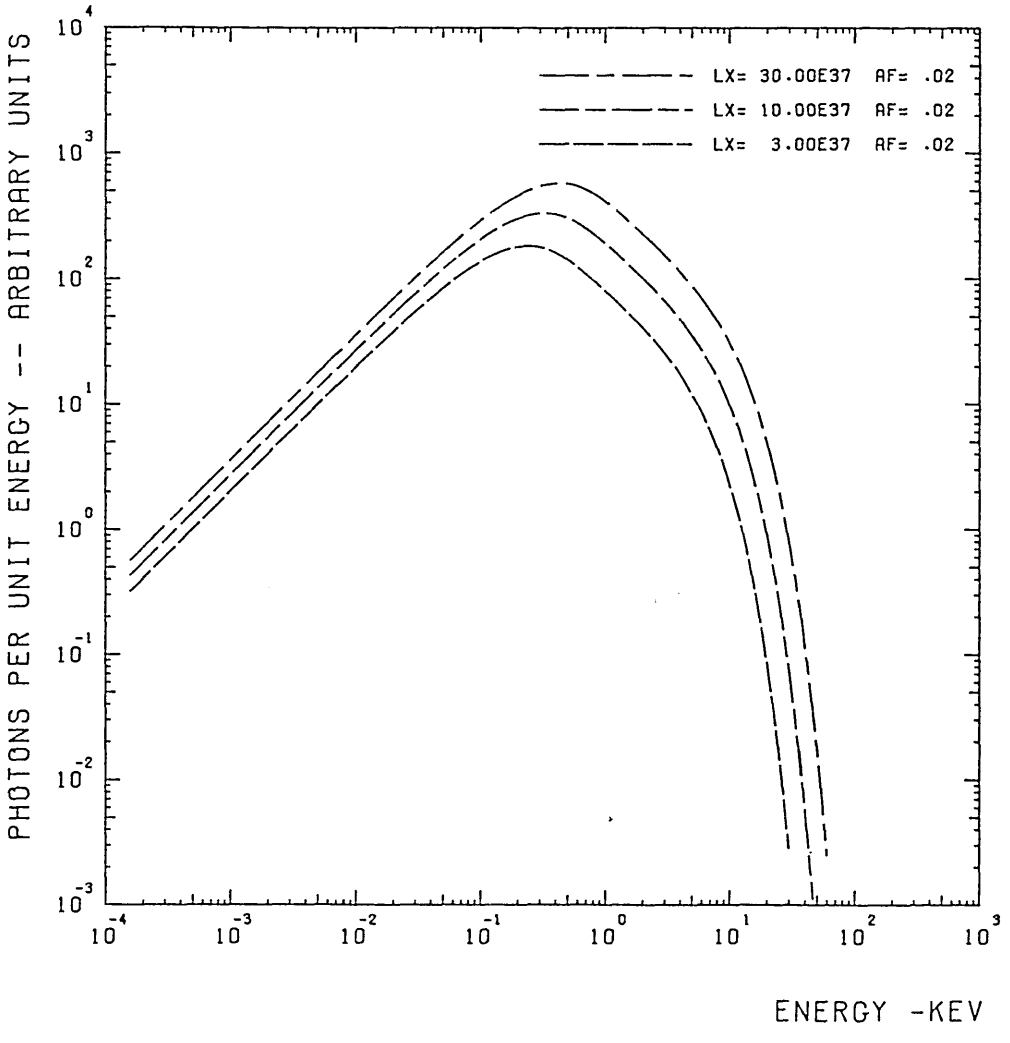

CHAPTER 5

A Model for an accreting neutron star near the bottom of an accretion funnel.

§5.1 The cases being considered in this chapter.

As indicated in chapter 1, binary X-ray sources are very varied and complicated objects. To produce a model that considers all the processes that are occuring would be extremely prohibitive. Any models that can be produced are necessarily an enormous simplification of the real case, yet it is important to model at least some of the more dominant phenomena of these objects. Some of the basic physics which constrains any possible model has been discussed in chapter 4. This chapter describes a model that shows some insight into accreting neutron stars with a luminosity of $0.06 \rightarrow 20 L_{EDD}$.

Funnel geometry is assumed in this chapter. Rotation is ignored for simplicity; although it is rotation that causes the pulsations of the X-ray pulsars, rotation may not have an important effect on the slowing down of the plasma flow and the production of radiation.

The purpose of this investigation is to understand more about accretion flow in the lower part of an accretion funnel. It is a study of how the falling matter is slowed down by a pressure gradient, the pressure gradient being a radiation pressure gradient. This case describes the situation in higher luminosity cases where the photons produced are scattered many times before escaping. This model takes into account photons escaping from the sides of the funnel, which is different from the case where all the radiation produced travels upwards through the infalling plasma. The range of luminosities this model seeks to understand vary between those of observed sources where $L_x \sim 10^{37} ergs\, sec^{-1}$ up to several times the Eddington luminosity.

When the velocity is a large fraction of the free fall velocity and the temperature is large enough for the pressure gradient to have an effect on the flow; order of magnitude calculations show that the radiation pressure must be very much greater than the gas pressure. Therefore, it must be a radiation pressure gradient that causes the matter to slow down if it is slowed down by a pressure gradient.

The aim is that the solution of the flow be self consistent. That is, the total radiation output from the sides of the funnel be approximately equal to the amount of gravitational potential energy available. This is one of the important properties of the model described here that is not considered in other high luminosity models.

The parameters of the accreting neutron star are as follows:-

$r_\star$	=	stellar radius ($= 1.5 \times 10^6 cm$)
M	=	Mass of star (usually $M_\odot$)
$r_{f\star}$	=	funnel radius at stellar surface
a_f	=	$r_{f\star}/r_\star = 0.01 \rightarrow 0.2$
$\dot{m}$	=	rate of accretion flow down 1 accretion funnel
ϵ	=	efficiency of production of radiation output
L_x	=	Luminosity $= 2\epsilon GM\dot{m}/r_\star$
$A_\star$	=	area of polar cap $= \pi {r_{f\star}}^2 = \pi {a_f}^2 {r_\star}^2$
A	=	Cross sectional area of funnel $= A_\star r/{r_\star}^\alpha$
T_e	=	Electron Temperature
T_p	=	Proton Temperature
T_r	=	Radiation Temperature
P_r	=	Radiation Pressure

In the slowing down region thermal equilibrium is assumed, i.e. $T_e = T_p = T_r$ and the radiation is assumed to be that of a black body, i.e. $P_r = a{T_r}^4/3$. Also $\alpha = 3$ as this corresponds to a the flowing plasma being confined by a dipole magnetic field. Thermal conductivity and viscosity are neglected. Fig 5.1 is a schematic diagram of the model described in this chapter; it is similar to the fan beam described in §4.4.

§5.2 Equations of the model and assumptions made.

The flow is assumed to be optically very thick, and the radiation is described by the diffusion approximation. This is reasonable considering the calculation in §4.3.5. The radiation is also assumed to be approximately black body at any given r. For simplicity, the variables are assumed to be constant across the funnel.

Mass Conservation.

$$\rho v A = -\dot{m}$$

It is worth noting that the direction of increasing r is taken to be the positive direction, therefore v is negative and $\dot{m}$ is positive.

Momentum Equation.

$$\rho v \frac{dv}{dr} = -\frac{dP_g}{dr} - \frac{dP_r}{dr} - \rho \frac{GM}{r^2}$$

Energy Equation.

$$\nabla . \left(\rho \frac{v^3}{2} + P_Q v P_g + 4 v P_r - D_{||} \frac{dP_r}{dr} - \rho v \frac{GM}{r} \right) = -K(r) P_r$$

This energy equation is derived by adding together the gas energy equation as given in §3.3. and the radiation diffusion equation given below:–

$$\nabla . \left(4 v P_r - D_{||} \frac{dP_r}{dr} \right) = -K(r) P(r) + \Lambda_R$$

where $K(r)P_r$ is the radiation output from the sides of the accretion funnel and Λ_R is the radiation emitted per unit volume of the hot gas. Combining these equations effectively loses one variable, the gas pressure.

The above equations assume that radiation transport may be described by the diffusion approximation. The diffusion coefficient is $D_{||} = c/\kappa\rho$ where κ is the scattering cross section σ divided by the mass of the proton m_p. The value of κ is variable. Also, $D_{||} = -cvA/(\dot{m}\kappa)$. Initially κ is taken as equal to the Thomson opacity as this will at least show how the equations behave and illustrate the physical processes occuring.

The term $-K(r)P_r$ represents the energy emitted from the sides of the funnel, as derived in §4.5.1. It repesents the energy output from the sides of

the funnel per unit volume of the plasma per unit time. $K(r)$ is taken as $K_{BB}(r)f_{BB}$ where K_{BB} is that which corresponds to the black body output. f_{BB} is introduced so that if required the output can be taken as less than the black body output. f_{BB} is less than or equal to one and is usually taken as equal to 1.

$P_Q = 5/2$ if there are no quantum effects. $P_Q = 3/2$ for electrons if 2 degrees of freedom are frozen out due to quantum effects in a high magnetic field, see for example *Langer + Rappaport 1982*. The average of these is 2, which forms a sensible value for P_Q. The dropping of some terms does mean that a value for P_Q is not actually needed.

Here we also note that the electron and proton temperatures are assumed to be equal in this region. Taking $T_r = T_e = T_p$ assumes that processes exsist that are fast enough to make this the case, or that gas pressure has a negligible effect. Justification for assuming $T_e = T_p$ is the same as that in §3.4. Justification for assuming $T_r = T_e$ is made by considering the time scale for thermal Bremsstrahlung given in §3.4.

$$\Delta t_B = 8.1 \times 10^{-14} \frac{T_e^{1/2}}{\rho}$$

By taking the formula for the density at a given r from §4.3.5. for the case where $r = r_\star$, the density near the bottom of the funnel is:–

$$\rho = \frac{L_x}{\xi_1 (2GM)^{3/2} \pi a_f^2 r_\star^{1/2}}$$

The value of ρ is taken for the case when $\xi = 1$, $a_f = 0.05$, $L_x = 3 \times 10^{37} erg\, sec^{-1}$, and other parameters are as in the model. This gives the minimum value for ρ at the bottom of the funnel which gives the maximum value for Δt_B. Also, a likely maximum value for the electron temperature is $T_e = 10keV$. This gives a value of $\Delta t_B \sim 10^{-6} sec$. In this time the free falling plasma will travel a distance equal to less than 1% of the stellar radius. As this is a maximum time scale and this is not the only emission process then assuming $T_e = T_r$ is a reasonable assumption. Even if the electron and proton temperatures are different from the radiation temperature, as the slowing down is dominated by the radiation pressure gradient, the difference in temperature will not have a great effect on the overall picture.

As the radiation diffuses upwards it may not be fully thermalised such that it represents a black body at a given r. This is because although the diffusion cross-section may be a reasonable representation of the diffusion, it does not assume that the photons have been fully thermalised within the diffusion length. If the plasma is not in thermal equilibrium the temperature at a given r may be greater than that corresponding to a black body for a given radiation energy density, while the actual value of the radiation energy density may be reasonably represented by the above equations. This means that the spectrum could be harder than that calculated, but this will not effect the dynamical slowing down process.

Also take $P_g = n_m kT/m_p$. For fully ionised hydrogen $n_m = 2$. For a gas containing 90% hydrogen and 10% helium where the helium is singly ionised $n_m = 1.9$. It is worth noting that it is possible to vary the effects of the gas pressure by varying n_m. If the gas temperature were twice the radiation temperature this could be approximately represented by doubling n_m. Varying n_m can also be used to test the significance of gas pressure on the slowing down of accretion flow.

The next approximation is to assume that gas pressure can be ignored except for its contribution to the slowing down due to $d\rho/dr$. The gas pressure gradient dP_g/dr may be large due to $d\rho/dr$ being large in the region where slowing down is very rapid, even though $P_g \ll P_r$

The equations described in this section are only appropriate in the region near the surface of the star where the flow is optically very thick. They describe the region where slowing down occurs and the flow is dominated by the radiation diffusing upwards through the infalling matter. They are not appropriate in regions further up the funnel that are remote from the region where the bulk of the slowing down and therefore radiation emission occurs. The regions further up the accretion funnel that are remote from the surface of the neutron star are discussed in chapter 6.

§5.3 Rearrangement of equations into dimensionless form.

In order to solve the equations in the previous section numerically using a standard method they need to be transformed into a suitable form. They are therefore expressed as a system of first order ordinary differential equations; see for example *Lambert 1976.* It is also convenient to express the equations in dimensionless variables.

First the density ρ is eliminated from the momentum and energy equations using the mass conservation equation. This gives one first order and one second order ordinary differential equation, in v and P_r as a function of r; as $P_g = P_g(P_r, v, r)$. The next stage is to choose suitable dimensionless variables in which to express the equations. The variables chosen are as follows:-

$$r_u = \frac{r}{r_\star}$$

$$f_{p0} = \frac{P_r}{P_{\star min}}$$

$$f_{p1} = \frac{df_{p0}}{dr_u}\left(= \frac{r_\star}{P_{\star min}}\frac{dP_r}{dr}\right)$$

$$\xi = \frac{v}{v_{ff\star}}\left(= v\sqrt{\frac{r_\star}{2GM}}\right)$$

Where $v_{ff\star}$ is the free fall velocity at the surface of the star, and

$$P_{\star min} = \frac{\dot{m}}{\pi a_f^2 r_\star^2}\sqrt{\frac{2GM}{r_\star}}\frac{1}{(2\alpha+1)}$$

as derived in §4.5.4. The variables, r_u ξ f_{p0} and f_{p1} are chosen as they are dimensionless, and rearrangement gives a system of 3 first order ordinary differential equations in the standard form:–

$$\frac{d\xi}{dr_u} = F_1(\xi, f_{p0}, f_{p1}, r_u)$$

$$\frac{df_{p0}}{dr_u} = F_2\,(= f_{p1})$$

$$\frac{df_{p1}}{dr_u} = F_3(\xi, f_{p0}, f_{p1}, r_u)$$

These equations are to be solved where r_u is decreasing. This is the direction where f_{p0} is increasing. In the case where equations have both a growth and a decay solution it is necessary to solve in the direction where a growth solution is

required. Otherwise, a small error will blow up and swamp the required decay solution.

The term originating from the $\rho\frac{n_m}{m_p}k\frac{dT}{dr}$ term of the gas pressure gradient is ignored, as is the $\rho\frac{kT}{m_p}\frac{1}{A}\frac{dA}{dr}$ term. The term originating from $n_m\frac{kT}{m_p}\frac{d\rho}{dr}$ is kept.

After rearrangement, the following equations are obtained:–

$$\frac{d\xi}{dr_u} = -\frac{\left(\frac{r_u^\alpha}{(2\alpha+1)}f_{p1} + \frac{1}{2\xi r_u^2}\right)}{\left(1 - \frac{Gasov2\, f_{p0}^1/4}{\xi^2}\right)}$$

$$\frac{df_{p0}}{dr_u} = f_{p1}$$

$$\begin{aligned}\frac{df_{p1}}{dr_u} = {} & \frac{CD2}{\xi r_u^\alpha} \times [\frac{K2S\, f_{p0}}{r_u^{\alpha/2}} - \left(4f_{p0} + \frac{2r_u^\alpha f_{p1}}{CD2}\right)\frac{\xi\alpha}{r_u} \\ & + \frac{1}{\left(1 - \frac{Gasov2\, f_{p0}^{1/4}}{\xi^2}\right)} \times [\left(4f_{p0}f_{p1} + \frac{r_u^\alpha}{CD2}f_{p1}f_{p1}\right)\frac{r_u^\alpha}{(2\alpha+1)} \\ & + \left(-\left(3 - 4\frac{Gasov2\, f_{p0}^{1/4}}{\xi^2}\right)\xi + \frac{r_u^{(\alpha-2)}}{2\xi\, CD2}\right)f_{p1} + \frac{2f_{p0}}{\xi r_u^2} \\ & + \frac{(2\alpha+1)}{2r_u^{\alpha+2}}\frac{Gasov2\, f_{p0}^{1/4}}{\xi^2}]]\end{aligned}$$

Where:–

$$Gasov2 = \frac{n_m k_B}{m_p}\left(\frac{3P_{\star min}}{a}\right)^{1/4}\frac{r_\star}{2GM}$$

$$CD2 = \frac{\kappa\dot{m}}{c\pi a_f^2 r_\star}$$

$$K2S = f_{BB}\frac{3c}{2a_f}\sqrt{\frac{r_\star}{2GM}}$$

If κ and f_{BB} are constant these three parameters are all constant for any set of parameters of the accreting neutron star, i.e. for any given run of the model they are constant. These constants are also dimensionless, therefore the above set of differential equations are in the form of 3 first order ordinary differential equations in dimensionless form.

The term $(1 - Gasov2\, f_{p0}^{1/4}/\xi^2)$ represents the effects of gas pressure. This term is ≈ 1 except where $\xi \ll 1$; which occurs in the region where much of the slowing down has already taken place. This term may then have a significant effect on the slowing down of the plasma.

The term $CD2$ represents $\frac{1}{D_{\|}}$, multiplied by certain parameters to make it dimensionless. $K2S$ represents perpendicular output, again in a dimensionless form.

§5.4 Boundary conditions and expectations of a solution.

It is expected that the bulk of the slowing down of plasma inflow and emission of radiation occurs within less than 1 stellar radius of the neutron star. The equations are integrated in the direction of decreasing r as this is the direction for which a growth solution is required. Hence the starting value for r_u is somewhere between $(1 + \delta)$ where $\delta \ll 1$ and 2. At the starting value of r the velocity is taken to equal the free fall velocity, i.e. it is assumed that negligible slowing down has already taken place. Therefore, $\xi = 1/\sqrt{r_u}$, at the starting point. Also start with $f_{p0} \ll 1$, as the radiation pressure will decay as it diffuses upwards through the infalling gas. The integration must be started at a value of r where $f_{p0} \ll 1$ as we require a solution that is valid up to the point where the physics within the funnel is dominated by physical processes other than diffusion of radiation up through the infalling matter. Also, $f_{p1} < 0$ as the radiation pressure is decreasing with increasing r. The magnitude of f_{p1} must be much greater than the magnitude of f_{p0} as the radiation pressure must change by several orders of magnitude over a stellar radius. The plasma is assumed to be confined by a dipole field, giving $\alpha = 3$. The equations are expressed in the program for the special case where $\alpha = 3$ as this assumption simplifies the functions in the equations which need to be calculated on every step of the numerical scheme.

One requirement of a solution is that when $r_u = 1$, $\xi \ll 1$; i.e. the slowing down has taken place. It is necessary to vary the starting value of r in order that the flow comes to rest at the surface of the neutron star. It is also expected that as the slowing down has taken place due to a radiation pressure gradient then the radiation pressure at the surface should be consistent with the required minimum pressure at the stellar surface; i.e. expect $f_{p0} = 1 \rightarrow N$ where $N \sim 10$.

One of the most important requirements of the model is that it should be self-consistent. The total radiation output from the sides of the funnel must be equal to, or nearly equal to the total energy available. This can be expressed as follows:–

$$\int_{r_\star}^{\infty} K(r)\, A\, P(r) dr = \epsilon \frac{GM\dot{m}}{r_\star}$$

Where the efficiency, $\epsilon \leq 1$. When this is converted into dimensionless form using the same variables as for the differential equations, the following expression is obtained:–

$$\int_{1}^{\infty} K2S \frac{r_u^{1.5} f_{p0}}{3.5} dr_u = \epsilon$$

Here, α has been taken as 3. This again needs to be integrated numerically. The starting point of the scheme used to solve the differential equations replaces infinity, as $f_{p0} \ll 1$ at this point, and the output from the sides of the funnel in the region is what is relevant to this model. Therefore, the above is replaced by:–

$$\int_{1}^{r_{u0}} K2S \frac{r_u^{1.5} f_{p0}}{3.5} dr_u = \epsilon$$

Where r_{u0} is the starting value of r_u.

§5.5 Method of solution.

The equations are in the form of a system of 3 first order ordinary differential equations in dimensionless variables. Therefore, a standard numerical method can be used. As one of the functions is rather lengthy, a numerical method that does not require a large number of function evaluations per step is required. First it is assumed that there are no serious stability problems as a growth solution is expected. These considerations point to an Adam's method; Adam's method is described in *Lambert 1976* or any standard text on methods for the computational solution of ordinary differential equations.

In the region where slowing down takes place rapidly; the step length of the scheme may need to be smaller than further up the funnel, hence a routine whose step length can be varied is required. Also, output is required at various values of r. This is in order to see the solution, to calculate the efficiency, and later to calculate a soft limit for the spectrum by the method described in §4.6. A variable order variable step Adams method was chosen. The NAG routine D02QAF was chosen, as this is a variable order variable step Adams method with extensive interrupt facilities, including the facility to output from the routine every integration step.

In order to see if the equations could be solved using the chosen numerical method, and whether this approach gives sensible results a simpler Adams method routine was tried. The NAG routine D02CBF is an Adams method routine which is very simple to use. It has a facility for intermediate output, the next output point being specified. In this test calculation the distance to the next output point was reduced if the fractional change in any variable since the previous output point was greater than a specified amount.

In both the test calculation and the later calculation the values of the variables at a large number of values of r and various other parameters were written out. Various other calculated variables were also written out to give some indication of what is happening and what terms dominate. The variables as a function of r are also witten to a file for use in later programs: to plot graphs and calculate the spectrum.

A solution of the radiation hydrodynamic equations using D02CBF was obtained. The results of these calculations indicated that a self consistent solution of the equations could be obtained, with the efficiency $\epsilon < 1$. Frequently,

the routine would fail between output points in the region where slowing down takes place very rapidly, indicating that the use of a routine with more extensive interrupt facilities is essential.

As an initial investigation indicated that the method of solution was reasonable, the routine D02QAF was used. Initially, as in the case for using D02CBF the routine was set to output if the fractional change was greater than a given amount; and exiting every step if ξ became less than a given value. After trying several criteria it was found that the most reasonable way to choose values to print out was to exit from the routine every step throughout and start printing values every few steps; and when slowing down had begun to take place rapidly the values were printed every step.

For the following reasons, the flow does not come to a halt at exactly $r_u = 1$ in any given run of the program to solve the equations. The equations are solved in the negative r direction because that is the direction in which a growth solution is required. It is assumed that the radiation must be liberated near the bottom of the funnel and diffuses upwards. The radiation pressure, radiation pressure gradient and velocity at any given r are dependent on what is going on at both smaller and larger r. An initial value problem as described here only follows the equations in one direction, only the properties in the direction from which the solution has been integrated are considered. For this reason it is necessary to keep restarting the integration until the conditions required by the model are satisfied. This is necessary because the conditions at the starting point of the integration are not actually known. The effective boundary conditions of the model are not actually the initial values, therefore the initial values have to be adjusted to produce the required boundary conditions.

As the end of the run cannot simply be taken as $r_u = 1$, it is necessary to select criteria for stopping the integration process during any single run of the model. These criteria must be carefully chosen so that the run does not fail before the run ends, and also the run does not end before it has progressed as far as is useful. The program was written so that the run ended for one of the following reasons. If $f_{p0} < 0$, i.e if the radiation pressure becomes negative; this is mainly a safeguard criteria in case the solution is going badly wrong. If $f_{p1} > 0$, i.e. if the radiation pressure starts to decrease as get nearer the stellar surface. If $\left(1 - Gasov2\, f_{p0}^{1/4}/\xi^2\right) < \delta$ where δ is a small number $\ll 1$ that can

be varied to produce an adjustable choice of when to end the run. If ξ is less than another small amount the run is ended, this is another adjustable criteria for ending the run. Also, if the step length became less than a given amount the run was ended, this formed a third adjustable criteria for ending the run.

When using Adam's method the routine tended to choose a very small step length in the region where $v \ll v_{ff}$ and $f_{p0} > 1$. It was necessary to set the minimum step size to an extremely small amount. The function F_3 was also very much less than some of the terms in the expression for F_3; i.e. the various terms in the expression for F_3 almost cancelled one another out. This is an indication that the equations are stiff in this region, and a special routine for stiff systems of ordinary differential equations is required.

Gear's method for stiff systems of ordinary differential equations was therefore tried. The NAG routine D02QBF is an implementation of Gear's method. Gear's method requires the calculation of the components of the Jacobian of the funcions of the system of differential equations. For a system of ordinary differential equations:–

$$\mathbf{y}' = \mathbf{F}(r, \mathbf{y})$$

the Jacobian is

$$|\frac{\delta \mathbf{F}}{\delta \mathbf{y}}|$$

Gear's method is described in *Gear 1971.* Stiff systems in general are described in texts such as *Lambert 1976* and Jacobians in general are described in various mathematical texts such as *Boas 1966.*

It was found that the components of the Jacobian could be expressed analytically without any difficulty. The expressions for the components of the Jacobian are given in Appendix 3.

It was found that before $v \ll v_{ff}$, i.e. above the region where there had been significant slowing down Gear's method did not work. Therefore, the program was started using Adam's method and when certain criteria had been met Gear's method was used. This did involve resetting the various parameters that are peculiar to each routine, or are used differently by each routine. Effectively, this means a new initial value problem is started with the values for r, ξ, f_{p0} and f_{p1} from Adam's method as starting values for Gear's method. The program used to solve the equations is given in Appendix 4.

§5.6 Calculation of the spectrum.

For any run of the model values of T_r for various values of r were written to a file. These were used to perform a soft limit spectrum calculation by the method described in §4.6.

At the starting point of the model the radiation pressure was very much less than that at the surface of the star. The radiation output above this point is ignored as far as the model for the radiation output from near the surface of the star is concerned. The spectrum associated with the part of the funnel between the starting point of the model and the surface of the star is calculated. Therefore, the integration of the function described in §4.6.1 is carried out between the surface of the star and the starting point of the model; i.e.

$$N(E) = CE^2 \int_1^{r_{u0}} \frac{r_u^{\alpha/2}}{\left(e^{\frac{E}{T(r_u)}} - 1\right)} dr_u$$

where r_{u0} is the starting point of the model.

The model writes the output data to the file with r decreasing. Therefore these values need to be reversed before the calculation can proceed.

In the region where $v \ll v_{ff}$ the step length chosen in the model was very small; therefore some of the points written to the file are very close together in r. It was found that if two points were too close together the NAG routine would fail. It is therefore necessary to eliminate some points so that there is a minimum distance between points used in the integration of the spectrum. The program used to calculate the spectrum is given in Appendix 2.

The calculated spectrum was plotted on a graph. On the same graph a black body spectrum for a temperature equal to that at the stellar surface was also plotted, normalised to the calculated spectrum at the peak of the black body spectrum.

§5.7 Results of calculations.

Computations were carried out for a wide range of L_x and a_f. Solutions to the system of differential equations could be found for $L_x \sim 0.05 \rightarrow 20 L_{EDD}$. These solutions were self consistent with an efficiency of $0.9 \rightarrow 1.0$ throughout this range of luminosity. Fig 5.2 shows the radiation temperature at the bottom of the funnel for varying $\dot{m}$ for three different values of a_f. These curves assume that the flow slows down within a distance very much less than the radius of the star. It also shows the peak energy output for various runs of the model, for values for $\dot{m}$ and a_f corresponding to those for which the curves are plotted. Detailed results for some sets of parameters are shown in figs 5.3 to 5.11. Figs 5.3 to 5.6 are all for a luminosity of approximately $3 \times 10^{37} erg\, sec^{-1}$ with different radii at the bottom of the funnel. Comparing figs 5.5, 5.7, and 5.8 shows how the results vary with luminosity when the radius of the funnel remains constant. Figs 5.9, 5.10 and 5.11 show 3 cases with a large funnel radius where the luminosity exceeds the Eddington luminosity. Table 5.1. overleaf shows the energy at which the radiation output spectrum peaks for various combinations of L_x and a_f for which the model was run and a self consistent solution was found. The mass flow $\dot{m}$ is in grams per second and the peak energy is in keV. The stars on the table represent mass flows for given a_f that are too small for the model to be self consistent.

See overleaf for table 5.1.

Table 5.1. Energy at which the radiation output spectrum peaks for various values of a_f and L_x.

$\dot{m}$ a_f	.01	.02	.05	.10	.20
2×10^{16}	9.8	$\star$	$\star$	$\star$	$\star$
5×10^{16}	15.1	9.1	$\star$	$\star$	$\star$
1×10^{17}	19.5	12.6	6.5	$\star$	$\star$
2×10^{17}	24.8	16.5	9.1	5.2	$\star$
5×10^{17}			13.1		
1×10^{18}		22.3	16.5		
2×10^{18}			20.0	13.8	
5×10^{18}			26.3		
1×10^{19}			30.9		
2×10^{19}			37.1		18.2

For all the runs of the model f_{p0} at the surface of the star was within a few percent of 7. This is the minimum value for which slowing down due to a radiation pressure gradient can take place, if the slowing down takes place in a short region where the change in cross-sectional area of the funnel can be ignored. Even for very high luminosity runs of the model where there was an extended region with $v \ll v_{ff}$ and $f_{p0} \sim 7$, the value of f_{p0} did not increase much above 8.

As can be seen from the graphs, the slowing down and emission takes place within a short distance equal to a few percent or less of the stellar radius. The slowing down takes place quite abruptly, more abruptly as the luminosity increases. It can also be seen from the graphs that for any given a_f as the luminosity increases the length of the region where $v \ll v_f f$ increases. In some papers, the region where the velocity is much less than the free fall velocity is called the sinking zone. These plots indicate that as the luminosity increases the length of the sinking zone increases.

When using Gear's method the use of the expressions for the components of the Jacobians did not make any difference to the results. The results were the same whether the program used its own internal approximation to the Jacobian

or the expression for the Jacobian given in Appendix 3. It also made very little difference to the amount of computer time the program took to run.

For lower luminosity sources the efficiency became greater than 1. This is because the limiting case of this model cannot describe lower luminosity sources. This is discussed in detail in §5.8.

If $(1 - Gasov2\, f_{p0}^{1/4}/\xi^2)$ becomes less than zero the equations cease to be sensible; therefore the run was ended if $(1 - Gasov2\, f_{p0}^{1/4}/\xi^2)$ became less than zero. The run most commonly ended when $(1 - Gasov2\, f_{p0}^{1/4}/\xi^2)$ became less than zero, or the step length became very small.

The spectral calculations are a soft limit continuum emission spectra for this model. For lower luminosity sources the spectral peak is much wider than the peak of a single black body. This is because black body spectra from regions at various temperatures are added together.

As the luminosity increases the calculated spectrum tends to that of a black body. Where $L_x \sim 10 L_{EDD}$ the spectrum is almost identical to that of a black body. This is because an extended sinking zone has formed in which the radiation temperature is approximately constant, from which most of the emission of radiation takes place.

§5.8 Conclusions and discussion.

The model shows that a solution to the radiation hydrodynamic equations can be found where matter is slowed down by a radiation pressure gradient. The model is able to give solutions over a wide range of luminosities, from 5% of the Eddington luminosity up to 20 times the Eddington luminosity. The results were self-consistent over this wide range of luminosities.

At the end of the run v is not equal to zero, but is very much less than the free fall velocity. The remainder of the slowing down may occur due to collisions with the stellar surface. The fraction of the origonal kinetic energy not converted into radiation by the end of the run is small enough that it does not effect the overall picture.

For all runs with $\dot{m}$ greater than a certain value, ϵ was equal to or slightly less than 1. For low luminosity ϵ became greater than 1. This indicates that there is a minimum luminosity for which the model is valid. A calculation of the minimum luminosity for which the model is valid may be based on the

minimum pressure required to slow down the flow, and an approximation to the scale length over which the radiation pressure changes. For the minimum luminosity it is assumed there is no extended sinking zone.

Two terms dominate the energy equation before slowing down has taken place. If these are equated to one another the following equation results:–

$$\frac{d^2 f_{p0}}{dr_u^2} = -\frac{3\,CD2}{r_u^\alpha}\frac{df_{p0}}{dr_u}$$

Assume for the minimum luminosity this equation reasonably describes the behaviour of f_{p0}. Also ignore the variation in cross sectional area of the funnel, as the scale length of change of radiation pressure is very much smaller than the stellar radius. As slowing down takes place over a length very much less than the stellar radius assume that at the stellar surface $f_{p0\star} = 7$. Therefore, f_{p0} can be approximately described by:–

$$f_{p0} = 7e^{-3\,CD2\,(r_u - 1)}$$

For self consistency, the efficiency must be equal to 1 therefore:–

$$\int_1^\infty \frac{K2S\, f_{p0}}{3.5} dr_u = 1$$

substituting for f_{p0} and integrating gives:–

$$\frac{2\,K2S}{3\,CD2} = 1$$

putting in the values for CD2 and K2S gives:–

$$\begin{aligned}\dot{m}_{min} &= \frac{\pi c^2 a_f r_\star}{\kappa}\sqrt{\frac{r_\star}{2GM}} \\ &= 1.59 \times 10^{18} a_f\end{aligned}$$

when $r_\star = 1.5 \times 10^6 cm$, $M = 1M_\odot$, and $\kappa = \kappa_T$. If $a_f = 0.05$, which is our most studied case, then $\dot{m}_{min} \sim 8 \times 10^{16} g\,sec^{-1}$. This gives a luminosity of $L_x = 7 \times 10^{36} erg\,sec^{-1} \sim 6\% L_{EDD}$. This is consistent with finding $\epsilon > 1$ when $\dot{m} = 6 \times 10^{16} g\,sec^{-1}$. It is worth noting that this is very much greater than the minimum luminosity for which we can expect the radiation to have an influence on the slowing down of accretion flow as expressed in §4.3.2, which is $0.06\% L_{EDD}$.

Another consideration of self-consistency is what has happened to the few percent of the energy that has not been emitted as radiation. The remaining kinetic energy is approximately ξ of the original energy available. The radiative energy carried down by the flowing plasma is approximately $\xi f_{p0}/7$ which is approximately ξ. Adding these to the efficiency does not quite make 1. This may be explained by our dropping some of the terms in the energy equation.

For runs of the model with luminosity similar to those of observed sources, it is worthwhile to compare the calculated spectra to the observed spectra. The calculated spectra are not as flat as those of the observed sources such as Her X-1, they cannot fully explain spectra such as those described in *Manchanda 1977*. This is because in the model the funnel is assumed to radiate like a black body throughout the emission region, which as discussed in §5.2. may not occur. The fact that many observed spectra resemble that of Bremsstrahlung emission indicates that the black body limit spectra calculated here are a poor approximation to the real case.

This model cannot fully explain the spectra of real sources and does not consider the details of any emission processes. It does illustrate how accretion flow may be slowed down by a radiation pressure gradient for a very wide range of accretion rates. It also gives radiation temperatures at the base of the accretion funnel that correspond to those of observed sources, indicating that the general picture resulting from this model is likely to be correct. It is also possible that a more realistic spectrum may be obtained by considering emission due to processes occuring further up in the funnel. If emission from higher up the accretion funnel is added to that from the base of the funnel it is possible that a more realistic spectrum may be produced.

The fact that runs of the model whose luminosities greatly exceed the Eddington luminosity does not necessarily mean that such sources actually occur in nature. There is some evidence that the Eddington luminosity may be exceeded, for example there is some evidence that SMC X-1 exceeds the Eddington luminosity. There are no observed sources that exceed the Eddington luminosity by a factor of 20.

Extremely high luminosity sources may not occur for a variety of reasons. Even though the matter may be able travel from the top of the funnel to reach the base of the funnel in such high luminosity cases, it may not be able to reach

the top of the funnel without being blown away by the large amount of radiation present. The radiation pressure in the outer regions of the magnetosphere may prevent the accretion taking place. It is unlikely that such a high accretion rate could occur from a stellar wind, see §2.4. Even for disk accretion there are limits to how much mass may be transferred. If accretion takes place from a disk it is likely that the matter may flow along field lines such that it occupies a small cross-section as it reaches the stellar surface, as shown by the annulus geometry discussed in §4.4.2. The higher luminosity runs of the model have a funnel with quite a large cross-sectional area.

It is worth considering other physical phenomena occuring near the bottom of the funnel which may limit the luminosity. The maximum luminosity may be limited by the maximum temperature for which e^+ e^- pair production is not significant. If the radiation temperature is greater than a certain value, the tail of the energy spectrum of the photons become of high eneough energy for e^+ e^- pair production to become significant. For electrons, $m_e c^2 \approx 500 keV$ which is very much more than the radiation temperatures at the bottom of the funnel for any runs of the model. The actual radiation temperature may be greater than those in this model as the radiation may not be fully thermalised.

For high luminosity models,the radiation pressure may become too high for the matter to be confined by the magnetic field. Assume the matter is confined by a magnetic field at the surface of the star of $5 \times 10^{12} gauss$. At the surface assume the radiation pressure is $7P_{\star min}$. Therefore:–

$$\frac{B^2}{8\pi} > 7P_{\star min}$$

Substituting for $P_{\star min}$ gives:–

$$\dot{m} < \frac{B^2}{8} a_f^2 r_\star^2 \sqrt{\frac{r_\star}{2GM}}$$

Substituting our usual values for the parameters gives:–

$$\dot{m} < 5.28 \times 10^{26} a_f^2 g\, sec^{-1}$$

For the example where $L_x \sim 20 L_{EDD}$ $\dot{m} = 2 \times 10^{19} g\, sec^{-1}$ This indicates that the luminosity is not greatly limited by the ability of the magnetic field to confine the radiating plasma near the bottom of the accretion funnel.

The model does indicate that in principle the Eddington luminosity may be greatly exceeded when accretion takes place down an accretion funnel. The luminosity is likely to be limited by the ability of matter to get transferred to the top of the accretion funnel rather than the ability to get to the surface from the top of the funnel. Chapter 2 indicates some of the difficulties arising in transferring large amounts of matter to the neutron star. Even if the large amounts of matter could be transferred to the neutron star to produce highly super-Eddington accretion, X-ray sources may not be produced. In the case where mass transfer rates are very high there must be a lot of matter in the vicinity of the neutron star. This matter will reprocess the X-rays emitted and the source is more likely to be seen in the ultra-violet or optical part of the spectrum.

It is worth mentioning that *Basko + Sunyaev 1976* attempted to calculate a limiting luminosity for accreting neutron stars. The model described in this chapter allows the Eddington luminosity to be exceeded to a far larger extent than was achieved in their paper. This is because they approximated the radiation output from the sides by assuming diffusion took place over a diffusion length equal to 1/2 of the thickness of the geometry they were considering. Considering black body output from the sides of an optically thick region, as taken by this model is equivalent to assuming a diffusion length equal to the mean free path of a photon. For this reason the output from the sides assumed by Basko and Sunyaev was a too small by a factor of approximately the optical length across the emitting region divided by two. Therefore, their approximation was reasonable if the optical length across the emitting region $\leq n$ where $n \sim 1 \rightarrow 10$.

In the case where $a_f = 0.05$ and $L_x \sim 3 \times 10^{37}$ the peak of the radiation output is at $\sim 9keV$. This is similar to that of observed sources of this luminosity. It is also consistent with many authors who calculate the radius of the funnel to be between 0.05 and 0.07 times the stellar radius. Therefore, the general picture of this model is consistent with observations and theoretical considerations of the magnetosphere.

§5.9 Suggestions for improvements and further work.

The model described here has assumed the geometry of the accreting region near the surface of the star is that of an accretion funnel. As there is a high likelihood that other geometries for accretion exist, it would be worth modifying the model to consider other geometries, for example that of an arc or annulus as described by *Basko + Sunyaev 1976.*

The model has assumed that the diffusion length corresponds to that due to the Thomson cross section. In a high magnetic field the Thomson cross section is quite a poor approximation, therefore it would be worthwhile to consider the effect of more realistic scattering cross sections on the accretion pattern. This could be done by simply varying the value of $CD2$ or κ.

The calculated spectra were a poor approximation to spectra observed. Yet the principle of adding spectra at various points in a radiation source is a useful one, and could be extended to more realistic spectral calculations. More detailed radiative transfer treatments and detailed radiative processes could be considered, and spectra calculated both for this type of source and for other types of sources.

Figure 5.1. Model of accretion flow and radiation production near the bottom of an accretion funnel.

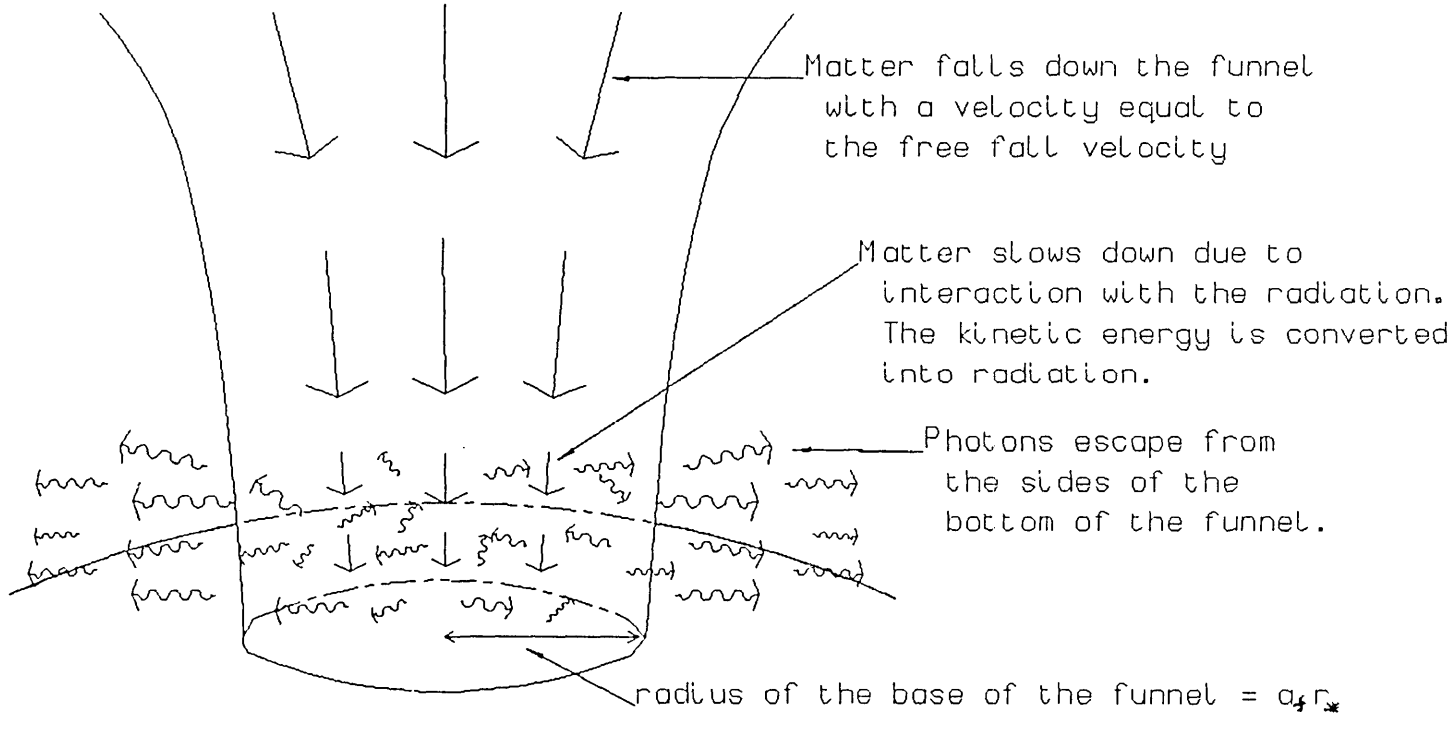

Fig 5.2. Graph of calculated temperature at the bottom of the funnel, and the energy where the radiation output peaks from some runs of the model

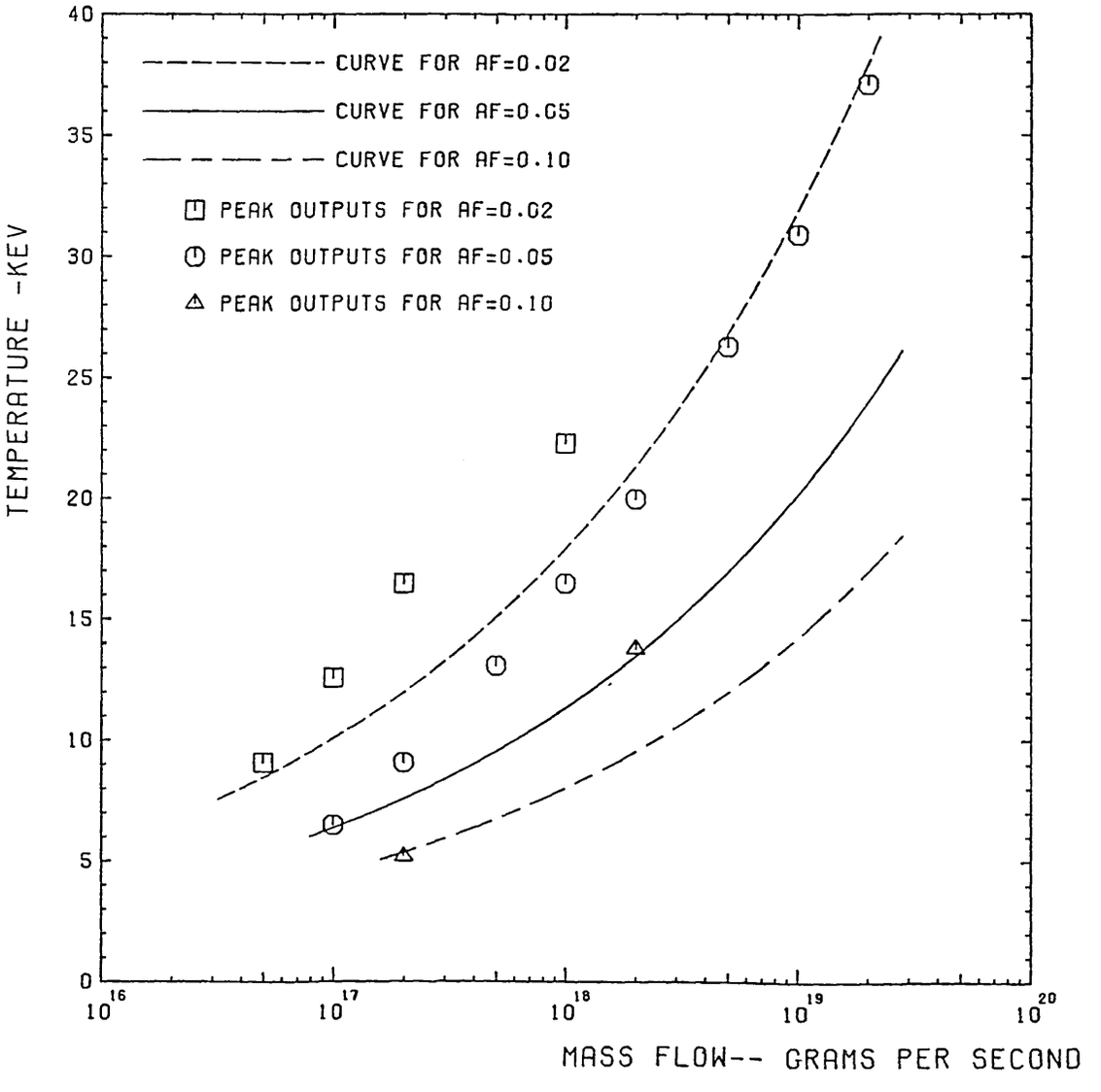

Fig 5.3. Plot of ξ, fp0, fp1 and spectrum at the bottom of the funnel

Parameters of this run-- MASSFC=2×10^{17} $g\ s^{-1}$ $L_x=3.2\times10^{37}$ $erg\ s^{-1}$ a_t=0.01

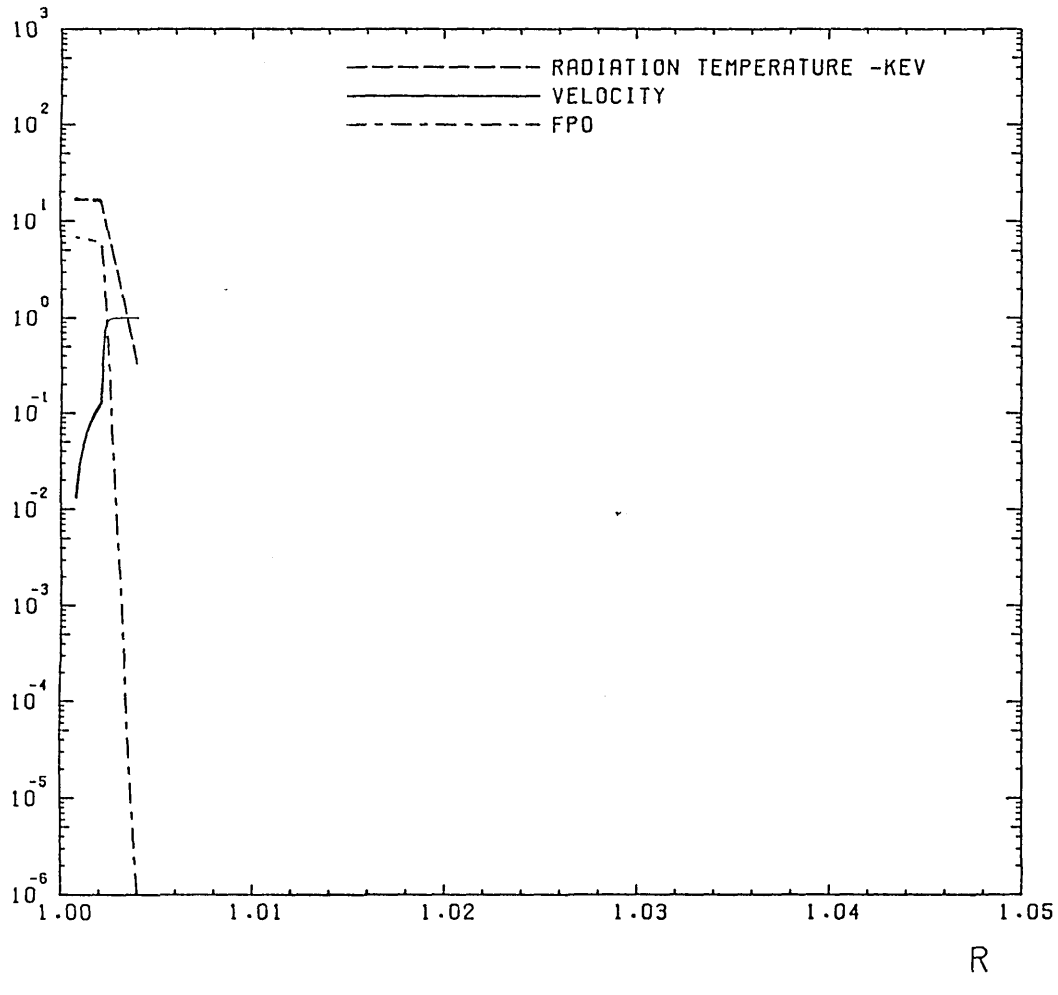

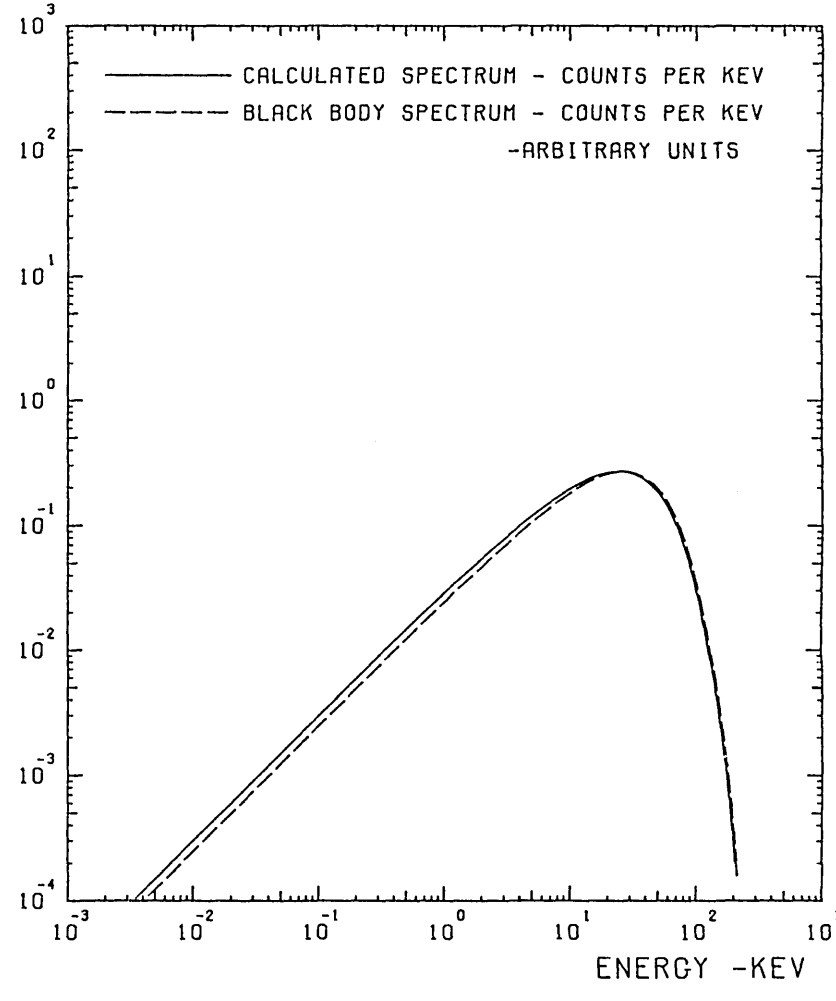

Fig 5.4. Plot of ξ, fp0, fp1 and spectrum at the bottom of the funnel

Parameters of this run-- MASSFC=2×10^{17} $g\ s^{-1}$ $L_x=3.2\times10^{37}$ $erg\ s^{-1}$ $a_f=0.02$

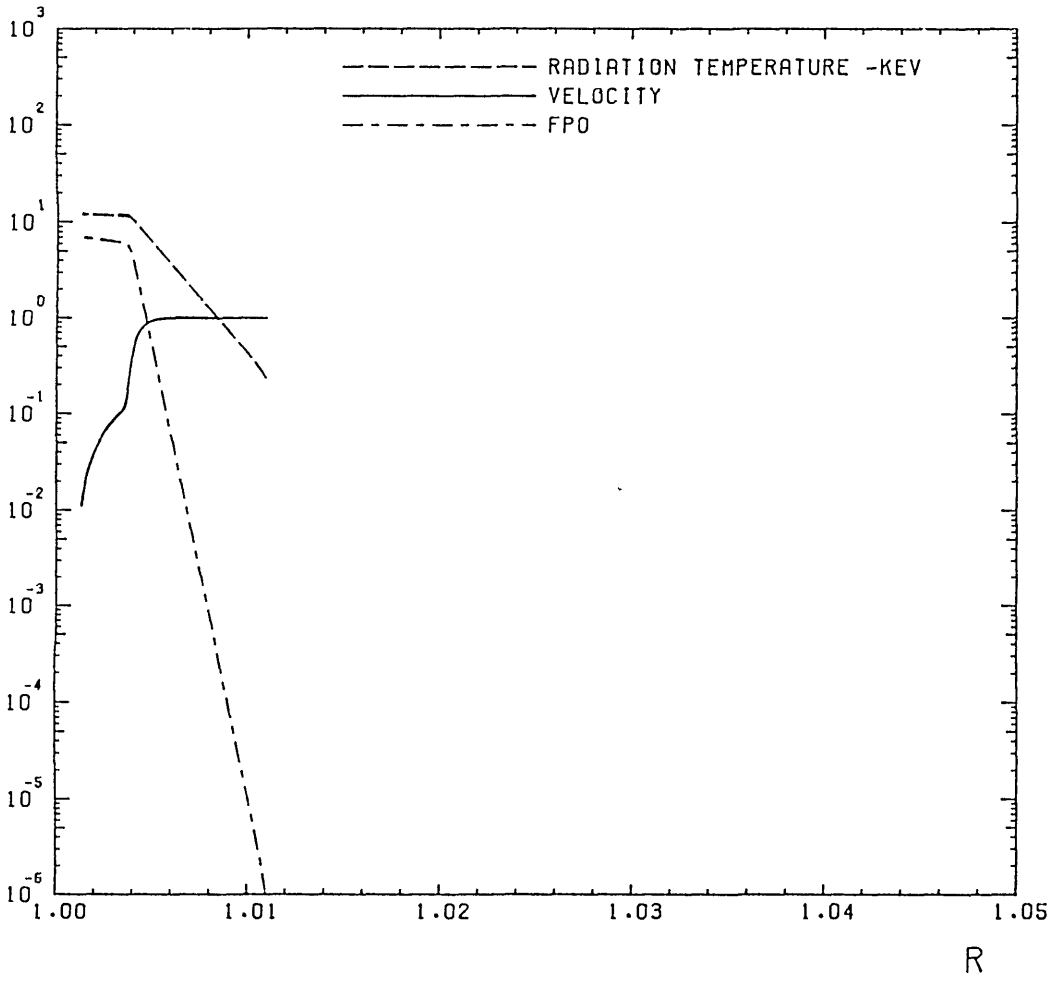

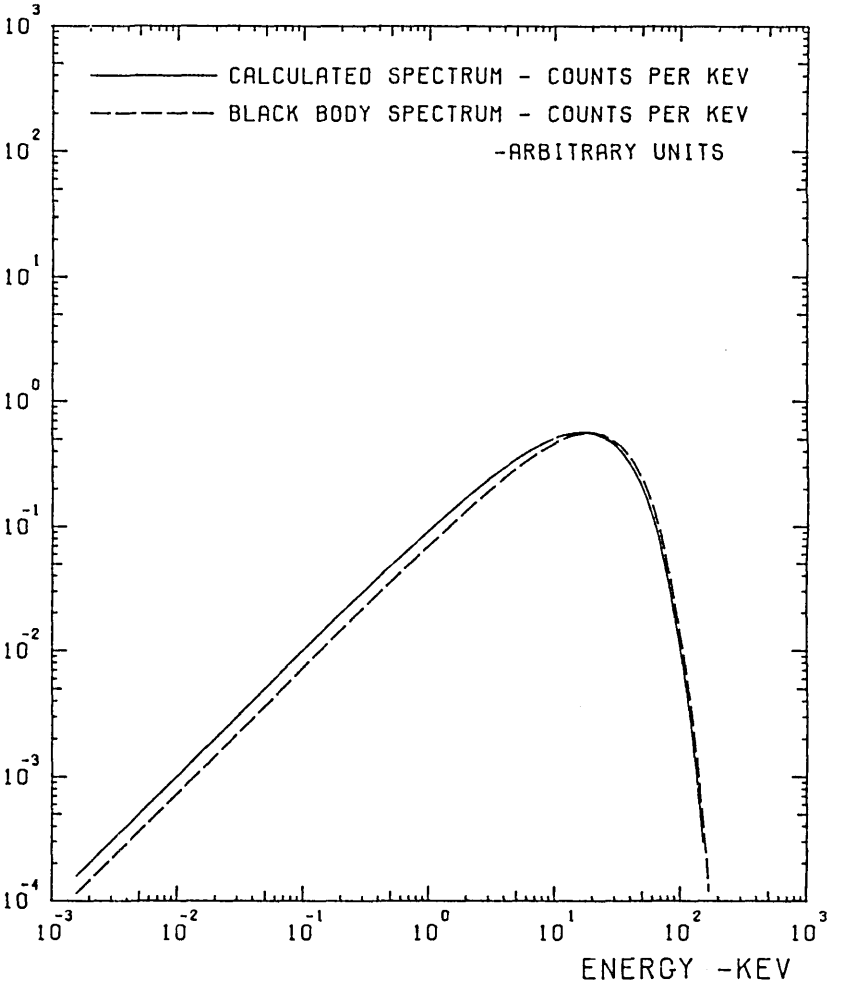

Fig 5.5. Plot of ξ, fp0, fp1 and spectrum at the bottom of the funnel

Parameters of this run-- MASSFC=2×10^{17} $g\ s^{-1}$ $L_x=3.3\times10^{37}$ $erg\ s^{-1}$ $a_1=0.05$

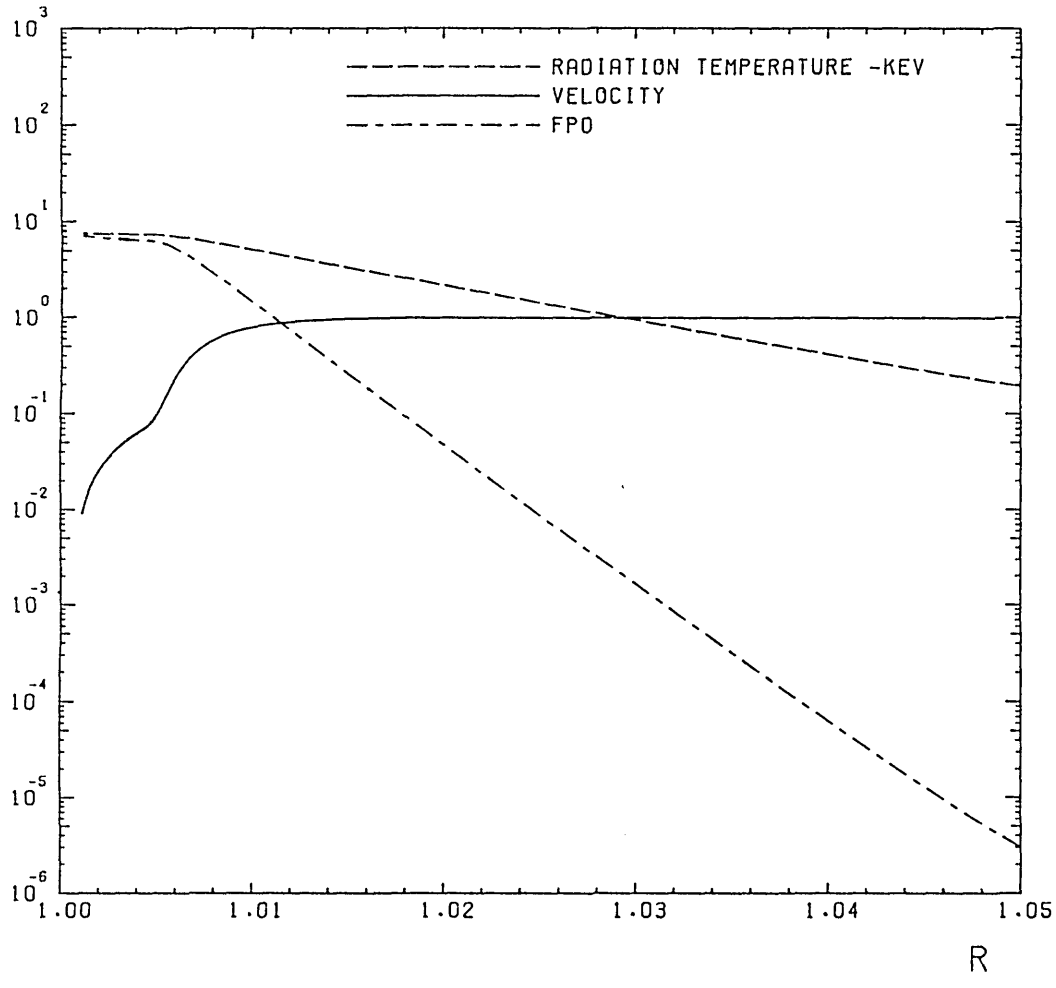

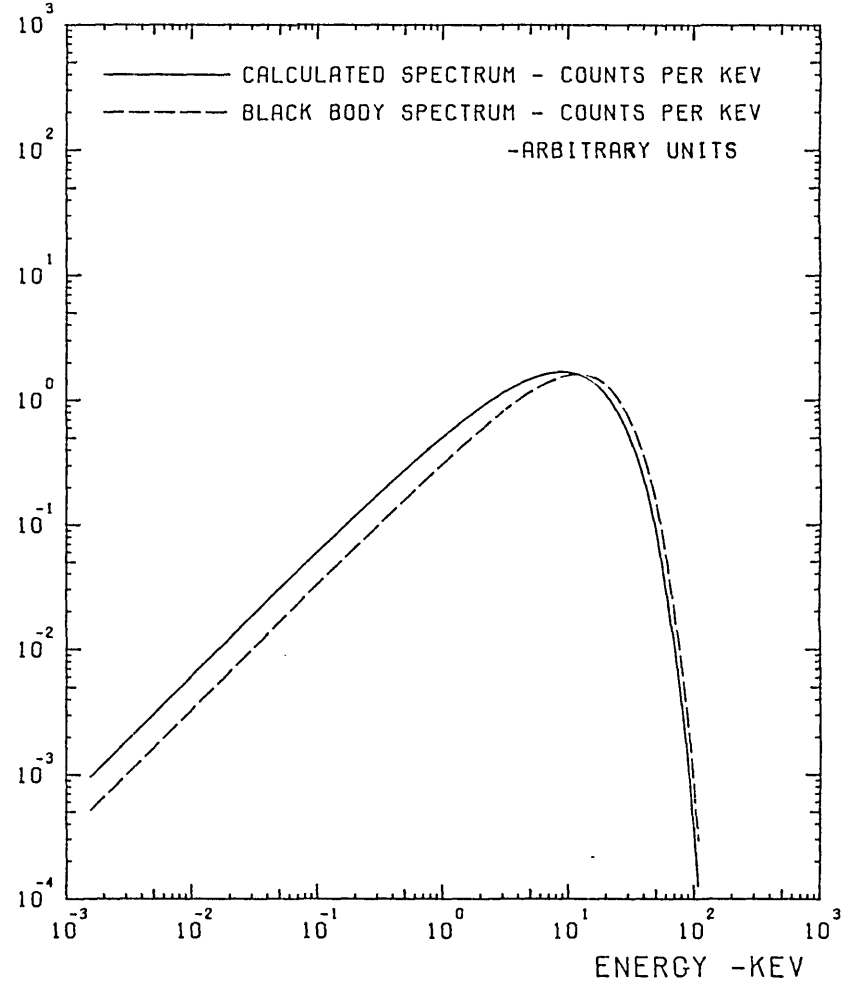

Fig 5.6. Plot of ξ, fp0, fp1 and spectrum at the bottom of the funnel

Parameters of this run-- MASSFC=2×10^{17} $g\ s^{-1}$ $L_x=3.4\times10^{37}$ $erg\ s^{-1}$ $a_f=0.10$

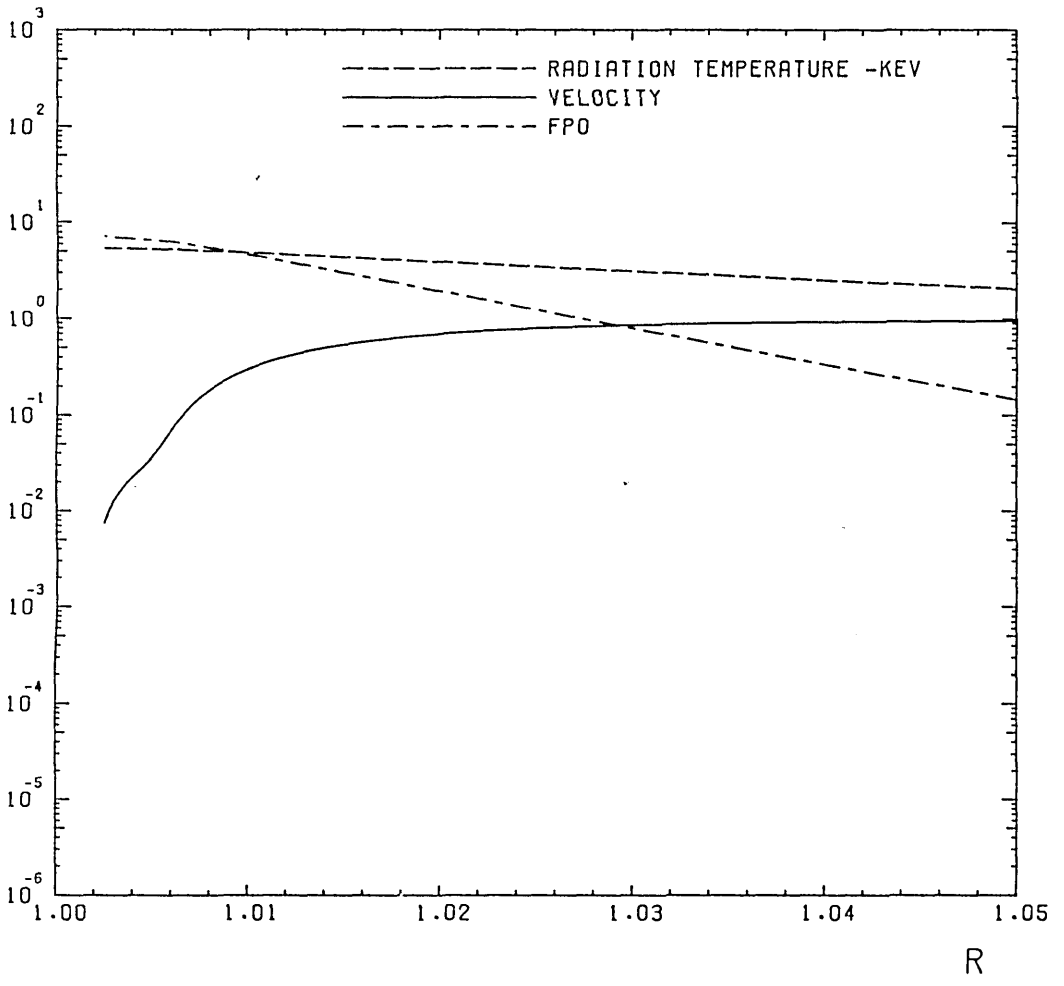

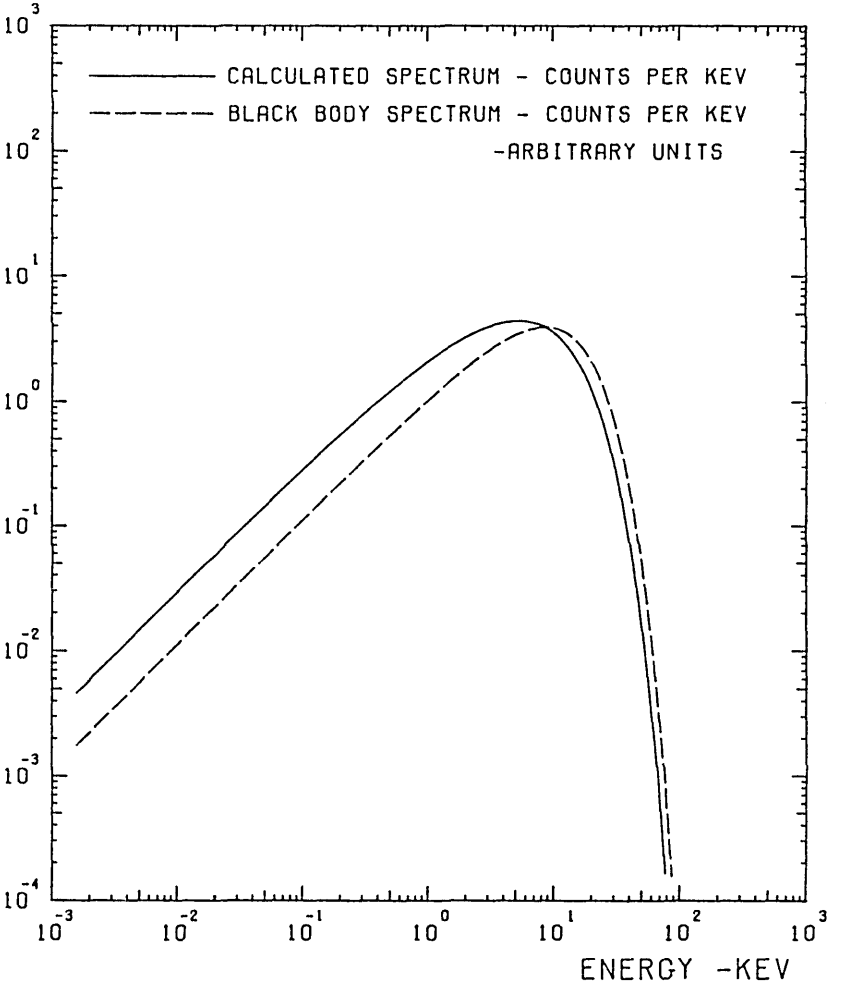

Fig 5.7. Plot of ξ, fp0, fp1 and spectrum at the bottom of the funnel

Parameters of this run-- MASSFC=1×10^{17} $g\ s^{-1}$ $L_x=1.7\times10^{37}$ $erg\ s^{-1}$ $a_f=0.05$

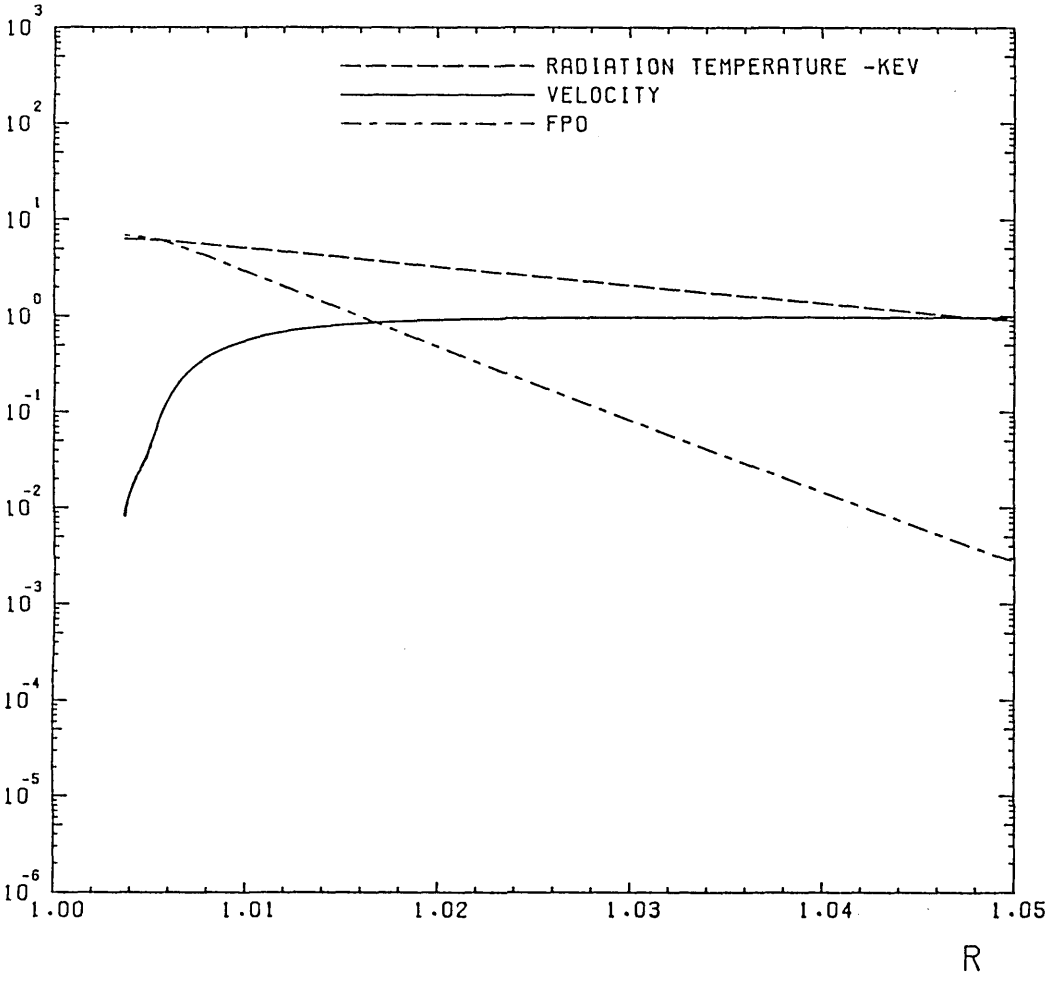

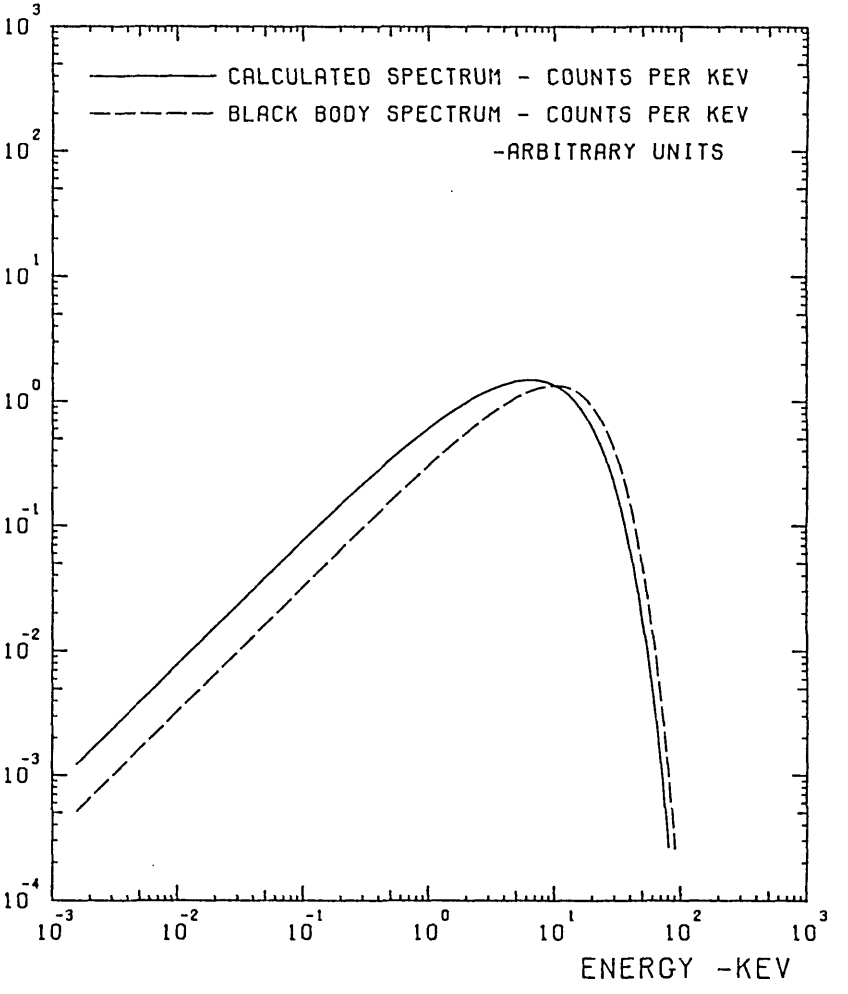

Fig 5.8. Plot of ξ, fp0, fp1 and spectrum at the bottom of the funnel

Parameters of this run-- MASSFC=5×10^{17} $g\ s^{-1}$ $L_x=8.1\times10^{37}$ $erg\ s^{-1}$ $a_f=0.05$

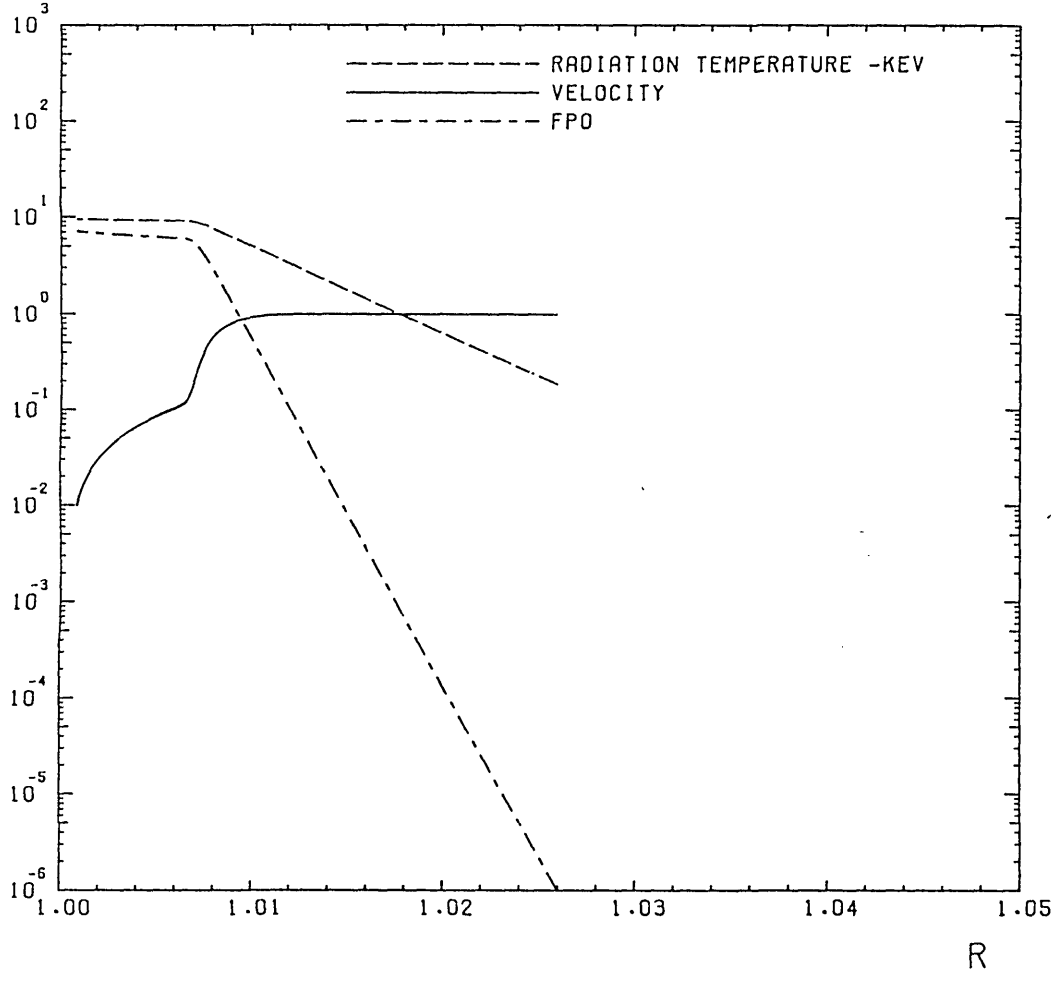

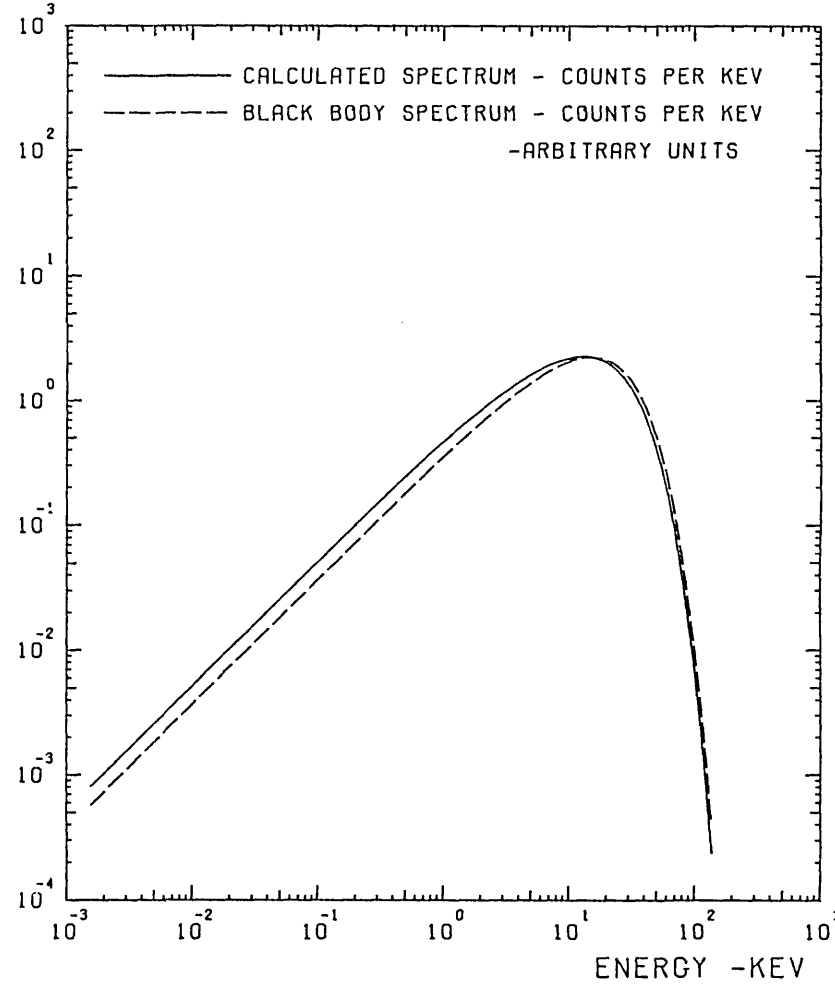

Fig 5.9. Plot of ξ, fp0, fp1 and spectrum at the bottom of the funnel

Parameters of this run-- MASSFC=2×10^{18} $g\ s^{-1}$ $L_x=3.2\times10^{38}$ $erg\ s^{-1}$ a_f=0.10

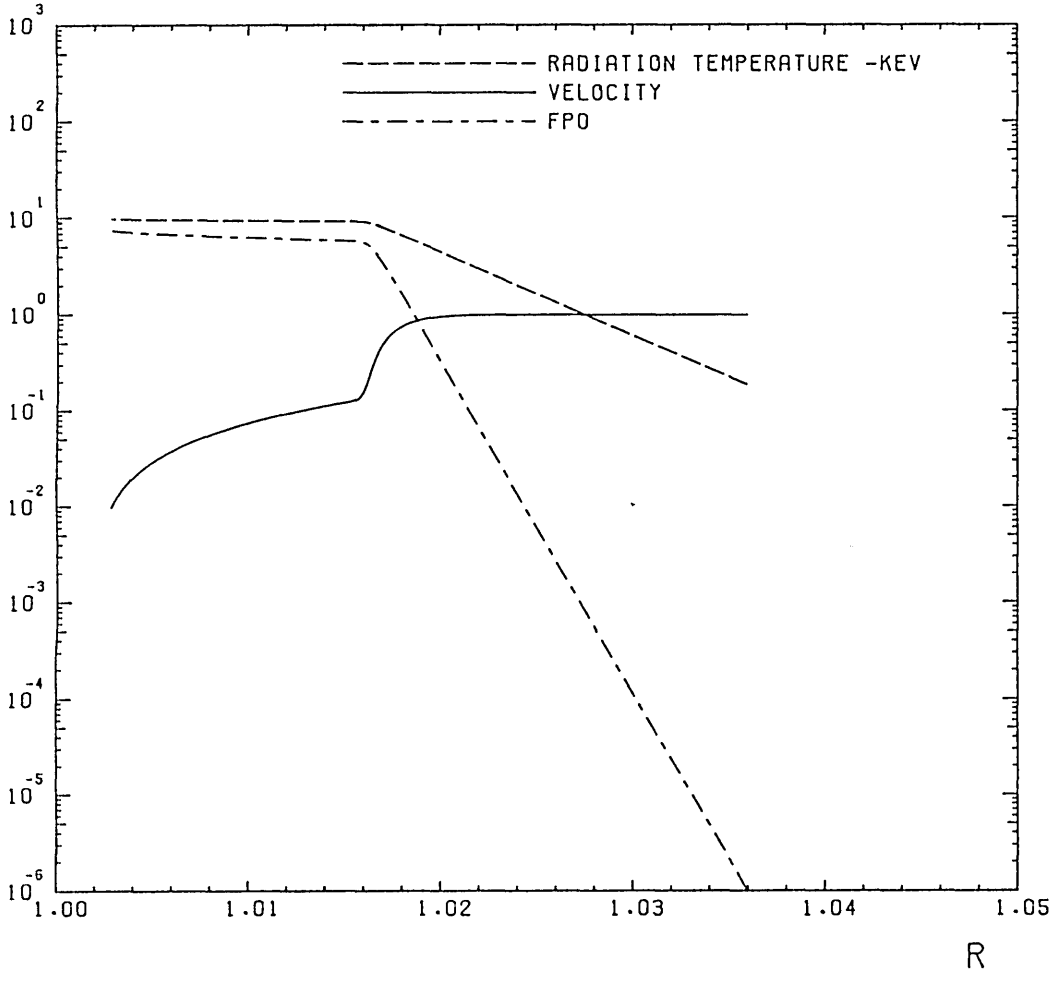

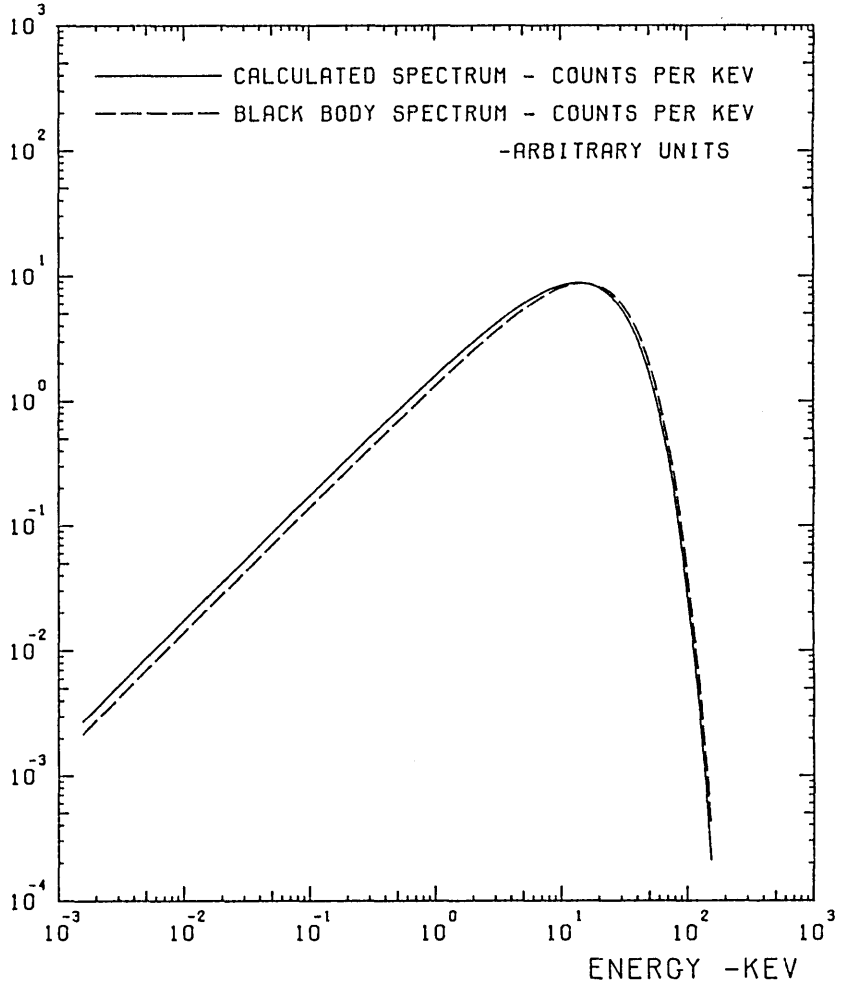

Fig 5.10. Plot of ξ, fp0, fp1 and spectrum at the bottom of the funnel

Parameters of this run-- MASSFC=2×10^{18} $g\ s^{-1}$ $L_x=3.3\times10^{38}$ $erg\ s^{-1}$ $a_f=0.20$

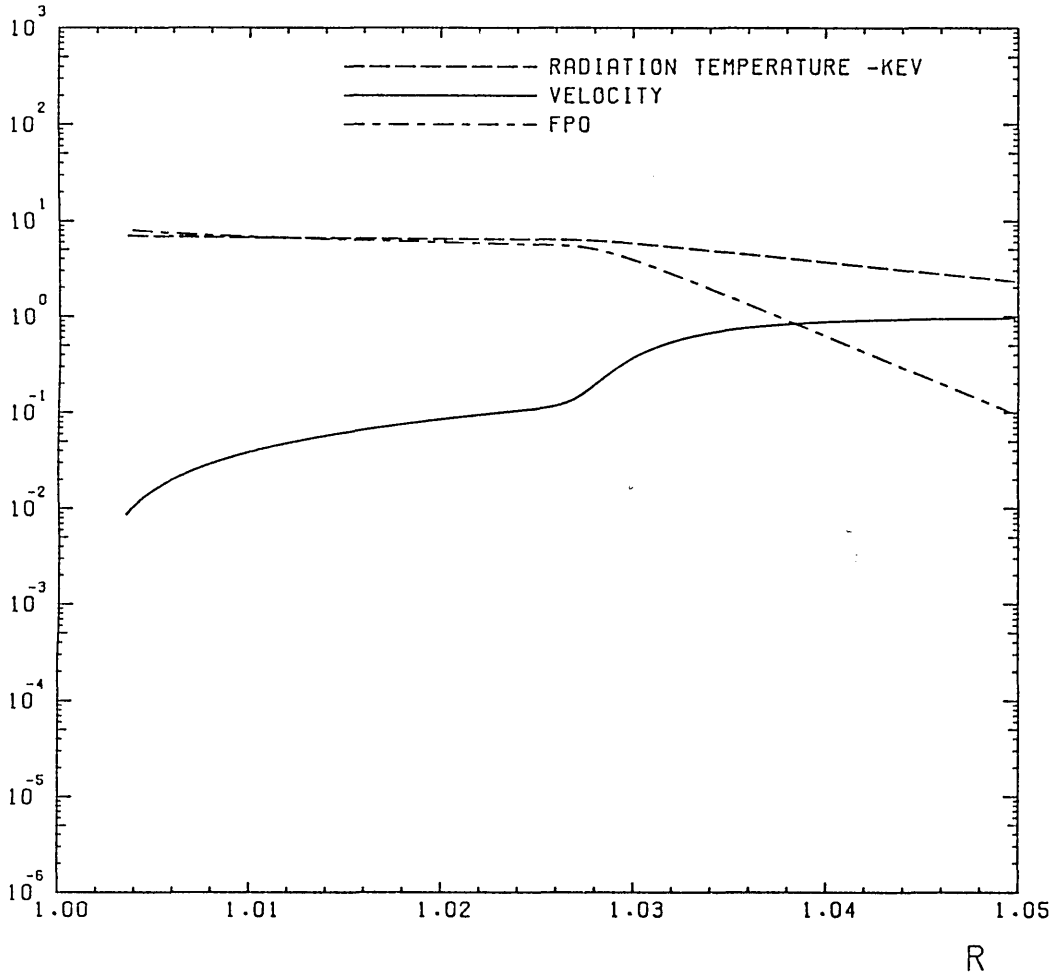

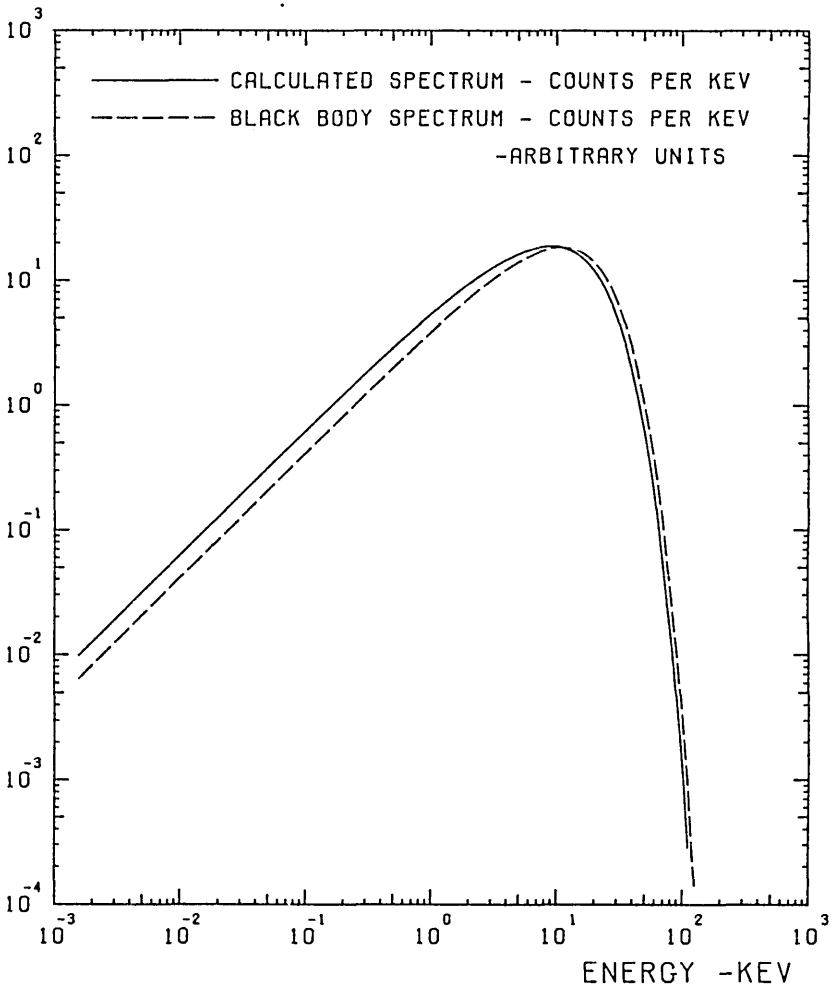

Fig 5.11. Plot of ξ, fp0, fp1 and spectrum at the bottom of the funnel

Parameters of this run-- MASSFC=2×10^{19} $g\ s^{-1}$ $L_x=3.2\times10^{39}$ $erg\ s^{-1}$ $a_1=0.20$

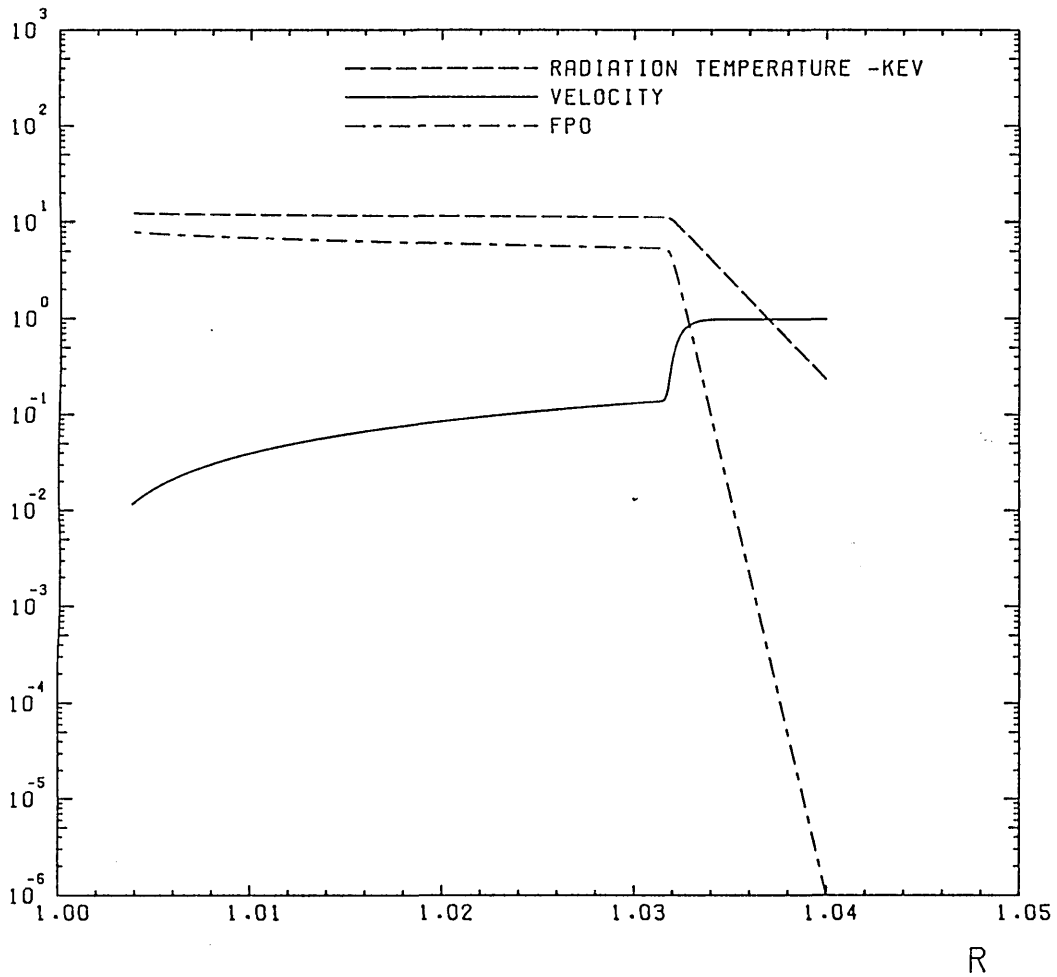

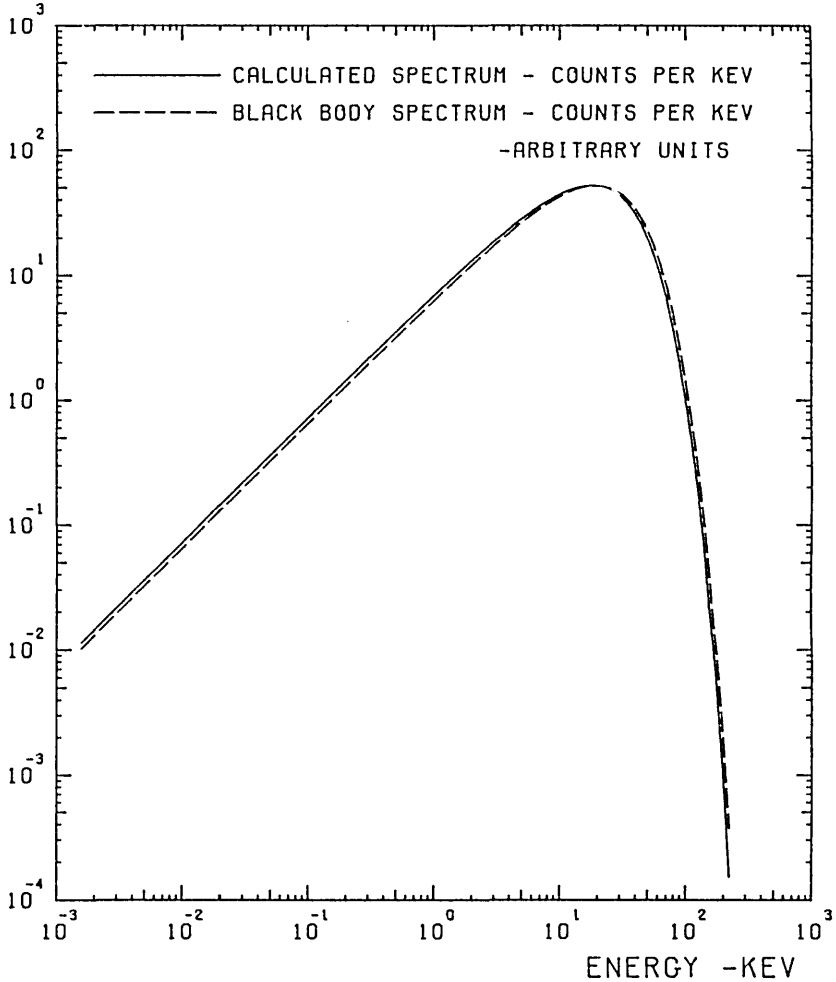

CHAPTER 6

Accretion flow in the funnel where the flow is not dominated by radiation pressure.

§6.1. Discussion.

This chapter considers accretion flow down an accretion funnel where the flow is approximately free falling towards the magnetic pole. The funnel can be divided into 2 regions; the first being that remote from the bottom of the funnel where the bulk of the radiation production is ocurring, and the second where the radiation is diffusing upwards through the free falling plasma.

In the first region heating and cooling processes in the free falling plasma are considered. The time scales for the various processes that may occur in plasmas are compared to see if the matter flowing is hot enough to contribute substantially to the radiation emitted by the accreting neutron star. Effects considered include Coulomb energy exchange, Bremsstrahlung, Cyclotron emission, and adiabatic heating.

The second section discusses the region just above where the radiative shock occurs in chapter 5; and how a radiative transfer treatment of the radiation in this region would be a way to improve the model in this thesis. In chapter 5 the radiation is treated dynamically assuming a black body spectrum: which is a reasonable approximation for the dynamical slowing down of the accretion flow, but does not properly describe the radiation energy spectrum as the radiation diffuses upwards through the infalling matter.

§6.2. Time scales for processes in free falling plasma.

This section compares time scales for various processes in the plasma free falling down the accretion funnel. The fastest time scale found in chapter 3 was that for energy exchange between protons and electrons due to Coulomb scattering. The time scale given in the formula in §3.4. is:–

$$\Delta t_C = \frac{T_e^{3/2}}{4.9 \times 10^5 \rho \ln \Lambda}$$

ρ is taken equal to the value for a free falling plasma derived in §4.3.5.

$$\rho_r = \frac{L_x r_*^2}{(2GM)^{3/2} \pi a_f^2 r^{5/2}}$$

This gives a value of Δt_C given by:–

$$\Delta t_C = 1.23 \times 10^{-9} \left(\frac{T_e}{1keV}\right)^{3/2} \left(\frac{3 \times 10^{37} erg\, sec^{-1}}{L_x}\right) \left(\frac{a_f}{0.05}\right)^2 \left(\frac{r}{r_*}\right)^{5/2} sec$$

This time scale may be compared to the time scales of radiation processes to see if $T_e = T_p$ at all times.

Also of importance is the time between collisions between electrons and protons in the plasma; this is compared to time taken for the electron to complete one cylotron orbit of the magnetic field. If this time between collisions is very much greater than the cylcotron time then plasma processes where the electron is orbiting the magnetic field between collisions are worth considering.

The collision frequency for electrons in a plasma is given in *Boyd + Sanderson 1969* and is:–

$$\nu_{Col} = \frac{\omega_p \ln \Lambda}{2\pi n \lambda_D^3}$$

taking the time between collisions as $1/\nu_{Col}$ and substituting for λ_D (the Debye length), ω_p (the plasma frequency) and $n = \rho/m_p$ and using the analytical expression for ρ gives:–

$$t_{Col} = 2.68 \times 10^{-13} \left(\frac{T_e}{1keV}\right)^{3/2} \left(\frac{a_f}{0.05}\right)^2 \left(\frac{3 \times 10^{37} erg\, sec^{-1}}{L_x}\right) \left(\frac{r}{r_*}\right)^{5/2} sec$$

The time taken for the electron to complete one orbit in the magnetic field is:–

$$t_{orbit} = \frac{2\pi}{\omega_B} = 2\pi \frac{m_e c}{eB}$$

assuming that at the stellar surface the magnetic field is 5×10^{12}gauss and the magnetic field is that of a dipole then:–

$$B_r = B_\star \left(\frac{r_\star}{r}\right)^3 = 5 \times 10^{12} \left(\frac{r_\star}{r}\right)^3$$

therefore:–

$$t_{orbit} = 2\pi \frac{m_e c}{5 \times 10^{12} e} \left(\frac{r}{r_\star}\right)^3 = 7.14 \times 10^{-20} \left(\frac{r}{r_\star}\right)^3 sec$$

this is obviously very much less than the time between collisions between protons and electrons.

Next consider what heating processes may occur in a magnetic field. As the electron is likely to complete a number of orbits before a collision occurs it is worthwhile to consider orbit theory processes in a magnetic field. Conservation of the first adiabatic invariant causes motion parallel to the magnetic field to be converted into motion perpendicular to the magnetic field; this perpendicular motion being converted to thermal energy by collisional redistribution. Between collisions, magnetic moment about the B field is conserved, see for example *Boyd + Sanderson 1969.*

$$m_e \frac{dv_\parallel}{dt} = -\frac{e}{c}\frac{r_L}{2} v_\perp \frac{dB}{dz}$$

where r_L is the Larmor radius. If we assume that the prependicular velocity is due to thermal energy, and substitute for the Larmor radius ($r_L = v_\perp \frac{mc}{eB}$) then

$$\frac{dv_\parallel}{dt} = -\frac{2k_B T_e}{m_e}\frac{1}{B}\frac{dB}{dz}$$

next assume that the loss of kinetic energy parallel to the magnetic field is converted into thermal energy by the collisions taking place, i.e.

$$\frac{dE}{dt} = -m_e v_\parallel \frac{dv_\parallel}{dt} = v_\parallel 2k_b T_e \frac{1}{B}\frac{dB}{dz}$$

per electron. As the cross-sectional area of the funnel is proportional to $1/B$; this is equivalent to adiabatic heating.

Next compare the bremsstrahlung emission time scale to the time scales above. Again, from §3.4.

$$\Delta t_B = 8.1 \times 10^{-14} \frac{T_e^{1/2}}{\rho} sec$$

again, substituting for the density if the plasma is free falling:–

$$\Delta t_B = 3.55 \times 10^{-7} \left(\frac{3 \times 10^{37} erg\, sec^{-1}}{L_x}\right) \left(\frac{a_f}{0.05}\right)^2 \left(\frac{T_e}{1keV}\right)^{1/2} \left(\frac{r}{r_\star}\right)^{5/2} sec$$

As found in chapter 3 this is a much longer time scale than that for thermal equilibrium between protons and electrons.

Next test whether the heating process due to adiabatic heating is more rapid than cooling due to thermal bremsstrahlung calculate the time scale of adiabatic heating.

$$\frac{dP_g}{dt} \sim -P_g v_{ff} \frac{1}{A} \frac{dA}{ds}$$

where s is the direction along which the matter is travelling (i.e. $-\mathbf{r}$ direction). Since $A = A_\star \left(\frac{r}{r_\star}\right)^3$ and remembering that $v_{ff} = -\sqrt{\frac{2GM}{r}}$ then:–

$$\Delta t_{ad} = \frac{r}{3v_{ff}} = \frac{r^{3/2}}{3\sqrt{2GM}} = 3.75 \times 10^{-5} \left(\frac{r}{r_\star}\right)^{3/2} sec$$

Taking the ratio $\Delta t_{ad}/\Delta t_B$ this is only less than 1 if

$$\left(\frac{3 \times 10^{37} erg\, sec^{-1}}{L_x}\right) \left(\frac{r}{r_\star}\right) \gg 100$$

for our usual values of a_f and $r_\star$.

Above and in earlier chapters the cross-sectional area of the funnel is taken to be proportional to r^3. This means that the angle subtended by the radius of the funnel from the centre of the neutron star is proportional to $r^{1/2}$. In the calculations in chapter 3, the model for the outer region followed the flow around the magnetosphere to the magnetic axis, which was at a radius $\sim 200 r_\star$ from the centre of the neutron star. In our most common case we take $a_f = 0.05$, which means that the angle subtended by the radius of the funnel at the stellar surface is 0.05 radians. If the r^3 cross-sectional area of the funnel is extended out to $\sim 200 r_\star$ then the angle subtended by the radius of the accretion funnel at this point $\sim \sqrt{200} \times .05 = 0.7$ radians. This is not compatible with the flow pattern along a narrow flux tube around the magnetosphere described in chapter 3. The above may indicate that accretion is likely to follow the pattern illustrated in Fig 2.7. The flow pattern that causes an accretion funnel of this radius at the surface of the star requires further investigation.

There is one more important time scale to consider here; the time scale for cyclotron emission. From *Katz 1985* the time scale is:–

$$t_{cyc} = 2.4 \times 10^{-4} \left(\frac{B}{10^6 gauss} \right)^{-2} sec.$$

For the case of a high magnetic field at the surface of the neutron star of $\sim 5 \times 10^{12} gauss$ this gives:–

$$t_{cyc} = 1.04 \times 10^{-17} \left(\frac{r}{r_\star} \right)^6 \left(\frac{5 \times 10^{12} gauss}{B_\star} \right)^2 sec$$

As can be seen from above, this time scale is very short. Even though this time scale is short it may not have a dominant effect on the physics. This is because cyclotron emission can be considered to be a coherent scattering process; if an electron gets into an excited state it rapidly falls to its lower energy state releasing the amount of energy originally required to excite it.

From this section we may conclude that except for where the density is very low in the cases of sources having a luminosity at the lower limit of our model; cooling processes are much faster than the heating processes considered. This indicates that the temperature of the plasma in this region is not in the *keV* energy range and therefore does not contribute to the X-ray emission. As the plasma is at a low temperature, recombination may occur thus the plasma may not be fully ionised. Processes that may occur in this case are beyond the scope of this thesis. It is probably a reasonable assumption that the regions higher up the funnel remote from where the slowing down occurs to not contribute substantially to the radiation output of these sources.

§6.3. Radiative transfer through cylinder of free falling plasma

In the model in chapter 5 it was found that the radiation density decayed very rapidly as the radiation diffused upwards through the infalling plasma. This short decay length is because the radiation is assumed to be forced downwards by the free falling plasma; which is flowing at a speed of $\sim c/3$.

In chapter 5 the radiation is assumed for simplicity to have a black body spectrum corresponding to that for the radiation energy density at any given r. This assumption was made in order that the problem be solvable and because the optical depth across the funnel with respect to Thomson scattering is large. The distance over which the radiation decays, as shown from the computations of the model and calculated from the dominant terms in the $v \sim v_{ff}$ region of the model assumed the Thomson opacity. This may be a reasonable calculation for the distance over which radiation may decay, but it is unlikely to be thermalised over this distance as the distance over which scattering occurs is very much shorter than the distance over which absorption occurs. The radiation temperature in this region is likely to be greater than that calculated in the model described in chapter 5.

A better description of the radiation in this region above where the slowing down takes place would be to describe the detailed radiative transfer equations in this region. This could be done by assuming black body radiation at the point where the slowing down begins to occur, and considering radiative transfer up through a cylinder of free falling plasma. This would not be a trivial problem as the infalling plasma would be heated by the radiation travelling upwards through the infalling plasma. Radiative transfer is described in general by *Mihalas 1978*; and radiative transfer to order v/c through matter flowing at a velocity v is studied by *Mihalas + Klein 1982*. In order to model a more realistic radiation output spectrum detailed absorption and emission processes would need to be taken into account; preferably including values for the Thomson and Compton cross sections in a high magnetic field and cylcotron emission. Such a study would indicate whether the radiation density does decay over such a short distance as that found in chapter 5 and may give a better model of the spectra of the observed objects. The full radiative transfer problem is beyond the scope of this thesis. Below is an order of magnitude calculation of processes just above where slowing down begins.

In the model in chapter 5, for the case where $L_x = 3 \times 10^{37} erg\, sec^{-1}$ and $a_f = 0.05$ the black body temperature just above the radiative shock was $\sim 4keV$. *Felten + Rees 1972* consider radiative transfer through a slab of plasma, and calculate a scale length over which absorption of radiation due to thermal bremsstrahlung takes place. The photons are scattered a multiple of times between absorption due to Compton scattering. The effective length between absorption is $L = \sqrt{\frac{3}{\chi_{es}\chi_{ff}}}$ Use their formulae for χ_{es} and χ_{ff} and the number density calculated from §4.3.5. When $r \sim r_*$ gives a length for this opacity $\sim 6.8 \times 10^5 cm$ when $T_r = 4keV$ and the other parameters as described above. This is larger than the diameter of the funnel $(= 2a_f r_*) = 1.5 \times 10^5 cm$. Therefore Felten + Rees's model cannot be directly applied to the case we are considering. This also shows that radiation emitted may escape with much of its original energy in the free falling region even though any photon will have undergone many scatterings.

The manner in which the radiation from the top of the shocked region heats the infalling plasma is now considered. The heat input to the infalling gas may be approximated by:–

$$H = \sigma_{ff} n \left(\frac{r_s}{r - r_s} \right)^2 F e^{-(r-r_s)/\lambda_d}$$

where $\sigma_{ff} n = \chi_{ff}$ and F is the radiation flux from the top of the shock. r_s is the shock radius and λ_d is the decay length of the radiation due photons being scattered out from the sides of the funnel. Putting in the parameters of the model, and taking $F = \sigma T_r^4$ gives:–

$$H = 5.875 \times 10^{18} \left(\frac{r}{r + r_s} \right)^2 e^{-(r-r_s)/\lambda_d}$$

From this it is possible to calculate the time scale for heating, which is equal to $3nk_bT/H$, $3nk_bT$ being the heat capacity of the gas. Therefore this time scale is:–

$$t_H = 1.4 \times 10^{-6} \left(\frac{r}{r - r_s} \right) e^{-(r-r_s)/\lambda_d}$$

As each time a Compton scattering takes place the photon is diverted form its path λ_d is related to the distance between scatters, $(= 1/n\sigma_{es}) \sim 3500cm$ in the case considered here. It is clear that a photon cannot travel very far without being scattered out of the funnel, which is in agreement with the earlier assumption that most of the funnel is remote from the radiation emitted at the bottom of the accretion funnel.

Acknowlegements.

I would like to thank my supervisor, Dr. John Quenby for supervising my work, allowing me to work in the Astrophysics group, many useful discussions, lots of encouragement and being very tolerant of me. I would also like to thank earlier heads of groups, Prof. Jim Ring and Prof. Peter Hedgecock for allowing me to work in their Research groups.

Special thanks to Dr. Rees Williams for friendship, encouragement and being a good office mate.

I would also like to thank Dr. Richard Lieu for several useful discussions and lots of encouragement.

I would also like to thank those staff at the computer centre who have given me help and moral support, especially Dr. Mark Lee who helped me use the system on which this document was produced.

I would like to thank everyone else who has given me moral support, especially my friends Andrea Prestwich, Antonia Tomoszek, Sunil Sidher, Claire Tonkinson and Tom Hicks.

Also many thanks to Natasha Sykes for proof reading this thesis.

Last but certainly not least I would like to thank my Mum for lots of encouragement and helping me buy my flat so that I did not have to worry about accomodation while I wrote this document.

From October 1981 to September 1984 I received a Postgraduate Student grant from the Science and Engineering Research council.

This Thesis was produced using TEXon an IBM PC-AT at Imperial college computer centre. The diagrams (not including plots of numerical results) were produced using PAFEC DOGS on a DEC VAX 8600 at Imperial college computer centre. The computational studies were carried out using a CDC Cyber 855 mainframe computer, and the graphs plotted on a BENSON 1645 plotter, both at Imperial college computer centre.

Appendix 1

The implicit 1 step method.

The second order implicit 1 step method is a well known standard method for solving either a single first order ordinary differential equation or a system of first order ordinary differential equations. The second order implicit 1 step method is sometimes also known as the trapeziodal method. This method is second order accurate meaning that for a step length h where h is small compared to the scale length of change of the variables the error is proportional to h^2.

Assume an ordinary differential equation of the form:–

$$\frac{dy}{dx} = f(x, y)$$

then the implicit 1 step method approximates the value for y at the (n+1)th step as:–

$$y^{n+1} = y^n + \frac{h}{2}\left(f(y^{n+1}, x^{n+1}) + f(y^n, x^n)\right)$$

where, for example $f(y^n, x^n)$ refers to the value of the function of the ordinary differential equation when the values for x and y at the nth step are taken. h is the step size. If a numerical scheme is implicit, it means that the right hand side contains terms requiring values at (n+1) that are not yet known. Obviously, in this case the value of $f(y^{n+1}, x^{n+1})$ is not yet known as y^{n+1} is not yet known. Thus we introduce the predictor-corrector method. One example of how this may be done is for the first approximation to the term on the left hand side to take the value equal to that at the previous step; thus effectively reducing the first approximation to the calculation of y^{n+1} to the Euler method. This new value is then put in the right hand side and the next approximation was calculated; thus:–

$$y^{n+1\,[S]} = y^n + \frac{h}{2}\left(f(y^{n+1\,[S-1]}, x^{n+1}) + f(y^n, x^n)\right)$$

Where $[S]$ is the number of iterations carried out. This process is carried out at each step until:–

$$\frac{\left(y^{n+1\,[S]} - y^{n+1\,[S-1]}\right)}{y^{n+1\,[S-1]}} \leq \delta$$

where δ is small.

In the case described in chapter 3 a system of 2 first order differential equations are to be solved that are effectively in the form:–

$$\frac{dP_g}{ds} = f_1(v, P_g, s)$$
$$\frac{dv}{ds} = f_2(v, P_g, s)$$

The Implicit 1 step method was therefore applied alternately to both these equations, and the iterative process carried out until the values for both v and P_g converged.

There are several methods for deriving the implicit 1 step method and showing that it is second order accurate, these derivations are described in *Lambert 1973 and Potter 1973.*

Appendix 2.

Program to calculate the spectrum from a series of black bodies.

```
C ================================================================
C
      PROGRAM BFSPEC1(INPUT,OUTPUT,TAPE5=INPUT,TAPE6=OUTPUT)
C
C ================================================================
C
C PROGRAM TO CALCULATE THE SPECTRUM FROM A SERIES OF BLACK BODY
C TEMPERATURES AS A FUNCTION OF R.
C
C THIS VERSION BFSPECC CALCULATES AS COUNTS PER UNIT ENERGY
C
      COMMON/BLOCK1/RCMIN
      REAL R(2000),RINT(2000),TR(2000),BBFN(2000),RINT2(2000)
      REAL BBFN2(2000),RTRY(2000),TRTRY(2000),MASSFC,NM
      PARAMETER(WEIN=1.593624)
C
      OPEN(UNIT=3,FILE='BFSVAL')
      OPEN(UNIT=4,FILE='BFPDAT')
C
      FACT=-2.8
      STEP1=.05
      STEP2=.01
C
      READ(5,1) IREF
C
      WRITE(6,2) IREF
    2 FORMAT(1H1,'RUN REFERENCE=',I3/1X)
C
      READ(5,11) GM,RSTAR,MASSFC
      READ(5,21) AINDEX,NM,FBB,AF
      READ(5,31) RS,ETA2,FP0S,FP1S
      READ(5,41) TOL,IFAIL
    1 FORMAT(I4)
   11 FORMAT(1X,3(1PE11.4,3X))
   21 FORMAT(1X,4(1PE11.4,3X))
   31 FORMAT(1X,4(1PE11.4,4X))
   41 FORMAT(1X,1PE11.4,4X,I2)
C
C READ THE VARIABLES
C
      DO 10 I=1,2000
      READ(5,20,END=50) R(I),TR(I)
   20 FORMAT(1X,F12.9,59X,1PE15.8)
      NVAL=I
   10 CONTINUE
C
   50 CONTINUE
C
      READ(4,*) NINT,RCMIN
C
```

```
      WRITE(6,8) RCMIN
    8 FORMAT(1X,'RCMIN=',1PE11.4)
C
C WRITE FIRST FEW VALUES TO OUTPUT TO CHECK THAT IT IS READING
C
      WRITE(6,55)
   55 FORMAT(1X/5X,'--R--',10X,'--TR--')
      DO 60 I=1,20
      WRITE(6,61) R(I),TR(I)
   60 CONTINUE
C
      WRITE(6,62) NVAL
C
   61 FORMAT(1X,2(1PE11.4,4X))
   62 FORMAT(1X,'NVAL=',I4)
      WRITE(3,63) NVAL
   63 FORMAT(1X,I4)
C
C NEED TO CUT OUT VALUES THAT ARE TOO CLOSE TOGETHER IN R
C
      CALL RELIM(NVAL,NUSE1,R,TR,RTRY,TRTRY)
C
C WRITE THE VALUES OF T AND R AFTER RELIM
C
      WRITE(6,122)
      WRITE(6,125) (RTRY(I),TRTRY(I) I=1,NUSE1)
  125 FORMAT(1X,2(1PE11.4,3X))
  122 FORMAT(1X/2X,'RTRY',11X,'TRTRY')
C
C WRITE NUMBER OF VALUES USED AFTER THOSE TOO CLOSE IN R HAVE BEEN
C ELIMINATED
C
      WRITE(6,64) NUSE1
   64 FORMAT(1X/1X,'NUSE1=',I4)
C
C FIND THE PEAK IF THE OUTPUT WAS SIMPLY 1 BLACK BODY FUNCTION
C WITH TR=TRSTAR
C
      TSTAR=TR(NVAL)
      BBPEAK=TSTAR*WEIN
C
      WRITE(6,70) TSTAR,BBPEAK
   70 FORMAT(1X/1X,'TSTAR=',1PE11.4,3X,'BBPEAK=',1PE11.4)
C
C NEXT NEED TO CALCULATE THE VALUE OF THE SPECTRUM AT THIS ENERGY
C FOR NORMALISATION.
C
      CALL SCALC(NUSE1,NUSE2,RTRY,TRTRY,BBPEAK,ANSWR,AERR)
      SE=100.*AF*BBPEAK**2*ANSWR
      BBMULT=SE/BLACK1(TSTAR,BBPEAK)
C
C NOW START CALCULATING THE SPECTRUM
C
      WRITE(6,65)
   65 FORMAT(1H1/2X,'--E--',9X,'--S--',9X,'--BB--',8X,'--AINTG--',5X,
     + '--ERROR--',5X,'POINTS USED')
C
```

```
      DO 100 N=1,300
C
      E=10.**FACT
      CALL SCALC(NUSE1,NUSE2,RTRY,TRTRY,E,ANSWR,AERR)
      SE=100.*AF*E**2*ANSWR
      BB=BBMULT*BLACK1(TSTAR,E)
C
      WRITE(3,220)  E,SE,BB
      WRITE(6,221) E,SE,BB,ANSWR,AERR,NUSE2
  220 FORMAT(1X,3(1PE15.8,3X))
  221 FORMAT(1X,5(1PE11.4,3X),I4)
C
      IF(E.GE.(.8*TSTAR).AND.E.LE.2.*TSTAR) THEN
         FACT=FACT+STEP2
      ELSE
         FACT=FACT+STEP1
      ENDIF
      IF(FACT.GT.3.0) GO TO 300
C
  100 CONTINUE
C
  300 STOP
      END
C ================================================================
C
      SUBROUTINE SCALC(NUSE1,NUSE2,R,TR,E,ANSWR,AERR)
C
C ================================================================
C
      REAL R(2000),RINT(2000),TR(2000),BBFN(2000),RINT2(2000),
     + BBFN2(2000)
C
      NUSE2=0
      DO 200 I=1,NUSE1
      PON=E/TR(I)
C
C ONLY USE A GIVEN POINT IF THE EXPONENT IS LESS THAN 500
C
      IF(PON.LE.500) THEN
        NUSE2=NUSE2+1
        BBFN(NUSE2)=R(I)**1.5/(EXP(PON)-1.)
        RINT(NUSE2)=R(I)
      ELSE
      ENDIF
  200 CONTINUE
C
C CHANGE TO GOING IN +VE R DIRN SO THAT INTEGRAL IS POSITIVE
C
      DO 250 J=1,NUSE2
      RINT2(J)=RINT(NUSE2-J+1)
      BBFN2(J)=BBFN(NUSE2-J+1)
  250 CONTINUE
C
C CALL NAG ROUTINE
C
      IFAIL=0
      CALL D01GAF(RINT2,BBFN2,NUSE2,ANSWR,AERR,IFAIL)
```

```
C
      RETURN
      END
C ═══════════════════════════════════════════════
C
      FUNCTION BLACK1(TSTAR,E)
C
C ═══════════════════════════════════════════════
C
C ROUTINE TO CALCULATE SINGLE BLACK BODY VALUE AT ENERGY E
C
      BLACK1=E**2/(EXP(E/TSTAR)-1)
      RETURN
      END
C ═══════════════════════════════════════════════
C
      SUBROUTINE RELIM(NVAL,NUSE1,R,TR,RTRY,TRTRY)
C
C ═══════════════════════════════════════════════
C
C SUBROUTINE TO ELIMINATE VALUES TOO CLOSE TOGETHER
C
      DIMENSION R(2000),RTRY(2000),TR(2000),TRTRY(2000)
      COMMON/BLOCK1/RCMIN
C
      NUSE1=0
C
      WRITE(6,180) RCMIN
  180 FORMAT(1X/2X,'RCMIN=',1PE11.4)
C
      DO 190 I=1,NVAL
      IUSE=0
      IF(I.NE.1) CHANGE=ABS(RTRY(NUSE1)-R(I))
      IF(I.EQ.1) THEN
         IUSE=1
      ELSEIF(CHANGE.GT.RCMIN)  THEN
         IUSE=1
      ELSE
      ENDIF
C
      IF(IUSE.EQ.1) THEN
         NUSE1=NUSE1+1
         RTRY(NUSE1)=R(I)
         TRTRY(NUSE1)=TR(I)
      ELSE
      ENDIF
C
C
  190 CONTINUE
C
      RETURN
      END
```

Appendix 3

Jacobian elements of the system of ordinary differential equations in chapter §5.3.

This appendix gives the jacobian elements of the system of ordinary differential equations as described in §5.5. First replace ξ, f_{p0} and f_{p1} by y_1, y_2 and y_3 respectively. Also for simplicity write $r = r_u$ and $Gv = Gasov2$ The system of first order differential equations then becomes:–

$$\frac{dy_1}{dr} = f_1 = \frac{-\left(\frac{r^3}{7}y_3 + \frac{1}{2y_1r^2}\right)}{\left(1 - Gv\,\frac{y_2^{1/4}}{y_1^2}\right)}$$

$$\frac{dy_2}{dr} = f_2 = y_3$$

$$\begin{aligned}\frac{dy_3}{dr} &= f_3 \\ &= \frac{CD2}{y_1r^3}[K2S\,\frac{y_2}{r^{3/2}} - \left(4y_2 + \frac{2r^{3/2}y_3}{CD2}\right)\frac{3y_1}{r} \\ &+ \frac{1}{\left(1 - \frac{Gv\,y_2^{1/4}}{y_1^2}\right)}[\left(4y_2y_3 + \frac{r^3y_3y_3}{CD2}\right)\frac{r^3}{7} \\ &+ \left(-\left(3 - 4\frac{Gv\,y_2^{1/4}}{y_1^2}\right)y_1 + \frac{r}{2y_1CD2}\right)y_3 \\ &+ \frac{2y_2}{y_1r^2} + \frac{7\,Gv\,y_2^{1/4}}{2r^5y_1^2}]]\end{aligned}$$

The jacobian component $PW(i,j) = \frac{df_i}{dy_j}$ and there are nine such components in all. They are as follows:–

$$PW(1,1) = \frac{\left(1 + \frac{Gv\,y_2^{1/4}}{y_1^2}\right)\frac{1}{2y_1^2r^2} + \frac{2r^3\,Gv\,y_2^{1/4}y_3}{7y_1^3}}{\left(1 - \frac{Gv\,y_2^{1/4}}{y_1^2}\right)^2}$$

$$PW(1,2) = \frac{\frac{-Gv}{4y_2^{3/4}y_1^2}\left(\frac{r^3}{7}y_3 + \frac{1}{2y_1r^2}\right)}{\left(1 - \frac{Gv\,y_2^{1/4}}{y_1^2}\right)}$$

$$PW(1,3) = \frac{\frac{-r^3}{7}}{\left(1 - \frac{Gv\,y_2^{1/4}}{y_1^2}\right)}$$

$$PW(2,1) = 0$$

$$PW(2,2) = 0$$

$$PW(2,3) = 1$$

$$PW(3,1) = \frac{CD2}{r^3}\frac{1}{\left(1 + \frac{Gv\,y_2^{1/4}}{y_1^2}\right)^2} \times [\frac{-K2Sy_2}{r^{3/2}y_1^2}$$
$$+ [-\left(1 + \frac{Gv\,y_2^{1/4}}{y_1^2}\right)\left(4y_2y_3 + \frac{r^3}{CD2}y_3y_3\right)\frac{r^3}{7y_1^2}$$
$$-\left(\frac{r}{CD2} + 2\,Gv\,y_2^{1/4}\right)\frac{y_3}{y_1^3} - \frac{4y_2}{y_1^3r^2}$$
$$-\frac{11.5Gv\,y_2^{1/4}}{r^5y_1^4} - \frac{7\,Gv^2\,y_2^{1/2}}{r^5y_1^6}]]$$

$$PW(3,2) = \frac{CD2}{r^3}\frac{1}{\left(1 - \frac{Gv\,y_2^{1/4}}{y_1^2}\right)^2}[\frac{-K2S}{r^{3/2}y_1} - \frac{12}{r}$$
$$+\left(4 - 3\frac{Gv\,y_2^{1/4}}{y_1^2}\right)\frac{y_3r^3}{7y_1} + \frac{Gv\,r^6y_3y_3}{28\,CD2\,y_2^{3/4}y_1^2}$$
$$+\left(\frac{1}{4} + \frac{r}{8y_1^2\,CD2}\right)\frac{y_3Gv}{y_2^{3/4}y_1^2}$$
$$+\left(1 - \frac{3}{4}\frac{Gv\,y_2^{1/4}}{y_1^2}\right)\frac{2}{y_1^2r^2} + \frac{7}{8}\frac{Gv}{y_1^3y_2^{3/4}r^5}]$$

$$PW(3,3) = \frac{CD2}{r^3}\left[-\frac{6r^2}{CD2} + \frac{1}{\left(1 - \frac{Gv\, y_2^{1/4}}{y_1^2}\right)}\right.$$
$$\left.\times \left[\left(4y_2 + \frac{2r^3 y_3}{CD2}\right)\frac{r^3}{7y_1} - \left(3 - \frac{4\,Gv\, y_2^{1/4}}{y_1^2}\right) + \frac{r}{2y_1^2\, CD2}\right]\right]$$

Appendix 4.

Program for the model of an accreting neutron star near the bottom of the accretion funnel described in chapter 5.

```
C ═══════════════════════════════════════════
C
      PROGRAM BFUNNL4(INPUT,OUTPUT,TAPE5=INPUT,TAPE6=OUTPUT)
C
C ═══════════════════════════════════════════
C
C PROGRAM TO INTEGRATE THE EQUATIONS WHICH OCCUR IN THE
C OPTICALLY THICK, THERMAL EQUILIBRIUM, SLOWING DOWN
C ASSUMED TO BE DUE TO A PRESSURE GRADIENT.
C
C BFUNNL4 IS FORTH VERSION, THIS USES DØ2QAF WHERE V IS LARGE
C AND DØ2QBF IN THE REGION WHERE V<<VFF.
C
C
C  NOUT   = MIN. NUMBER OF EXIT POINTS IF OUTPUT AT GIVEN R
C  IFULL  = NUMBER OF OUTPUT POINTS BETWEEN WRITING VARIUS PARAMS
C  ISTEP  = 1 IF OUTPUT EVERY STEP, Ø OTHERWISE
C         - IF STIFF, ISTEP=1
C  IWRITE = NUMBER OF EXIT POINTS BETWEEN OUTPUT POINTS.
C         - WHEN OUTPUT EVERY STEP
C
C ARRAY FRAC IS AN ARRAY OF VARIABLES USED IN CONTROLLING PROGRAM
C FRAC(1) -  MAX FRACTIONAL CHANGE IN VARIABLE (OUTPUT AT GIVEN R)
C FRAC(2) - IF VELOCITY <  FRAC(2) EXIT EVERY STEP
C FRAC(3) - IF(1-GASOV2*Y2**.25/Y1**2) <FRAC(3) END RUN
C FRAC(4) - IF VELOCITY <  FRAC(4) END RUN
C FRAC(5) - IF COUT(1) (MIN STEP) < FRAC(5) END RUN
C FRAC(6) - IF COUT(1)            < FRAC(6) USE STIFF ROUTINE
C FRAC(7) - IF Y(1) < FRAC(7)  USE STIFF ROUTINE
C FRAC(8) - IF Y(2) > FRAC(8) USE STIFF ROUTINE
C
C IEND ARRAY, USED TO INDICATE WHEN RUN CEASES, AND THE REASON
C IEND(1) = 1 RUN ENDED, REASONS IN OTHER IEND VALUES
C IEND(2) = 1 Y(2) < Ø.
C IEND(3) = 1 Y(2) < Ø.
C IEND(4) = 1 Y(3) > Ø.
C IEND(5) = 1 (1.-GASOV2 Y2**.25/Y1**2) < FRAC(3)
C IEND(6) = 1 Y(1) < FRAC(4)
C IEND(7) = 1 COUT(1) < FRAC(5)
C IEND(8) = 1 NC > 5ØØØ
C
C ISTIFF ARRAY, USED TO INDICATE WHEN CHANGE TO GEARS METHOD
C ISTIFF(1) = 1  USE STIFF METHOD, REASONS FOLLOW
C ISTIFF(2) = 1  COUT(1) < FRAC(6)
C ISTIFF(3) = 1  Y(1) < FRAC(7)
C ISTIFF(4) = 1  Y(2) > FRAC(8)
C
      DIMENSION Y(3),F(3),W(3,22),CIN(7),COMM(5),CONST(5)
     + ,COUT(16),PW(3,3),ISTIFF(5)
C
```

```
      PARAMETER(ARAD=7.56464E-15,AKB=1.38Ø62E-16 C=2.9979E1Ø)
      PARAMETER(AMP=1.67352E-24,AME=9.1Ø956E-28)
      PARAMETER(PI=3.1415926)
C
      EXTERNAL FCN,PEDERV
C
      COMMON/BLOCK1/K2S,CD2,GASOV2,TSTRM
      COMMON/BLOCK2/EFFIC,NOUT,IFULL,IOUT,H,IEND(1Ø)
      COMMON/BLOCK3/FRAC(1Ø)
C
      REAL GM,MASSFC,KAPPA
      REAL LX,LXMAX,LEDD,NM K2S
C
      OPEN(UNIT=1,FILE='BFGVAL')
C
      READ(5,1) IREF
    1 FORMAT(I4)
      WRITE(6,2) IREF
    2 FORMAT(1H1,'REF NO.....G',I4)
      WRITE(1,1) IREF
C
C READ MASS (*G), RADIUS AND MASSFC IN CGS UNITS
C
      READ(5,*) GM,RSTAR,MASSFC
C
      WRITE(6,1Ø) GM,RSTAR,MASSFC
C
C ALSO WRITE INTO BFGVAL FOR FUTURE USE
C
      WRITE(1,11) GM,RSTAR,MASSFC
C
C READ OTHER PARAMETERS FOR THE MODEL
C
      READ(5,*) AINDEX,NM,FBB,AF
C
C NOTE-NOT USING AINDEX AS IT WOULD BE NEEDED IN FUNCTIONS THAT
C ARE FREQUENTLY CALCULATED.
C
      WRITE(6,2Ø) AINDEX,NM,FBB,AF
      WRITE(1,21) AINDEX,NM,FBB,AF
C
      KAPPA=CALKAP(R,Y)
C
C CALCULATE OTHER PARAMETERS THAT ARE PECULIAR TO
C PARAMETERS ALREADY READ
C
      ASTAR=PI*AF*AF*RSTAR*RSTAR
      VFFSTR=SQRT(2.*GM/RSTAR)
      LXMAX=2.*GM*MASSFC/RSTAR
      LEDD=4.*PI*C*GM/Ø.38
      EDMAX=LXMAX/LEDD
C
      CD2=KAPPA*MASSFC/(C*PI*AF**2*RSTAR)
      K2S=1.5*C/VFFSTR/AF
      GASOV2=NM*AKB/AMP*(3./ARAD*MASSFC/ASTAR*VFFSTR/7.)**.25
     + *RSTAR/2./GM
      TSTRM=(3.*MASSFC*VFFSTR/ASTAR/7./ARAD)**.25/1.159E7
```

```
C
C WRITE THESE VALUES THAT NOW DEFINE THE MODEL
C
      WRITE(6,25) ASTAR,VFFSTR,LXMAX,EDMAX,CD2,K2S,GASOV2,TSTRM
C
C READ STARTING VALUES FOR THE VARIABLES
C
      READ(5,*) R,ETA2,FPØ,FP1
C
      WRITE(6,3Ø) R,ETA2,FPØ,FP1
      WRITE(1,31) R,ETA2,FPØ,FP1
C
C READ CONSTANTS NEEDED FOR DØ2QAF
C
      READ(5,*) TOL,NPED
C
      WRITE(6,4Ø) TOL,NPED
      WRITE(1,41) TOL NPED
C
C
      READ(5,*) NOUT,IFULL,ISTEP,IWRITE
      WRITE(6,49)
      WRITE(6,5Ø) NOUT,IFULL,ISTEP,IWRITE
C
C
      READ(5,*) (FRAC(J),J=1,8)
C
      WRITE(6,6Ø) (J,FRAC(J),J=1,8)
C
      IOUT=Ø
C
C NOTE IEND IS AN ARRAY, IF IEND(1) IS 1 INTEGRATION CEASES,
C REST OF ARRAY REPRESENT REASONS FOR ENDING INTEGRATION.
C
      DO 61 I=1,1Ø
      IEND(I)=Ø
   61 CONTINUE
C
      DO 62 I=1,5
      ISTIFF(I)=Ø
   62 CONTINUE
C
C CALCULATE H, THE DISTANCE BETWEEN OUTPUT VALUES
C
      H=(R-1.)/FLOAT(NOUT)
C
C SET EFFIC EQUAL TO ZERO
C
      EFFIC=Ø
C
C SET THE INITIAL VALUES
C
      Y(1)=ETA2/SQRT(R)
      Y(2)=FPØ
      Y(3)=FP1
C
C WRITE HEADING FOR COLUMNS
```

```
C
      WRITE(6,152)
      WRITE(6,151)
C
C SET VARIABLES NEEDED FOR D02QAF. SET ALL BUT CIN(1) TO ZERO INITIALLY,
C AND RESET AS REQUIRED.
C
      CIN(1)=1.
C
      DO 500 K=2,5
       CIN(K)=0.
  500 CONTINUE
C
      DO 510 K=1,5
      COMM(K)=0.
      CONST(K)=0.
  510 CONTINUE
C
C START BY HAVING OUTPUT STEPS CERTAIN DIST. H APART.
C
      IW=3
      IW1=22
C
C FIRST USE ADAMS METHOD UNTIL THE EQUATIONS BECOME STIFF AS GEARS
C METHOD DOES NOT COPE WELL WITH GROWTH SOLUTION.
C
      DO 300 NC=1,5000
C
      IFAIL=0
      IF(ISTEP.EQ.1) THEN
         COMM(4)=1
      ELSE
         COMM(4)=-1
         COMM(5)=R-H
      ENDIF
C
C  RECALCULATE CD2 BEFORE EACH CALL TO THE NAG ROUTINE
C
      KAPPA=CALKAP(R,Y)
      CD2=KAPPA*MASSFC/(C*PI*AF**2*RSTAR)
C
      CALL D02QAF(R,.99,3,Y,CIN,TOL,FCN,COMM,CONST,COUT,W,IW,IW1,IFAIL)
      IF(ISTEP.EQ.0 OR.(NC/IWRITE*IWRITE).EQ.NC) THEN
         CALL OUTP(R,Y,COUT)
      ENDIF
      IF(IOUT.GT.10) CALL ENTEST(R,Y,COUT)
      IF(IEND(1).EQ.1) GO TO 699
C
      IF(IOUT.GT.10) CALL STEST(R,Y,COUT,ISTIFF)
      IF(ISTIFF(1).EQ.1) THEN
          WRITE(6,313) (I,ISTIFF(I),I=1 5)
          WRITE(6,311)
          WRITE(6,151)
          GO TO 320
      ENDIF
C TEST IF NEED TO OUTPUT EVERY STEP
C
```

```
      IF(Y(1).LE.FRAC(2).AND.ISTEP.EQ.Ø) THEN
         ISTEP=1
         WRITE(6,31Ø) IWRITE
         WRITE(6,151)
      ENDIF
C
  3ØØ CONTINUE
C
  32Ø CONTINUE
C
C
C NOW WRITE DO LOOP FOR CALLING DØ2QBF
C
C FIRST RESET SOME VALUES
C
      CIN(1)=1.
      CIN(4)=Ø.
      CIN(5)=Ø.
C
      DO 3Ø9 NC=1,5ØØØ
C
C  RECALCULATE CD2 BEFORE EACH CALL TO THE NAG ROUTINE
C
      KAPPA=CALKAP(R,Y)
      CD2=KAPPA*MASSFC/(C*PI*AF**2*RSTAR)
C
      IFAIL=Ø
C
         COMM(4)=1
C
      CALL DØ2QBF(R, .99,3,Y,CIN,TOL,FCN,COMM,CONST,COUT,NPED,PEDERV,PW,
     C W,IW,IW1,IFAIL)
C
      IF((NC/IWRITE*IWRITE).EQ.NC) THEN
         CALL OUTP(R,Y,COUT)
      ENDIF
      IF(IOUT.GT.1Ø) CALL ENTEST(R Y,COUT)
      IF(IEND(1).EQ.1) GO TO 699
C
  3Ø9 CONTINUE
C
      IEND(8)=1
      IEND(1)=1
C
C THIS REPRESENTS THE END OF THE RUN
C
  699 WRITE(6 7ØØ)
      DO 71Ø I=1,1Ø
      WRITE(6,7Ø1) I,IEND(I)
  71Ø CONTINUE
C
      CALL OUTP(R,Y,COUT)
C
      WRITE(6,1ØØ) IFAIL,TOL
C
      LX=EFFIC*LXMAX
      EDD=EDMAX*EFFIC
```

```
      WRITE(6,160) LX,EDD
      WRITE(6,110) R,(Y(J),J=1,3)
      STOP
C
   10 FORMAT(1X/1X,'GM=',1PE11.4,6X,'RSTAR=',1PE11.4,6X,'MASSFC=',
     + 1PE11.4)
   11 FORMAT(1X,3(1PE11.4,3X))
   20 FORMAT(1X/2X,'AINDEX',9X,'NM',13X,'FBB',12X,'AF'/
     + 1X,4(1PE11.4,4X))
   21 FORMAT(1X,4(1PE11.4,3X))
   25 FORMAT(1X/7X,'==CALCULATED PARAMETERS=='/1X/
     + 2X,'ASTAR',10X,'VFFSTR',9X,'MAX LX',9X,'LXMAX/LEDD',5X,'CD2',12X,
     + 'K2S',12X,'GASOV2',9X,'TSTRM'/
     + 1X,8(1PE11.4,4X))
   30 FORMAT(1X/7X,'==STARTING VALUES OF VARIABLES ARE=='/1X/
     + 2X,'R/RSTAR',8X,'V/VFF',10X,'FP0',12X,'FP1'/
     + 1X,F11.9,4X,4(1PE11.4,4X))
   31 FORMAT(1X,4(1PE11.4,4X))
   40 FORMAT(1X/7X,'==VARIABLES NEEDED FOR D02QBF=='/1X/
     + 2X,'TOL',11X,'NPED'/
     + 1X,1PE11.4,4X,I2)
   41 FORMAT(1X,1PE11.4,4X,I2)
   49 FORMAT(1X/7X,'==OTHER VARIABLES THAT CONTROL THE PROGRAM==')
   50 FORMAT(1X/2X,'NOUT=',I5,6X,'IFULL=',I4,6X,'ISTEP=',I4,
     + 6X,'IWRITE=',I4)
   60 FORMAT(1X/2(2X,5('FRAC(',I2,')=',1PE11.4,4X)/))
  100 FORMAT(1X/2X,'IFAIL',10X,'TOL'/1X,I2,13X,1PE11.4)
  110 FORMAT(1X/7X,'==FINAL VALUES==',1X/
     + 2X,'R',14X,'V/VFFSTR',7X,'FPO',12X,'FP1'/
     + 1X,4(1PE11.4,4X))
  152 FORMAT(1H1)
  151 FORMAT(1X/2X,'R',14X,'V/VFFSTR',6X,'FP0',11X,'FP1',11X,'V/VFF',
     + 9X,'EFFIC',9X,'TR (KEV)',10X,'GPTERM',9X,'DIFRAT')
  160 FORMAT(1X/2X,'LUMINOCITY=',1PE11.4,3X,'LOLEDD=',1PE11.4)
  310 FORMAT(1H1,'**** FROM HERE OUTPUT EVERY ',I3,' STEPS****')
  313 FORMAT(1X/2X,5('ISTIFF(',I2,')=',I2,5X,))
  311 FORMAT(1H1,'**** FROM HERE USE STIFF ROUTINE ****')
  700 FORMAT(1H1,'**** RUN ENDED, IEND VALUES ****'/
     + 1X/)
  701 FORMAT(1X,'END(',I2,')=',I2)
C
      END
C ======================================
C
      SUBROUTINE FCN(R,Y,F)
C
C ======================================
C
C THIS SUBROUTINE CONTAINS THE FUNCTIONS, NOTE THAT
C Y(1)=ETA, Y(2)=FP0, Y(3)=FP1.
C
      REAL K2S
      REAL F(3),Y(3)
C
      COMMON/BLOCK1/K2S,CD2,GASOV2,TSTRM
C
C CALC VARIABLE USED COMMONLY
```

```
C
      GASIM=GASOV2*Y(2)**.25/(Y(1)*Y(1))
C
      F(1)=-1.*(R**3/7.*Y(3)+1./(2.*Y(1)*R*R))/(1.-GASIM)
C
      F(2)=Y(3)
C
      F(3)=CD2/Y(1)/R**3*(K2S/R**1.5*Y(2)
     + -(4.*Y(2)+2.*R**3/CD2*Y(3))*3.*Y(1)/R
     + +1./(1.-GASIM)*
     + ((4.*Y(2)*Y(3)+Y(3)*Y(3)*R**3/CD2)*R**3/7.
     + +(-1.*(3.-4.*GASOV2*Y(2)**.25/Y(1)**2)*Y(1)+R/(2.*Y(1)*CD2))
     + *Y(3)
     + +2.*Y(2)/Y(1)/R**2+7./(2.*R**5)*GASIM))
C
      RETURN
      END
C ================================================
C
      SUBROUTINE OUTP(ROUT,Y,COUT)
C
C ================================================
C
      REAL Y(3),F(3),PT(9),K2S,COUT(16)
C
      COMMON/BLOCK1/K2S,CD2,GASOV2,TSTRM
      COMMON/BLOCK2/EFFIC,NOUT,IFULL,IOUT,H,IEND(10)
      COMMON/BLOCK3/FRAC(10)
C
C NOW NEED TO LOOK AT 'EFFICIENCY' UP TO THIS POINT
C CALCULATE      USING              TRAPEZIODAL METHOD
C
      IF(IOUT.NE.0) THEN
      EFFIC=EFFIC+
     + K2S/3.5*(ROUT**1.5*Y(2)+RPREV**1.5*Y2PREV)*(RPREV-ROUT)/2.
      ENDIF
C
      TR=Y(2)**.25*TSTRM
C
C DIFRAT=RATIO OF DIFFUSION TO FLOW OF RADIATION
C
      DIFRAT=-Y(3)/(4.*Y(2)*CD2)
      GPTERM=GASOV2*Y(2)**.25/Y(1)**2
C
C WRITE THE VARIABLES PLUS V/VFF, EFFIC, AND TR(KEV)
C
      WRITE(6,120) ROUT,(Y(J),J=1,3),Y(1)*SQRT(ROUT),EFFIC,
     + TR,GPTERM,DIFRAT
C
C ALSO WRITE THE VARIABLES IN BFGVAL
C
      WRITE(1,121) ROUT,(Y(J),J=1,3),Y(1)*SQRT(ROUT),TR
C
      IF(IOUT/IFULL*IFULL.EQ.IOUT.OR.IEND(1).EQ.1) THEN
C
C WRITE SOME OF THE TERMS TO SEE WHICH DOMINATE
C
```

```
C
C
      GPTERM=GASOV2*Y(2)**.25/Y(1)**2
      GRAVV=Ø.5/Y(1)/ROUT**2
      PRV=ROUT**3*Y(3)/7.
C
      CALL FCN(ROUT,Y,F)
C
      WRITE(6,125) (F(J),J=1,3)
C
      COEF3=CD2/Y(1)/ROUT**3
C
      PT(1)=K2S*Y(2)*COEF3/ROUT**1.5
      PT(2)=-12*Y(2)*Y(1)/ROUT*COEF3
      PT(3)=-6.*ROUT**2*Y(3)*Y(1)/CD2*COEF3
      PT(4)=4./7.*Y(2)*Y(3)*ROUT**3*COEF3/(1.-GPTERM)
      PT(5)=ROUT**6/7.*Y(3)*Y(3)/CD2*COEF3/(1.-GPTERM)
      PT(6)=-3.*Y(1)*Y(3)*COEF3/(1.-GPTERM)
      PT(7)=ROUT/2./Y(1)/CD2*Y(3)*COEF3/(1.-GPTERM)
      PT(8)=2.*Y(2)/Y(1)/ROUT**2*COEF3/(1.-GPTERM)
      PT(9)=3.5*GASOV2*Y(2)**.25/ROUT**5/Y(1)**2*COEF3/(1.-GPTERM)
C
      WRITE(6,13Ø)  GPTERM,GRAVV,PRV
C
      WRITE(6,14Ø) (PT(K),K=1,9)
C
      WRITE(6,145) (J,COUT(J),J=1,16)
C
      WRITE(6,15Ø)
      ENDIF
C
C IF FRACTIONAL CHANGE IN FPO OR ETA BETWEEN OUTPUTS IS GREATER
C THAN FRAC REDUCE H.
C
      IF(IOUT.EQ.Ø) THEN
         Y1DIF=Ø.
      ELSE
         Y1DIF=ABS((Y1PREV-Y(1))/Y(1))
      ENDIF
C
      IF(ABS(Y(3)*H/Y(2)).GT.FRAC(1).OR.Y1DIF.GT.FRAC(1).AND.H.GT.
     + .ØØØØØ1)
     + H=H/2.
C
      IOUT=IOUT+1
C
C STORE PREVIOUS VALUES OF Y'S FOR VARIOUS PURPOSES
C
      Y1PREV=Y(1)
      Y2PREV=Y(2)
      Y3PREV=Y(3)
      RPREV=ROUT
C
      RETURN
C
  15Ø FORMAT(1X/2X,'R',14X,'V/VFFSTR',6X,'FPØ',11X,'FP1',11X,'V/VFF',
     + 9X,'EFFIC',9X,'TR (KEV)',1ØX,'GPTERM',9X,'DIFRAT')
```

```
  120 FORMAT(1X,F12.9,3X,5(1PE11.4,3X),1PE15.8,2(3X,1PE11.4))
  121 FORMAT(1X,F12.9,3X,4(1PE11.4,3X),1PE15.8)
  125 FORMAT(1X/2X,'F(1)',11X,'F(2)',11X,'F(3)'/1X,3(1PE11 4,4X))
  130 FORMAT(1X/2X,'GPTERM',9X,'GRAVV',10X,'PRV'/
     + 1X,3(1PE11.4,4X))
  140 FORMAT(1X/2X,'PT1',10X,'PT2',10X,'PT3',10X,'PT4',10X,'PT5',
     + 10X,'PT6' 10X,'PT7',10X,'PT8',10X,'PT9'/1X,9(1PE10.3,3X))
  145 FORMAT(4(1X/2X,5('COUT(',I2,')=',1PE11.4,5X)/))
C
      END
C ======================================
C
      SUBROUTINE ENTEST(R,Y,COUT)
C
C ======================================
C
C SUBROUTINE TO TEST WHETHER THE RUN SHOULD END
C
      DIMENSION Y(3),COUT(16)
C
      COMMON/BLOCK1/K2S,CD2,GASOV2,TSTRM
      COMMON/BLOCK2/EFFIC,NOUT,IFULL,IOUT,H,IEND(10)
      COMMON/BLOCK3/FRAC(10)
C
      REAL K2S
C
      IF(Y(1).LT.0.) IEND(2)=1
      IF(Y(2).LT.0.) IEND(3)=1
      IF(Y(3).GT.0.) IEND(4)=1
      IF((1.-GASOV2*Y(2)**.25/Y(1)**2).LT.FRAC(3)) IEND(5)=1
      IF(Y(1).LT.FRAC(4)) IEND(6)=1
      IF(ABS(COUT(1)).LT.FRAC(5)) IEND(7)=1
C
      DO 8 I=2,10
      IF(IEND(I).EQ.1) IEND(1)=1
    8 CONTINUE
C
      RETURN
      END
C ============================
C
      FUNCTION CALKAP(R,Y)
C
C ============================
C
C FUNCTION TO ALLOW KAPPA TO BE VARIED
C
      DIMENSION Y(3)
C
      CALKAP=0.20
C
      RETURN
      END
C ==========================================================
C
       SUBROUTINE PEDERV(R,Y,PW)
C
```

```
C ================================================================
C
      REAL R,Y(3),PW(3,3)
C
      COMMON/BLOCK1/K2S,CD2,GASOV2,TSTRM
      REAL K2S
C
      GASIM=GASOV2*Y(2)**.25/Y(1)**2
C
      PW(1,1)=(1./2./Y(1)**2/R**2+GASIM*
     C (1./2./Y(1)**2/R**2+R**3*Y(3)/Y(1)/3.5))
     C /(1.-GASIM)**2
C
      PW(1,2)=-.25*GASIM/Y(2)*(R**3*Y(3)/7.+.5/Y(1)/R**2)
     C /(1-GASIM)**2
C
      PW(1,3)=-R**3/7./(1.-GASIM)
C
      PW(2,1)=0.
C
      PW(2,2)=0.
C
      PW(2,3)=1.
C
      PW(3,1)=CD2/R**3*(-K2S*Y(2)/R**1.5/Y(1)**2
     C +(-1.*R**3/7./Y(1)**2*(1.+GASIM)
     C *(4.*Y(2)*Y(3)+R**3/CD2*Y(3)*Y(3))
     C -1.*(R/CD2+2.*GASOV2*Y(2)**.25)*Y(3)/Y(1)**3
     C -4.*Y(2)/Y(1)**3/R**2
     C -GASIM/R**5/Y(1)**2*(11.5-7.*GASIM))
     C /(1.-GASIM)**2)
C
      PW(3,2)=CD2/R**3*(K2S/Y(1)/R**1.5-12./R
     C +((4.+3.*GASIM)*Y(3)/Y(1)*R**3/7.
     C +R**6/28.*GASIM/Y(2)/CD2
     C +(.25+R/Y(1)**2/CD2/8)*GASIM*Y(3)/Y(2)
     C +(1.-.75*GASIM)*2./R**2/Y(1)**2
     C +7/8*GASOV2/R**5/Y(2)**.75/Y(1)**3)
     C /(1.-GASIM)**2)
C
      PW(3,3)=CD2/R**3*(-6.*R**2/CD2
     + +((4.*Y(2)+2.*R**3*Y(3)/CD2)*R**3/7./Y(1)
     + -(3.-4.*GASIM)
     + +R/2./Y(1)**2/CD2)/(1.-GASIM))
C
      RETURN
      END
C ================================================================
C
      SUBROUTINE STEST(R,Y,COUT,ISTIFF)
C
C ================================================================
C
C SUBROUTINE TO TEST WHETHER OR NOT TO USE GEARS METHOD
C
      DIMENSION Y(3),COUT(16),ISTIFF(5)
      COMMON/BLOCK3/FRAC(10)
```

```
C
      IF(ABS(COUT(1)).LE.FRAC(6)) ISTIFF(2)=1
      IF(Y(1).LE.FRAC(7)) ISTIFF(3)=1
      IF(Y(2).GE.FRAC(8))  ISTIFF(4)=1
C
      DO 1 I=2,5
      IF(ISTIFF(I).EQ.1) ISTIFF(1)=1
    1 CONTINUE
C
      RETURN
      END
```

References.

Adams, 1978
Cosmic X-ray Sources Adam Hilger.

Akasofu, S. I. 1978
Space Sci. Rev. **21** 489.

Apparao, K. M. V. 1985
Ap. J. **292** 257.

Arnett, W. D. + Bowers, R. L. 1977
Ap. J. Supp. Ser. **33** 415.

Arons, J. + Lea, S. M. 1976
Ap. J. **207** 914.

Basko, M. M. + Sunyaev, R. A. 1975
Astron. Ap. **42** 311.

Basko, M. M. + Sunyaev, R. A. 1976
M.N.R.A.S. **175** 395.

Beard, D. B. 1960
J. G. R. **65** 3559.

Boas, M. 1966
Mathematical Methods in the Physical Sciences John Wiley + Sons.

Borner, G, 1980
Physics Reports **60** 151.

Boyd, T. M. + Sanderson, J. J. 1969
Plasma Dynamics Thomas Nelson + Sons Ltd.

Canuto, V. et al. 1971
Phys. Rev. D. **3** 2303.

Daugherty, J. K. + Ventura, J. 1978
Phys. Rev. D. **18** 1053.

Davidson, K. 1973
Nature **246** 1.

Davidson, K. + McCray, R. 1980
Ap. J. **241** 1042.

Davidson, K. + Ostriker, J. P. 1973
Ap. J. **179** 585.

Eardley, D. M. + Press, W.H. 1975
Ann. Rev. Astron. Ap. **13** 381.

Evans, A. J. 1981
PhD Thesis University of London.

Fabian, A. et al 1977
M.N.R.A.S. **179** 9P.

Felten, J.E. + Rees, M.J. 1972
Astron. Ap. **17** 226.

Frank, J. et al 1986
Accretion Power In Astrophysics Cambridge University press.

Gear, C. W. 1971
Communications of the A.C.M. **14** 176.

Giacconi, R. et al 1962
Phys. Rev. Lett. **9** 439.

Giacconi, R. et al 1971
Ap. J. Lett. **167** L67.

Grindley, J.E. et al 1984
Ap. J. **277** 286.

Holt, S. S. + McCray, R. 1982
Ann. Rev. Astron. Ap. **20** 323.

Katz, J. I. 1986
High Energy Astrophysics Addison-Wesley Publishing Co.

Kirk, J. G. + Galloway, D. J. 1981
M.N.R.A.S. **195** 45P.

Klein, R. I. et al. 1980
Ap. J. **237** 912.

Joss, P. C. + Rappaport, S. A. 1984
Ann. Rev. Astron. Ap. **22** 537.

Lambert, J. D. 1976
Computational Methods for Ordinary Differential Equations John Wiley + Sons.

Langer, S. H. + Rappaport, S. 1982
Ap. J. **257** 733.

Lieu, R. 1983
M. N. R. A. S. **205** 973.

Liang, E. P. + Nolan, P. L. 1984
Sp. Sci. Rev. **38** 353.

Lindblom, L. L. 1986
Ap. J. **303** 146.

Lynden-Bell, D. 1969
Nature **233** 690.

Manchanda, R. K. 1977
Ap. Sp. Sci. **50** 179.

Margon, B. 1984
Ann. Rev. Astron. Ap. **22** 507.

Mason, K. O. 1985
Space Science Rev. **40** 99.

Michel, F. C. 1977
Ap. J. **214** 261.

Mihalas, D. 1978
Stellar Atmospheres W. H. Freeman + company.

Mihalas, D. + Klein, R. I. 1982
J. Comp. Phys. **46** 97.

NAG 1983
Numerical Algorithms Group Reference Mannual Mk10.

Pacholczyk, A. G. + Stoeger, S. J. 1986
Ap. J. **303** 76.

Parmar, A. N. et al. 1986
Ap. J. **304** 664.

Pomraning, G. C. 1973
The Equations of Radiation Hydrodynamics Pergamon Press.

Potter, D. 1973
Computational Physics John Wiley + Sons.

Pravdo, S. H. et al. 1979
Ap. J. **231** 912.

Pringle, J.E. 1981
Ann. Rev. Astron. Ap. **19** 137.

Rosner, R. et al 1985
Ann. Rev. Astron. Ap. **23** 413.

Schreier, E. J. 1982
(Paper in) Galactic X-ray sources Nato advanced study Inst.
John Wiley + Sons.

Spitzer, L. 1956
Physics of fully ionised gases Interscience, New York.

Tapia, S. 1977
Ap. J. **212** L125.

Taylor, J. H. +Weisberg, J. M. 1982
Ap. J. **253** 908.

Trumper, J. et al 1978
Ap. J. **219** L105.

Trumper, J. et al. 1986
Ap. J. **300** L63.

Wandel, A. et al 1984
Ap. J. **282** 53.

Wang, Y. M. + Frank, J. 1981
Astron. Ap. **93** 255.

Wasserman, I. + Shapiro, S. L. 1983
Ap. J. **265** 1036.

Weyman, R. 1965
Phys. Fluids **8** 2112.

Willmore, A.P. 1978
Rep. Prog. Phys. **41** 511.

Wilson, J.G. 1976
Cosmic Rays Wykenham Publications Ltd.

Zel'dovich, Ya B. + Shakura, N. I. 1969
Soviet Astron. **13** 175.

§4.4. Corrections.

Davidson 1973 considers accretion flow near the bottom of the accretion funnel where the flow is slowed down by the radiation pressure gradient. The two dimensional radiation transfer problem near the bottom of the accretion funnel is considered. Gas pressure and gravity are ignored, as these are small compared to the radiation pressure and the ram pressure. In the case where gas pressure and gravity are ignored the momentum equation is:–

$$S\frac{\delta v}{\delta z}+\frac{1}{3}\frac{\delta U}{\delta z}=0$$

where $S=\rho v$ (the mass flux) and U is the radiation density. Therefore :–

$$U=3S|v_{ff}-v|$$

The velocity is then expressed in terms of $Q=v/v_{ff}$ and this is substituted into the expression for the radiation flux. The diffusion approximation for the radiation flux is taken. The radiation flux is taken as:–

$$\mathbf{F}=-\frac{c}{3}\frac{m_p}{\sigma_T\rho}\nabla U+\mathbf{v}U$$

It is then assumed that production of radiation is prompt, i.e. kinetic energy lost is immediately converted into radiation, therefore:–

$$\nabla.\mathbf{F}=S\frac{\delta}{\delta z}\left(\frac{v^2}{2}\right)$$

On substituting the expression for F and U into this expression, writing in terms of Q the following expression is obtained:–

$$\nabla^2 Q=\frac{\sigma_T S}{m_p c}\frac{\delta}{\delta z}\left(6Q^{1/2}-5Q\right)$$

∇^2 is then expressed in cylindrical coordinates, and given suitable boundary conditions the above equation for Q may then be solved numerically.

The author takes the boundary conditions to be $Q=1$ at $z=\infty$ and $Q=0$ at $z=0$. The other required boundary condition is the radiation density at $R=R_c$, the side of the funnel. As the funnel is assumed to be optically thick, the radiation density is very much larger at the centre of the funnel than at the sides; therefore the radiation density is taken to be zero at $R=R_c$. Given these boundary conditions the author numerically solves the above differential equation for Q, and plots contours of constant Q (i.e. constant velocity) across the accretion funnel.

The model in chapter 5 of this thesis uses similar equations to those in this paper by Davidson. The main purpose of Davidson's paper was to calculate the shape of the region near the bottom of the funnel where the velocity is much less than the free fall velocity, when the luminosity is $\sim 10^{37} erg\, sec^{-1}$.

The model in chapter 5 considers a much wider range of phenomena and luminosities, including highly super-Eddington accretion. The model in chapter 5 also does not drop terms such as gas pressure and gravity. Also plots of radiation temperature and velocity as a function of radius are presented, for a wide range of accretion rates and funnel radii. The emitted spectrum is also calculated and plotted.

§4.5.3. Corrections.

In the case we are considering, the matter is free falling towards the base of the accretion funnel. Therefore the more realistic minimum pressure required to slow down the accretion flow is equal to the ram pressure of the matter flowing towards the stellar surface, i.e. at the bottom of the funnel:–

$$P_{r\,min} = \rho v_{ff}^2 = \frac{\dot{m}}{A} v_{ff} = \frac{L_x}{v_{ff\star} \pi a_f^2 r_\star^2}$$

It is also worth noting here that L_x refers to the total luminosity, coming from 2 accretion funnels, i.e. $L_x = 2GM\dot{m}/r_\star$. When $P_{\star min}$ as calculated in §4.5.3 is replaced by $P_{r\,min}$ as calculated above table 4.1 becomes:–

a_f	$P_{r\,min}$	$T_r = \left(\frac{3P_r}{a_f}\right)^{1/4} keV$	$E_{peak} = 1.5936 T_r\, keV$
0.1	3.19×10^{16}	5.15	8.21
0.05	1.27×10^{17}	7.29	11.62
0.02	7.97×10^{17}	11.53	18.37
0.01	3.19×10^{18}	16.30	25.99

As before, the table refers to a luminosity of $3 \times 10^{37} erg\, sec^{-1}$. It is clear that the peak energy output is comparable to that of the observed sources when $a_f = 0.05$.